Classification of Sub-10 nm Aerosol: Theory, Instrument Development, and Experiment

Thesis by
Andrew Joseph Downard

In Partial Fulfillment of the Requirements
for the Degree of
Doctor of Philosophy

California Institute of Technology
Pasadena, California

2012

(Defended 8 May 2012)

To my mother, father, and brother.

Acknowledgements

My thesis advisor, **Rick Flagan**, is a scientist of exceptional creativity and integrity. In working with him, I had a tremendous amount of freedom and I was afforded the opportunity of working with the CLOUD team at CERN. I came into Caltech afraid of sharp hand tools and uncertain of myself with physics and math; with the support of Rick, I leave as a competent machinist and a self-confident scientist.

I thank my committee, John Seinfeld, Jack Beauchamp, and Paul Wennberg, for all of their support.

My personal growth at Caltech has been remarkable. I thank in particular my non-academic mentors, Lee Coleman, Ken Pickar, Karen Cohen, Sue Chiarchiaro, and Felicia Hunt. I am deeply grateful for their support.

I thank Mike Roy and John Van Deusen for helping me transform myself into a precision machinist.

The CLOUD team at CERN, led by **Jasper Kirkby**, is a group of top flight physicists from all over Europe. I appreciated the day-to-day mentoring and support from Jasper, and I enjoyed spending time working in Helsinki with **Markku Kulmala**, Tuukka Petäjä, Katrianne Lehtipalo, Jyri Mikkilä, Mikko Sipilä, Heikki Junninen, Joonas Vanhanan, Tuomo Nieminen, Simon Schallhart, Maija Kajos, Jonathan Duplissy, Stéphanie Gagné, Sigi Schobesberger, and the rest of Markku's army. In Frankfurt, **Joachim Curtius** went out of his way to make sure that I was well supported in my time in Europe, and I enjoyed working alongside Andreas Kürten, Daniela Wimmer, Fabian Kreissl, Sebastian Ehrhart, and Katja Ivanova.

I continue my practice of typesetting those who have funded me during my thesis work in bold with my thanks to **Urs Baltensperger** of the Paul Scherrer Institut jn Baden, Switzerland. His team was a pleasure to work with, especially Francesco Riccobono, Federico Bianchi, Josef Dommen, Marie Laborde, and Arnaud Praplan.

Our time at CERN was intense, and we were all very supportive of each other along the way. I really enjoyed working alongside Eimear Dunne, Agnieszka Kupc, Axel Metzger, Georgios Tsgkogeorgas, Antonio Amorim, João Almeida, Martin Bre-

itenlechner, Werner Jud, Antonio Tomé, and Daniel Hauser. There are also several other scientists. engineers, and professors who are members of the CLOUD team that I enjoyed working with, including Armin Hansel, André David, Serge Mathot, Antti Onnela, Frank Stratmann, Aron Vrtala, Paul Wagner, Heike Wex, Ken Carslaw, and the incredibly energetic and constructive Doug Worsnop.

Ale Franchin and Linda Rondo grew to be particularly close friends of mine from the CLOUD project. Ale visited the Flagan Lab this past winter and Linda is coming in the summer. It is wonderful to have friends as collaborators.

On that note, I enjoyed working with Arón Varga of the Sossina Haile Lab at Caltech. He and I had a delightful collaboration and share a strong friendship.

It was a joy to work with such talented colleagues at Caltech. I thank in particular Xerxes Lopez-Yglesias and Andrew Metcalf. I also really enjoyed working alongside Ruoyu Zhang, Jason Gamba, Arthur Chan, Havala Pye, Joey Ensberg, Christine Loza, Andi Zund, Tristan Day, Jason Surratt, Manuj Swaroop, Josh Black, Ubaldo Cordova-Figueroa, Roseanna Zia, Lindsay Yee, Jill Craven, and the numerous others who I have shared offices and fun conversations with over the years.

The first years of my graduate work were with **John Brady** and **Zhen-Gang Wang**. I learned a lot from observing the standard of excellence that they strive for in all of their endeavors. They are both excellent teachers, and I admire their ability to capture the essential physics of complex systems with the aid of intuitive models and simulation. There is good reason why their students have gone on to be the leading academics in their respective fields.

My closest friends, Glenn Garrett, Mike Shearn, and Anna Beck, have been exceedingly supportive during my time at Caltech. I also thank Vanessa Jönsson, Matt Eichenfield, Jim Swan, Valerie Kristof, Scott Kelber, Kathleen Spencer, Tony Roy, my fellow resident associates, and the Caltech Administration (especially my friends in the Division of Chemistry and Chemical Engineering, the Housing Office, the Dean's Office, and the Counseling Center), all of whom made the journey enjoyable.

I appreciate all of the support of the Caltech family, and I wish I could include the names of all the people who have been important to me, like Anne Hormann and

Stephanie Berrocal. This would take a second thesis, and the department is paying by the page. Please accept my sincerest thanks!

Abstract

The large diffusion coefficients of sub-10 nm aerosol have posed a long-standing challenge to the aerosol community; to understand nucleation and early growth, there is a need for methods such as those presented here that transmit a strong, high resolution signal of classified charged aerosol to the detector. I introduce a framework for comparison of the Flagan Laboratory classifiers to other instruments, and I show why our instruments perform favorably relative to these alternatives. Reducing the size of the classification region reduces the effect of diffusion on performance and will ultimately enable the development of personal health monitors. The deployment of our instruments to the Cosmics Leaving OUtdoor Droplets experiment at CERN motivated a deeper look into detector performance and design for extreme operating conditions. I caution about the possible interference of ion nucleation with measurements and introduce a process for optimizing detector performance at arbitrary temperature. My experience with aerosol classifications has inspired the invention of separation methods for related fields; I conclude by describing methods for the high resolution separation of gas ions and of aqueous particles such as proteins and antibodies.

Contents

List of Figures

List of Tables

Chapter 1

An Asymptotic Analysis of Differential Electrical Mobility Classifiers

1.1 Abstract

An asymptotic analysis of balanced-flow operations of differential mobility analyzers (DMAs) and a new class of instruments that includes opposed migration aerosol classifiers (OMACs) and inclined grid mobility analyzers (IGMAs) provides new insights into the similarities and differences between the devices. The characteristic scalings of different instruments found from minimal models are shown to relate the resolving powers, dynamic ranges, and efficiencies of most such devices. The resolving powers of all of the instruments in the nondiffusive regime of high voltage classifications, $\mathcal{R}_{nd}$, is determined by the ratio of the flow rate of the separation gas (sheath or crossflow) to that of the aerosol. At low voltage, when diffusion degrades the classification, the OMAC and the IGMA share an $\mathcal{R}_{nd}$ factor advantage in dynamic range of mobilities over the DMA, although the OMAC also suffers greater losses because diffusion immediately deposits particles onto its porous electrodes. Based upon this analysis, a single master operating diagram is proposed for DMAs, OMACs, and IGMAs. Analysis of this operating diagram and its consequences for the design of differential electrical mobility classifiers suggests that OMACs and IGMAs also have advantages over DMAs in design flexibility and miniaturization. Most importantly, OMACs and IGMAs may outperform DMAs for the currently difficult classification of particles with diameters less than 10 nm. On the other hand, DMAs are more amenable to voltage scanning-mode operation to enable accelerated size distribution measurements, whereas it is most convenient to operate OMACs and IGMAs in volt-

age stepping-mode operation.

1.2 Nomenclature

b	distance between electrodes
c	geometry constant for electrostatic breakdown
C	particle concentration
$\hat{C}$	dimensionless particle concentration
C_0	initial particle concentration
D	diffusion coefficient
D^*	diffusion coefficient of target particle
D_p	electrical mobility equivalent diameter
e	elementary charge
$\mathcal{E}[u]$	$= u \cdot \mathrm{erf}[u] + \exp[-u^2]/\sqrt{\pi}$
E_B	electrostatic breakdown field strength
$\mathrm{erf}[u]$	error function
f	electric field geometry factor
G	geometry and flow factor
Gz	Graetz number
$H[u]$	Heaviside step function
k	Boltzmann constant
L	length of classification region
P	absolute pressure
$\hat{P}$	dimensionless pressure
P_0	reference pressure
ΔP_c	characteristic pressure drop
Pe	migration Péclet number
Q_a	aerosol flow rate
Q_c	crossflow flow rate
Q_e	excess (exhaust) flow rate
Q_s	sample (classified) flow rate
Q_{sh}	sheath flow rate
$\mathcal{R}$	resolving power
$\mathcal{R}_{nd}$	nondiffusive resolving power
Re	Reynolds number
Sc	Schmidt number
T	temperature
u	aerosol velocity profile
$\hat{u}$	dimensionless aerosol velocity profile
V	applied voltage
V_B	electrostatic breakdown voltage
W	width of classification region
Z	electrical mobility
Z^*	target electrical mobility
ΔZ_{FWHM}	full width at half maximum of the transfer function

1.3 Greek Letters

α	flow distortion parameter
β	ratio of aerosol to separation gas flow rates
ϵ	span of aerosol (sample) streamlines at inlet (outlet)
ζ	$= \mathcal{R}_{nd}\,(Z/Z^* - 1)$
η	transmission efficiency
θ	angle between fluid and target particle streamlines
κ	dimensionless flow parameter
ν	kinematic viscosity
ρ	density
σ	dimensionless diffusion parameter
σ_c	critical dimensionless diffusion parameter
τ_d	characteristic diffusion time across target particle streamlines
τ_r	residence time in the classification region
Ω	transfer function

1.4 Introduction

Field deployable instruments for the classification of airborne particulate matter are critical for determining the effect of aerosols on the climate and human health. High-resolving power aerosol particle classification by electrical mobility was made possible by the cylindrical differential mobility analyzer (DMA) [1]. In a continuous scanning mode, such devices can classify aerosols across their entire dynamic ranges in under a minute [2], or even in a few seconds using fast-response detectors [3, 4]. A variety of custom-made and commercially available instruments enable investigators to remotely monitor the evolution of aerosol populations ranging from 1 nm – 10 μm.

While these classical DMAs provide valuable information, challenges remain for accurate classification at the low and high ends of the size spectrum [5]. Classification of particles approaching 1 μm becomes difficult because these larger particles may be multiply charged. To the extent that the relevant charging statistics are known, this has been a manageable problem resolved by using a variety of data inversion algorithms. Classification of particles smaller than 10 nm in diameter is difficult because these smaller particles diffuse rapidly, degrading the resolving power of most DMAs. This problem can be addressed by reducing the DMA's residence time, but doing so has required innovative designs that achieve small-diameter particle classification at the expense of affordability and dynamic range of mobilities.

The resolving power of a DMA is a measure of the ability of a method to resolve particles of similar electrical mobility. We follow the definition of Flagan (1999) proposed by analogy to terminology used in a wide range of spectroscopies: the resolving power $\mathcal{R}$ is the ratio of the mobility, Z^*, of the particle that is transmitted with the greatest efficiency to the full range of mobilities that is transmitted with at least half of that efficiency, ΔZ_{FWHM}, i.e., $\mathcal{R} = Z^*/\Delta Z_{FWHM}$. For large particles that require high voltages for classification, the resolving power of a DMA is determined by the ratio of the sum of the flow rates of the sheath and exhaust flows, Q_{sh} and Q_e,

respectively, to the sum of the aerosol and sample flows, Q_a and Q_s, i.e.,

$$\mathcal{R}_{nd} = \frac{Q_{sh} + Q_e}{Q_a + Q_s} = \beta^{-1}, \tag{1.1}$$

where β is the DMA flow ratio. The resolving power in this limit is unaffected by Brownian diffusion and is, therefore, labeled the nondiffusive resolving power.

For small particles that are classified at low voltages, Brownian diffusion degrades the instrument resolving power. Flagan (1999) showed that the resolving power of a DMA in the diffusion-dominated limit varies with the applied voltage according to

$$\mathcal{R} \propto V^{1/2}. \tag{1.2}$$

Thus, for any desired instrument resolving power, Brownian diffusion places a lower bound on the range of particle mobilities that can be classified with a resolving power that is close to the setpoint defined by the ratio of the flow rates. Measurements can be made at lower voltages, but the resolving power will decrease as $V^{1/2}$.

There exists another limit to the range of mobilities that can be probed with a DMA. When the magnitude of the electric field exceeds a critical value, E_B, electrostatic breakdown may occur. The resulting arc may generate particles within the DMA and damage components of the instrument by eroding precisely machined metal surfaces or charring polymeric materials. Typically, $E_B \sim 10^6$ V/m. Thus, the dynamic range of a DMA is constrained from above by electrostatic breakdown (or by the maximum voltage that the power supply can deliver) and from below by Brownian diffusion. A useful dynamic range is achieved in most DMAs by employing an electrode spacing of ~ 0.01 m, enabling operation at voltages as high as 10 kV, although the dynamic range of some instruments has been extended by increasing the electrode spacing.

Early DMAs were designed to classify particles approaching 1 μm in diameter. As a result, they employed classification columns of much longer length L than the spacing between the electrodes, e.g., $L/b \approx 48$ in the classical DMA of Knutson and Whitby (1975). Interest in ultrafine particles led to the development of instruments

with smaller aspect ratios, e.g., $L/b \approx 14$ for the Vienna DMA [6], which was the first modern DMA to size particles in the sub-5 nm size range. The radial DMA [7] and the nano-DMA ([8]; TSI Model 3085), instruments designed to probe nanoparticles, both employed even smaller aspect ratios of about 5. In all of these instruments, the particle trajectories through the classification region deviate from the direction of the channel walls by shallow angles. Significantly, it has been shown that the best resolving power in the low-nanometer regime would be achieved with classifiers in which the aspect ratio approaches unity [9]. A number of instruments applied that approach to the measurements of particles with an electrical mobility equivalent diameter as small as 1 nm [10, 11, 12, 13]. Through meticulous aerodynamic design and fabrication, short aspect ratio DMAs have been developed that extend laminar flow operation to Reynolds numbers well beyond the usual turbulent transition [10, 11, 12]. This has enabled the attainment of unprecedented resolving power for small nanoparticles and gas ions. However, the range of mobilities that can be probed in a given instrument at fixed flow rates while maintaining that high resolving power becomes extremely small due to the convergence of the diffusive regime with the electrostatic breakdown limit.

A number of investigators have explored ways to extend the dynamic range of high resolution electrical mobility measurements. For example, the resolving power has been shown to be enhanced when the direction of migration is reversed in the cylindrical DMA, i.e., by classifying particles as they migrate from the inner electrode toward the outer one [14]. This was a consequence of the nonuniformity of the field between the electrodes.

More dramatic improvements were predicted for a DMA that includes a component of the electric field parallel to the direction of the sheath flow [15]. A practical way to produce a classifier in which the electric field is, as suggested by Loscertales, inclined relative to the usual transverse field of the DMA is to place inclined screens or grids within a DMA-like flow channel in an inclined grid mobility analyzer (IGMA; [16, 17]). This has recently been applied in an instrument called the symmetric inclined grid mobility analyzer (SIGMA), which enables simultaneous measurement of

gas ions or small nanoparticles of both polarities. Employing high volumetric flow rates, the SIGMA can measure ions/particles in the 0.4 to 7.5 nm size range [18].

Flagan (2004) modeled another form of inclined field mobility analyzer called the opposed migration aerosol classifier (OMAC) in which porous electrodes define the classification channel. Particles enter one end of the channel. An electric field applied between the porous electrodes induces migration that is countered by a flow across the classification channel. Particles of the target mobility pass through the channel parallel to the electrodes due to the balance of electrostatic and drag forces. While the planar OMAC modeled by Flagan (2004) can be viewed as a form of the inclined grid device proposed by Tammet (1999), other OMAC designs are not so easily translated into practical inclined grid forms. Examples include an OMAC that employs porous electrodes in the form of coaxial cylinders with a radial crossflow and one consisting of parallel porous disk electrodes with an axial crossflow. By eliminating the larger channel in which the inclined grid electrodes are immersed, the OMAC leads to conceptually simple classifier designs.

Using Monte Carlo simulations to probe the relative roles of migration and diffusion, the onset of diffusional degradation of the classifier resolving power was found to be delayed to much lower voltages than in the DMA [19]. By enabling operation at $\mathcal{R} \sim \mathcal{R}_{nd}$ at low voltages, the OMAC expands the range of mobilities between the diffusive and electrostatic breakdown limits beyond that which is possible with a DMA. An OMAC with an electrode spacing comparable to present DMAs could, therefore, be used for high resolution measurements over a much wider dynamic range of mobilities than a DMA. Alternatively, a dynamic range comparable to present DMAs could be achieved with a smaller electrode spacing. This enables the instrument to be made much smaller than present DMAs.

While theoretical analyses and simulations demonstrate marked differences in the resolving power of these two distinct types of differential electrical mobility classifiers (DEMCs), the favorable performance of OMACs and IGMAs relative to DMAs has not been adequately explained. The present paper seeks to build upon the work of Flagan (1999, 2004) to elucidate the differences between DMAs and the promising

new OMACs and IGMAs. We begin with the development of minimal models that reveal the underlying differences, extending the diffusive transfer function ([20, 21] – see also [22, 23, 24]) to the OMAC. With these simple models, we identify scaling principles that make it possible to collapse the resolving powers of DMAs, OMACs, and IGMAs onto a single plot as a function of an appropriately scaled dimensionless operating parameter. Significantly, a general operating diagram for ideal DEMCs is then constructed and its predictions are compared to the performance of real instruments. As is the case with all asymptotic analyses, the results are not precise for all conceivable DMAs, OMACs, and IGMAs. A number of significant features of real devices are neglected in the interest of clarity, notable amongst which are nonuniform fields, small aspect ratios, and end effects.

1.5 Generalizing DMA performance with insights from a minimal model

We begin by considering the simplest DMA concept – a planar DMA of length L and width W where an electric field is applied across a gap of thickness b. We further restrict the model to large aspect ratio devices, $L/b \gg 1$, so that migration owing to the electric field is primarily in the direction normal to fluid streamlines. All particles are assumed to carry only one elementary charge. The flows are taken to be balanced, so the volumetric flow rates $Q_a = Q_s$ and $Q_{sh} = Q_e$. For simplicity, the velocity profiles are taken to be uniform (plug flow). As illustrated in Fig. 1.1, if edge effects are neglected, then the kinematic resolving power $\mathcal{R}_{nd} = \beta^{-1} = Q_{sh}/Q_a$ is also equal to the fraction of the inlet occupied by sheath streamlines relative to that occupied by the aerosol streamlines, $\mathcal{R}_{nd} = (b - \epsilon)/\epsilon$, where ϵ/b is the fraction of the inlet occupied by aerosol flow fluid streamlines, as shown in Fig. 1.1. Following the analysis of Stolzenburg (1988), a coordinate axis aligned with the target *particle* streamlines is defined as shown in Fig. 1.2. Since the coordinate axis is aligned with the target particle streamlines, particles are advected in the $x-$direction by

the flow and, to a small extent, the field. Diffusion in the $x-$direction is negligible in the large aspect ratio limit. Diffusion is important, however, across the target particle streamlines in the $y-$direction, where particles of mobilities greater or less than Z^* will also be displaced by the electric field. Using this approach, the steady-state transport of dilute aerosols through a planar DMA with a large aspect ratio $L/b \gg 1$ operated at a large kinematic resolving power $\mathcal{R}_{nd} \gg 1$ is modeled using the convection-diffusion equation for particles, including both advection by the gas flow and the contribution of electrical migration along the target particle streamline ($x-$direction) and perpendicular to it ($y-$direction), i.e.,

$$\left(\frac{Q_{sh}+Q_a}{Wb}+\frac{ZV\left(b-\epsilon\right)}{bL}\right)\frac{\partial C}{\partial x}+\left(\frac{ZV}{b}-\frac{Z^*V}{b}\right)\frac{\partial C}{\partial y}=D\frac{\partial^2 C}{\partial y^2}, \tag{1.3}$$

with boundary conditions

$$C\left[0,y\right]=C_0\left(H\left[y\right]-H\left[y-\epsilon\right]\right) \text{ and } \lim_{y\to\pm\infty} C\left[x,y\right]=0, \tag{1.4}$$

where Z is the electrical mobility, C_0 is the particle concentration at the inlet, D is the diffusion coefficient, and H is the Heaviside step function. The angle of the target particle streamlines relative to that of the fluid streamlines, θ, does not appear because the high aspect ratio assumption implies that we are in the small angle limit. Physically, the left-hand side of Equation (1.3) captures the effect of the flow and the field on the longitudinal and transverse advection of particles, respectively, and the right hand side captures diffusion relative to the target particle streamlines. As the aerosols of interest populate a band $O(\epsilon)$ in thickness that is far from the walls over most of the device, diffusive deposition to the walls is ignored.

To cast the problem in dimensionless form, the variables $\hat{x} \equiv x/L$, $\hat{y} \equiv y/\epsilon$, and $\hat{C} \equiv C/C_0$ are defined, and the governing equation and boundary conditions are rendered dimensionless to obtain

$$\frac{\partial \hat{C}}{\partial \hat{x}}+\mathcal{R}_{nd}\left(\frac{Z}{Z^*}-1\right)\frac{\partial \hat{C}}{\partial \hat{y}}=\frac{G\mathcal{R}_{nd}^2}{2\mathrm{Pe}}\left(\frac{Z}{Z^*}\right)\frac{\partial^2 \hat{C}}{\partial \hat{y}^2}, \tag{1.5}$$

with

$$\hat{C}\left[0,\hat{y}\right]=H\left[\hat{y}\right]-H\left[\hat{y}-1\right]\ \text{and}\ \lim_{\hat{y}\to\pm\infty}\hat{C}\left[\hat{x},\hat{y}\right]=0, \tag{1.6}$$

where the geometry factor $G=2\left(\mathcal{R}_{nd}+1\right)/\mathcal{R}_{nd}$ and Z^{*} is the target mobility in the kinematic limit. Note that the stipulation that only high aspect ratio devices are considered was employed to justify the assumption that transport owing to the electric field is negligibly small in the direction of the target particle streamlines $\hat{x}$. The migration Péclet number

$$\mathrm{Pe}=\frac{Z^{*}V}{b^{2}}\cdot\frac{b^{2}}{D^{*}}\cdot f=\frac{Z^{*}Vf}{D^{*}}, \tag{1.7}$$

where f is a geometry factor that accounts for nonuniformities in the electric field along the migration pathway, is the ratio of the characteristic time for diffusion to that for the field to displace the target particle the distance of the thin-gap. As only singly charged particles are modeled, $D/D^{*}=Z/Z^{*}$ and $\mathrm{Pe}=eVf/kT$, where e is the elementary charge, k is the Boltzmann constant, and T is the temperature. The geometry factor f is unity for the present planar thin-gap geometry and is generally $O(1)$ for commonly used cylindrical and radial DMAs [23].

For accurate characterization of a particle size distribution, it is optimal to operate at large $\mathcal{R}_{nd}$ and under conditions where diffusive broadening is not significant. For large $\mathcal{R}_{nd}$, the geometry factor of the present minimal model asymptotically approaches a constant

$$\lim_{\mathcal{R}_{nd}\to\infty}G=2, \tag{1.8}$$

which is consistent with the results of Flagan (1999) that showed $G\sim 2$ for the most commonly used DMAs, even when curvature, nonuniformities of the flow, and the finiteness of $\mathcal{R}_{nd}$ are considered in its calculation. Since it is optimal to operate where the performance of the DMA closely approximates its behavior in the kinematic limit, the vast majority of the particles transmitted will be in the range $-1<\mathcal{R}_{nd}\left(Z/Z^{*}-1\right)<1$, or $\left(\mathcal{R}_{nd}-1\right)/\mathcal{R}_{nd}<Z/Z^{*}<\left(\mathcal{R}_{nd}+1\right)/\mathcal{R}_{nd}$. Hence, for $\mathcal{R}_{nd}\gg 1$, the range of mobilities (or, equivalently, diffusion coefficients) of transmit-

ted particles is negligible, or $(\mathcal{R}_{nd}-1)/\mathcal{R}_{nd} \approx (\mathcal{R}_{nd}+1)/\mathcal{R}_{nd} \approx 1$, so the factor of Z/Z^* that multiplies the diffusive term in the governing equation may be taken as unity. In the limit $\mathcal{R}_{nd} \gg 1$, the governing equation becomes

$$\frac{\partial \hat{C}}{\partial \hat{x}} + \zeta \frac{\partial \hat{C}}{\partial \hat{y}} = \frac{\sigma^2_{_{DMA}}}{2} \frac{\partial^2 \hat{C}}{\partial \hat{y}^2}, \tag{1.9}$$

with

$$\hat{C}\left[0, \hat{y}\right] = H\left[\hat{y}\right] - H\left[\hat{y}-1\right] \text{ and } \lim_{\hat{y}\to\pm\infty} \hat{C}\left[\hat{x}, \hat{y}\right] = 0, \tag{1.10}$$

where $\zeta = \mathcal{R}_{nd}\left(Z/Z^* - 1\right)$. The square of the dimensionless diffusion parameter is $\sigma^2_{_{DMA}} = G\mathcal{R}^2_{nd}\left(Z/Z^*\right)/\mathrm{Pe}$ with $G = 2$ and $Z/Z^* = 1$.

This equation can be solved using the convolution and shift theorems for Fourier transforms [25], resulting in the equation

$$\hat{C} = \frac{1}{2}\left(\mathrm{erf}\left[\frac{\zeta\hat{x} + 1 - \hat{y}}{\sqrt{2}\sigma_{_{DMA}}}\right] - \mathrm{erf}\left[\frac{\zeta\hat{x} - \hat{y}}{\sqrt{2}\sigma_{_{DMA}}}\right]\right), \tag{1.11}$$

where erf is the error function. The transmission probability $\Omega_{_{DMA}}$ is obtained by calculating the average concentration of the sample flow outlet relative to that at the inlet, where, for the properly nondimensionalized concentration,

$$\Omega_{_{DMA}} = \int_0^1 \hat{C}\left[1, \hat{y}\right] d\hat{y} = \frac{\sigma_{_{DMA}}}{\sqrt{2}}\left(\mathcal{E}\left[\frac{\zeta+1}{\sqrt{2}\sigma_{_{DMA}}}\right] + \mathcal{E}\left[\frac{\zeta-1}{\sqrt{2}\sigma_{_{DMA}}}\right] - 2\mathcal{E}\left[\frac{\zeta}{\sqrt{2}\sigma_{_{DMA}}}\right]\right), \tag{1.12}$$

where $\mathcal{E}$ is an even function defined by

$$\mathcal{E} = \int \mathrm{erf}\left[u\right] du = u \cdot \mathrm{erf}\left[u\right] + \frac{1}{\sqrt{\pi}} \exp\left[-u^2\right]. \tag{1.13}$$

This result is identical to that of Stolzenburg (1988) for balanced flows, as expected given the similarities of the treatments. Figure 1.3 shows that differences in the diffusion coefficients of transmitted particles, which eventually become nontrivial for finite $\mathcal{R}_{nd}$ operation at low voltages, only become relevant for values of $\sigma^2_{_{DMA}}$ that are far larger than those that are appropriate for high-resolving power classification.

The key difference between the present analysis and previous work is that this

analysis suggests that the diffusional degradation of the resolving power of DMAs with substantially different geometries and operating conditions are identical at constant σ^2_{DMA}. Indeed, the resolving power as a function of σ^2_{DMA} for a broad array of DMAs may be collapsed onto a single master curve, as shown in Fig. 1.4. Note that Flagan (1999) has previously shown that the effects of nonuniformities in the electric field and variations in the velocity profile can be taken into account in the evaluation of the geometry factors, f and G, which correct σ^2_{DMA} to the appropriate value for the conditions under which a real device is used. Thus, while our minimal model was devised for the simplest possible DMA, the result can be applied to DMAs in general.

1.6 A minimal model for the OMAC

The OMAC takes a significant departure from the DMA, replacing the sheath flow with a crossflow that opposes the migration owing to the electric field as is illustrated in Fig. 1.5. The IGMA is closely related to the OMAC and could be modeled analogously to the treatment that is presented here, with modifications for the flow profile and boundary conditions as appropriate for the particular instrument design. Since they are both members of the class of inclined field mobility analyzers, they share the same characteristic scaling of the dimensionless groups that govern their performance. While IGMAs are not treated explicitly here, it should be understood that their performance is substantially similar to OMACs.

In developing a minimal model for the OMAC, we proceed analogously to our work with the DMA in considering the limit of large aspect ratio devices where $L/b \gg 1$, stipulating that $\mathcal{R}_{nd} \gg 1$, and modeling a thin-gap planar channel geometry with negligible variation across the width. In these limits, in the $x-$direction particles are advected by the aerosol/sample flow and diffusion in this direction is negligible owing to the large aspect ratio. Diffusion is, however, important in the thin $y-$dimension, where highly mobile particles with $Z/Z^* > 1$ are displaced in the direction opposite the crossflow while less mobile particles are moved toward the crossflow exit. The target particles with $Z/Z^* = 1$ suffer a drag force that exactly counterbalances the

electrostatic force, so the motion in the $y-$direction is purely diffusive. The dimensionless governing equation is written

$$\hat{u}\left[\hat{y}\right]\frac{\partial\hat{C}}{\partial\hat{x}}-\zeta\frac{\partial\hat{C}}{\partial\hat{y}}=\frac{\sigma_{OMAC}^{2}}{2}\frac{\partial^{2}\hat{C}}{\partial\hat{y}^{2}}, \tag{1.14}$$

with boundary conditions

$$\hat{C}\left[0,\hat{y}\right]=H\left[\hat{y}\right]-H\left[\hat{y}-1\right]\text{ and }\hat{C}\left[\hat{x},0\right]=\hat{C}\left[\hat{x},1\right]=0, \tag{1.15}$$

where $\sigma_{OMAC}^{2}=2\mathcal{R}_{nd}/\mathrm{Pe}$, the walls are taken to be perfect sinks for particles, and, here, $\hat{y}\equiv y/b$. As was the case with the minimal model of the DMA, the migration Péclet number is $\mathrm{Pe}=eVf/kT$, where we note that only singly charged particles are considered and $f=1$ for the parallel plate geometry that is considered here. The dimensionless $\hat{x}-$velocity profile $\hat{u}\left[\hat{y}\right]=u\left[y\right]Wb/Q_{a}$ is taken to be unity everywhere, i.e., we assume plug flow, for simplicity. We immediately see the two key differences between the DMA and the OMAC; (i) the square of the dimensionless diffusion parameter σ^{2} is a factor of $\mathcal{R}_{nd}$ smaller in the OMAC where there is a crossflow than in the DMA where the sheath flow contributes to advection through the classifier; and (ii) diffusive losses out the sides of the channel play an important role in the OMAC since the target particles span the entire thin-gap during their transit and are lost to the porous walls as soon as they diffuse from the channel. The transmission probability can be written as

$$\Omega_{OMAC}=\sum_{n=1}^{\infty}\frac{4n^{2}\pi^{2}\exp\left[-\frac{\sigma_{OMAC}^{2}}{2}\left(n^{2}\pi^{2}+\left(\frac{\zeta}{\sigma_{OMAC}^{2}}\right)^{2}\right)\right]\left(1-(-1)^{n}\cosh\left[\frac{\zeta}{\sigma_{OMAC}^{2}}\right]\right)}{\left(n^{2}\pi^{2}+\left(\frac{\zeta}{\sigma_{OMAC}^{2}}\right)^{2}\right)^{2}}, \tag{1.16}$$

where the concentration was foufnd by the method of separation of variables and then integrated over the outlet to solve for Ω_{OMAC}.

In general, while the velocity profile in the $\hat{y}$ direction is easily rendered uniform by frits or other porous media, the profile across the thin-gap u can vary significantly

from that of plug flow. The Navier-Stokes equations for a fluid of density ρ and kinematic viscosity ν reduce to

$$\mathcal{R}_{nd}\mathrm{Re}\frac{b}{L}\frac{\partial \hat{u}}{\partial \hat{y}} = -\frac{\partial \hat{P}}{\partial \hat{x}} + \frac{\partial^2 \hat{u}}{\partial \hat{y}^2}, \tag{1.17}$$

with no-slip boundary conditions, i.e., $\hat{u}\left[0\right] = \hat{u}\left[1\right] = 0$, where the Reynolds number is $\mathrm{Re} = Q_a/W/\nu$ and the dimensionless pressure $\hat{P} = \left(P - P_o\right)/\Delta P_c$ is scaled viscously, so $\Delta P_c = \rho\nu Q_a L/b^3/W$. In order to obtain an analytical solution, note that it has been stipulated that

$$\left(\frac{b}{L}\right)^2 \ll \frac{1}{\mathcal{R}_{nd}} \text{ and } \left(\frac{b}{L}\right)^3 \ll \frac{1}{\mathcal{R}_{nd}^2\mathrm{Re}}, \tag{1.18}$$

which results in a uniform crossflow velocity profile and renders the nonlinear terms in the Navier-Stokes equations negligibly small. In these limits, the flow profile is found to be [19]

$$\hat{u} = \frac{2\alpha\left(\left(1 - \exp\left[\alpha\hat{y}\right]\right) - \hat{y}\left(1 - \exp\left[\alpha\right]\right)\right)}{2\left(1 - \exp\left[\alpha\right]\right) + \alpha\left(1 + \exp\left[\alpha\right]\right)}, \tag{1.19}$$

where the distortion parameter $\alpha = \mathcal{R}_{nd}\mathrm{Re}\left(b/L\right)$. Since α may vary over a large range, consider the asymptotic behavior of $\hat{u}$. For $\alpha \ll 1$, the effect of $\hat{y}-$momentum on the crossflow is negligible so $\hat{u} \approx 6\hat{y}\left(1 - \hat{y}\right)$, which is parabolic Poiseuille flow. The opposite is true for $\alpha \gg 1$, when the strongly deflected velocity profile $\hat{u} \approx 2\hat{y}$, or simple shear flow, over the domain $y \in [0, 1)$. The effect of nonuniform flow profiles on the transfer function can be found by Brownian dynamics simulation [26, 27]. Figure 1.6 illustrates that, while the effect of nonuniform velocity profiles should not be ignored, the transmission probabilities remain remarkably similar for both limits of α. The quantitative effect of flow nonuniformities and finite $\mathcal{R}_{nd}$ on the observed resolving power are also generally noticeable but manageably small, as is shown in Fig. 1.7.

1.7 Comparing DMAs to OMACs and IGMAs

Since it has been shown that geometry, flow profile, and finite $\mathcal{R}_{nd}$ asymmetries either are easily accommodated by an $O(1)$ constant, or are otherwise altogether negligible, the analysis presented here is applicable to the vast majority of conceivable DMA and OMAC designs. Clearly, the value of the dimensionless group σ^2 plays a critical role in determining the performance of both DMAs and OMACs. Physically, the square of the dimensionless diffusion parameter scales with the ratio of the residence time τ_r to the diffusion time across the target particle streamlines τ_d, or $\sigma^2 \sim \tau_r/\tau_d$. Since it is arguably more intuitive to work in a form that is linearly proportional to the voltage, consider the behavior of $1/\sigma^2 \sim \tau_d/\tau_r \sim V$. For DMAs, $1/\sigma^2_{_{DMA}} \sim \mathrm{Pe}/\mathcal{R}^2_{nd}$ since the target particle streamlines only occupy a fraction $\epsilon/b \sim \mathcal{R}^{-1}_{nd}$ of the gap, resulting in a characteristic diffusion length scale that is quite small relative to the gap thickness for large resolving powers. Because the transit time across the channel is equal to the residence time for those particles that are transmitted through a DMA, the residence time scales inversely with the migration Péclet number. In contrast, OMACs utilize the entire thin-gap for the separation so their diffusion time does not scale with $\mathcal{R}_{nd}$. Additionally, the residence time scales as $\tau_r \sim \mathcal{R}_{nd}/\mathrm{Pe}$ because the unopposed transit time for the target mobility across the thin-gap is a factor of the kinematic resolving power larger than the residence time. The net effect is that, at constant voltage and kinematic resolving power, $\sigma^2_{_{DMA}}\left[V,\ \mathcal{R}_{nd}\right]/\sigma^2_{_{OMAC}}\left[V,\ \mathcal{R}_{nd}\right] \sim \mathcal{R}_{nd}$. Notably, while IGMAs share the same $O(\mathcal{R}_{nd})$ advantage over standard DMAs when the geometry and operating conditions are such that the target particle streamlines span the gap between the electrodes, the velocity profiles may differ from those of OMACs since the electrodes do not provide no-slip boundary conditions.

The diffusive degradation of these classes of methods is also equivalent. As proposed by Flagan (1999), the intersection of the scaling for resolving power degradation in the diffusion-dominated regime with that in the kinematic limit $\mathcal{R}/\mathcal{R}_{nd} \sim 1$ provides a characteristic value of the voltage where diffusion becomes important, as illustrated in Fig. 1.8. Since, in the diffusion-dominated regime, the transfer func-

tion is well approximated by a Gaussian of mean zero and standard deviation σ, $\mathcal{R}/\mathcal{R}_{nd} \sim 1/\left(2\sqrt{2\ln 2}\sigma\right)$ because the 50% confidence interval is $\sqrt{2\ln 2}$ standard deviations. The critical value of

$$1/\sigma_c^2 = 8\ln 2 \approx 5.545 \tag{1.20}$$

then defines a lower bound for near nondiffusive resolving power ($\mathcal{R} \approx \mathcal{R}_{nd}$).

The upper bound of the accessible range of $1/\sigma^2$, which together with the lower bound $1/\sigma_c^2 = 8\ln 2$ defines the dynamic range in mobilities for an instrument run at constant flow rates, is set by the lower of the maximum voltage of the power supply and the voltage V_B at which electrostatic breakdown occurs. At room temperature and atmospheric pressure, electrostatic breakdown occurs at a field strength $E_B \sim 10^6$V/m. This can be used with the electrode spacing, b, to specify $V_B = cbE_B$, where c is a geometry-dependent proportionality constant.

The voltage range alone does not fully specify a mobility analyzer's operating characteristics. The absolute value of one of the flow rates, the geometry of the device, and the mobility of the target particles are also required. The relevant dimensionless group that contains this information is the Graetz number $\mathrm{Gz} = \mathrm{ScRe}\,(b/L)$, where Sc is the Schmidt number $\mathrm{Sc} = \nu/D$. Physically, the Graetz number is a measure of the diffusion time orthogonal to the primary flow to the residence time and is, therefore, similar to $1/\sigma^2$. For DMAs the target particle streamlines only occupy $\epsilon/b \sim \mathcal{R}_{nd}^{-1}$ of the channel, so $\mathrm{Gz}_{DMA}/\mathcal{R}_{nd}^2 \sim 1/\sigma_{DMA}^2$, whereas for OMACs and IGMAs the target particle streamlines may occupy the entire gap between the electrodes, so $\mathrm{Gz}_{OMAC} \sim 1/\sigma_{OMAC}^2$. All target particle information is contained in the Schmidt number; solving for the Schmidt number, therefore, gives the conditions under which particles described by that Schmidt number should be classified. For the minimal models of DMAs and OMACs considered here, the Schmidt number for a particular instrument and flow conditions is given by

$$\mathrm{Sc} = \frac{2}{\sigma^2\kappa}, \tag{1.21}$$

where $\kappa_{DMA} = \mathrm{Re}\,(b/L)\,/\mathcal{R}_{nd}^2$ and $\kappa_{OMAC} = \mathrm{Re}\,(b/L)$, where it should be noted that IGMAs have the same scaling as OMACs. Figure 1.9 illustrates that, for a specified fluid kinematic viscosity, Equation (1.21) may be used to make a general operating diagram for mobility analyzers.

The mobility analyzers that have been built to date have fixed geometries. Common practice for operation is to set the flows and to change the voltage in a stepwise or continuous manner to characterize particles of different electrical mobility. These conventions correspond to holding κ constant while varying $1/\sigma^2$. Figure 1.10 shows the operating range of a TSI Model 3081 DMA run at the common kinematic resolving power of $\mathcal{R}_{nd} = 10$. The diagram is consistent with previous literature, demonstrating that the dynamic range in mobilities is independent of the absolute flow rate and that the device is unable to perform high-resolving power classifications of particles with diameter less than 10 nm. It is reasonable to expect similar agreement between the present asymptotic model that was used to generate the operating diagram and many commonly used DMAs where $f \sim 1$ and $G \sim 2$. In the minimal model of the DMA we set $f = 1$ and $G = 2$, whereas for the TSI 3081 DMA $f = 0.707$ and $G = 2.14$ when $\mathcal{R}_{nd} = 10$ [23].

For a constant kinematic resolving power and dynamic range, OMACs and IGMAs require a maximum voltage that is a factor of $\sigma_{DMA}^2/\sigma_{OMAC}^2 = \mathcal{R}_{nd}$ smaller than DMAs. Decreasing the maximum required voltage allows OMACs with smaller flow chambers to achieve the same quality aerosol classification and dynamic range as larger DMAs. Alternatively, if the kinematic resolving power and the maximum voltage are set, an OMAC or IGMA will have a dynamic range $\mathcal{R}_{nd}$ times that of the equivalent DMA. The $O(\mathcal{R}_{nd}^2)$ advantage in κ, on the other hand, makes it possible to reduce either Re or b/L. Hence, lower absolute flow rates can be used to classify the smallest particles, and devices need not be shortened as much for OMACs or IGMAs as for DMAs in order to classify small, high mobility particles. This explains why, as suggested by modeling results of Flagan (2004), OMACs are capable of much higher resolving powers than DMAs. Alternatively, the potential for small instruments operating at low voltage introduces a number of economies that may allow a paradigm shift in

aerosol measurement strategies.

As shown in Fig. 1.10, the maximum Reynolds number for which flow remains laminar plays a critical role in determining the ability of a particular DEMC design to perform high-resolution classifications of the smallest particles, since this value sets an upper bound on κ. Using specific geometries that promote laminar flow, DMAs have been pushed to Re $\sim 10^5$, nearly two orders of magnitude greater than the lower bound Re $\sim 2 \times 10^3$ of the usual laminar to turbulent transition region. Martinez-Lozano and de la Mora (2006) demonstrated a precision-machined DMA capable of operating at Re $= 6.2 \times 10^4$ with $\kappa_{DMA} \sim 3$ and $\mathcal{R}_{nd} \sim 10^2$, implying an upper bound on $1/\sigma^2 \sim 10$ for this device with $b = 0.005$ m and $L = 0.01$ m. The design maximized κ by operating at large Re and $b/L \sim 1$. In this instrument, $\mathcal{R}/\mathcal{R}_{nd} \sim 1$ for $D_p \sim 1$ nm, as suggested by the general operating diagram presented here. As an aside, the nearly quantitative agreement obtained between the operating diagram constructed from the minimal models presented here and the results of a small aspect ratio, high flow rate device with nonuniform electric fields suggests that the present asymptotic analyses capture much of the relevant physics for DEMCs, despite their simplicity. In designing an OMAC for high resolving power separations of small (ultrafine) particles, $\kappa_{OMAC} = 3$ could be achieved for Re $= 30$ and $b/L = 1/10$, far more forgiving design specifications than required in the elegant DMA design of Martinez-Lozano and de la Mora (2006). The predicted upper bound becomes $1/\sigma^2 \sim 2 \times 10^2$ for an instrument operated at $\mathcal{R}_{nd} = 10^2$ with $b = 0.001$ m, indicating considerable dynamic range with a compact device. The favorable scaling characteristics of OMACs and IGMAs relative to DMAs hold promise for new designs that could have substantially larger dynamic ranges for high resolution classification of ultrafine particles. Note that the upper bounds of Re for OMACs, where the nonlinear terms that appear in the Navier-Stokes equations may affect the transition to turbulence or otherwise alter the flow profile from the analytical form presented here, are generally not known at present for all conceivable designs. However, as demonstrated in the comparison above, the required Reynolds numbers are much lower. The upper bound of Re for IGMAs is also unknown at present. For many designs the proper Reynolds number

for IGMAs from the perspective of flow stability is that of the separation gas flow, which is a factor of $\mathcal{R}_{nd}$ larger than that of the aerosol flow considered here. Although the limits of accessible Re are generally unknown at present, the favorable scaling in κ relative to DMAs nonetheless suggests that OMAC and IGMA designs may even enable DEMCs to peer into the sub-nanometer range of small molecules, opening the door to an array of new applications ranging from front-end purification of samples going to mass-spectrometers to monitoring for dangerous airborne chemicals in the field or use, as demonstrated by Tammet (2011), as an airborne-ion detector.

Another approach to extending the dynamic range that may seem particularly appealing for high mobility, ultrafine particles is to design instruments that can be operated at voltages where $1/\sigma^2 < 1/\sigma_c^2$. However, unlike DMAs, the target particle streamlines occupy the entire flow channel of the OMAC, leading to a loss of transmission efficiency at low resolving power. This can introduce new challenges with counting statistics. The transmission efficiency η is the ratio of the integral of the diffusive transfer function over mobility space to that of the kinematic transfer function, or

$$\eta\left[1/\sigma^2\right] = \int_{-\infty}^{\infty} \Omega\left[1/\sigma^2, \zeta\right] d\zeta. \tag{1.22}$$

As shown in Fig. 1.11, the efficiency drops precipitously below $1/\sigma_c^2$ for OMACs due to diffusive losses to the walls. In contrast, the target particle streamlines occupy only a fraction, $\epsilon/b \sim \mathcal{R}_{nd}^{-1}$, of the DMA. Since those streamlines are far from the walls except for very close to the inlet and outlet, DMAs do not suffer the same efficiency losses within the classification region. OMACs could be designed to minimize these losses by allowing sheath flows to isolate the particles of interest from the walls. However, because OMACs in which target particle streamlines do occupy the entire device exhibit the simplest scaling, we do not consider their alternatives here. Hence, for the DMA there is a tradeoff between resolving power and dynamic range that can be considered on an application-specific basis, whereas, for the OMAC efficiency losses generally prevent operation significantly below the voltage that corresponds to $1/\sigma_c^2$. The governing dimensionless groups for these methods are summarized in Table

1.1 to facilitate direct comparison between DMAs and OMACs/IGMAs. It should be noted that IGMAs share the same scaling advantages as OMACs in $1/\sigma^2$ and κ over standard DMAs but may be able to maintain larger efficiencies at smaller values of $1/\sigma^2$ providing particle deposition on the electrodes is not problematic.

OMACs and IGMAs differ from DMAs in how they scan in electrical mobility space. The electrical mobility targeted in a DMA can be changed smoothly by changing the operating voltage, with resolution determined by diffusion. By eliminating the equilibration time between voltages in stepping-mode (DMPS) operation of the DMA, temporal resolution can be dramatically improved. Additionally, this scanning-mode (SMPS) operation of the DMA achieves this acceleration without loss of sensitivity, provided the detector counting time is not shortened from that used in stepping-mode operation. In contrast, scanning-mode operation of the OMAC or IGMA will result in enhanced particle losses unless either the electric field or the crossflow velocity is varied with position along the classification channel to maintain the balance between electrical migration and the crossflow along the entire particle path. This would introduce additional complexity to the OMAC or IGMA design, particularly if variable scan rates were to be accommodated. This might be ameliorated by making OMACs or IGMAs in which the target particle streamlines occupy only a fraction of the flow chamber, i.e., by developing a hybrid between the DMA and the OMAC. Because creating finely controlled time-varying spatially nonuniform electric fields is more difficult than controlling a single uniform voltage in time, for scanning applications, DMAs have an advantage over those OMACs in which target particle streamlines occupy the entire device. It should be noted, however, that the SIGMA of Tammet (2011) does employ a scanning mode and still attains reasonable resolving power. Moreover, because the OMAC/IGMA allows smaller instruments to be built, the time penalty associated with stepping-mode operation may be smaller than in the DMA.

Finally, additional comparison between OMACs and IGMAs is merited as it has been noted that they share the same scaling advantages over standard DMAs. While an OMAC of fixed geometry may be operated at arbitrary $\mathcal{R}_{nd}$ by simply changing

the ratio of the flow rates, IGMAs operate optimally at a value of $\mathcal{R}_{nd}$ that is specified by the angle formed between the electric field and the fluid streamlines, the distance between the electrodes, and the length of the classification region. For many applications, this is not problematic as a fixed $\mathcal{R}_{nd}$ will suffice. The maximum obtainable value of Re before the flows become unstable may be different for OMACs and IGMAs, depending on the details of the respective designs. IGMAs hold a great deal of promise for the classification of ultrafine particles and gas ions owing to the favorable scalings over standard DMAs. OMACs share in these favorable scalings and also have additional flexibility in their design and operation.

1.8 Conclusions

The minimal models presented here for DMAs and OMACs elucidate the key dimensionless groups that govern their performance. The well-known kinematic resolving power $\mathcal{R}_{nd}$ and the new quantity $1/\sigma^2$ fix the resolving power of a particular classification, while a third parameter, κ, describes the flow rates at which that classification can be accomplished. The accessible range in $1/\sigma^2$ and κ of a mobility analyzer at a fixed $\mathcal{R}_{nd}$ provides a quantitative measure of the its dynamic range in mobilities both for fixed flows (constant κ) and for fixed voltages (constant $1/\sigma^2$). By examining the physical limits of these quantities, one can create operating diagrams capable of describing a base case of performance of most custom and commercially available designs. Furthermore, these operating diagrams can be used as theoretical design aids.

Compared to DMAs, OMACs and IGMAs were shown to have superior scaling with increasing kinematic resolving power, with a factor of $\mathcal{R}_{nd}$ edge in $1/\sigma^2$ and a factor of $\mathcal{R}_{nd}^2$ advantage in κ. This increases the flexibility of design in miniaturization and dynamic range in mobility classifier design. The OMAC and the IGMA also open new doors for DEMCs that classify particles with $D_p < 10$ nm, with the particularly exciting prospect of extending down to $D_p < 1$ nm. Offering a broad dynamic range and unprecedentedly high $\mathcal{R}$, OMACs and IGMAs may even be used

as front-ends to mass-spectrometers for small-molecule detection, so long as the operating conditions are such that $1/\sigma^2 > 1/\sigma_c^2$ so that the efficiency $\eta \sim 1$. Beyond having a sufficiently large efficiency, for field deployable OMACs and IGMAs or, for that matter, DMAs to be more broadly used, inexpensive, miniature detectors with excellent sensitivities must be developed. While the DMA will likely continue to play a critical role in aerosol measurements, particularly with respect to measurement speed as fast-response detectors become available, the OMAC and the IGMA have distinct advantages that should enable them to expand the ways that mobility methods can be used in broader studies into the effects of aerosols on the climate and human health.

1.9 Figures

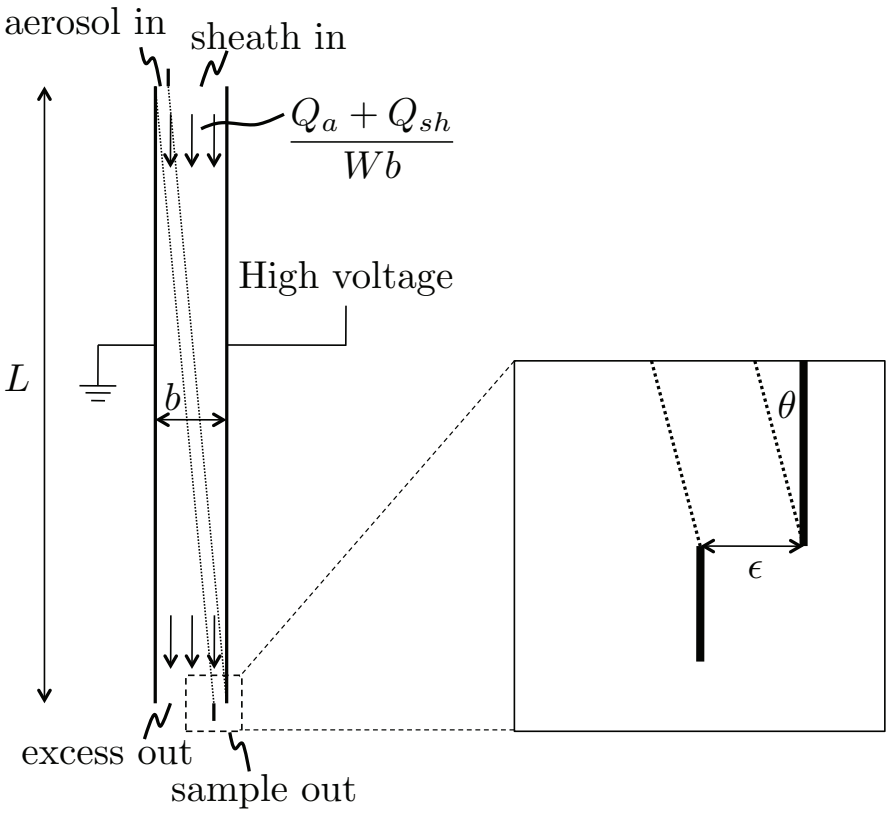

Figure 1.1. A thin-gap differential mobility analyzer, with emphasis put on the bounds of target particle streamlines. A pressure-driven flow introduces particle-free sheath air at a flow rate of Q_{sh} over $(b-\epsilon)\,W$ of the inlet, with the aerosol entering at a rate of Q_a over the surface area ϵW (there is no variation along the width, so a two-dimensional drawing is shown here). As they are advected down the channel, charged particles are deflected across the gap by an electric field. Target particles of mobility Z^* follow particle streamlines that extend from the aerosol inlet to the sample outlet. For balanced flows, this corresponds to crossing over the separation gas fluid streamlines that populate a thickness $b-\epsilon$ of the gap b. In the large aspect ratio, large kinematic resolving power limits considered here, the target particle and fluid streamlines form the small angle $\theta \ll 1$.

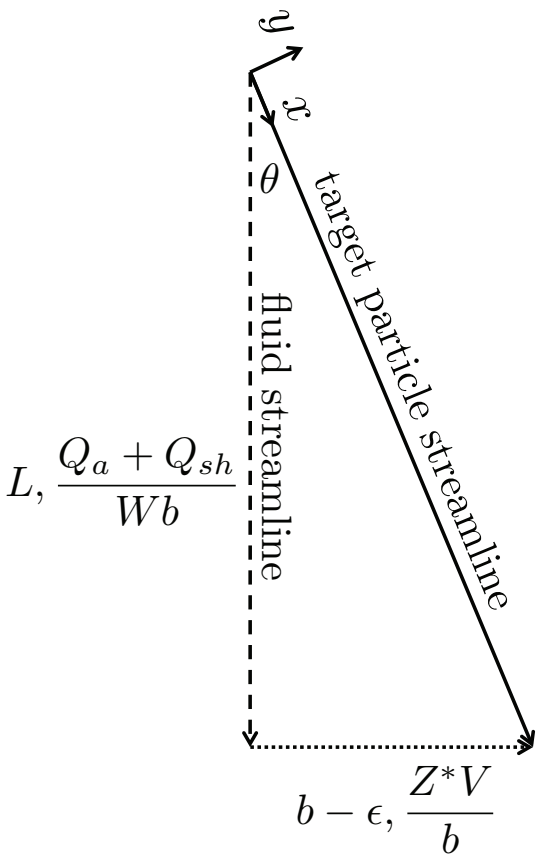

Figure 1.2. A fluid streamline that originates at the aerosol inlet is shown with a target particle streamline to illustrate the coordinate system that is chosen and critical dimensions and velocities in the DMA. The dimensions are exaggerated for the purpose of illustration; here the small angle limit $\theta \ll 1$ is considered.

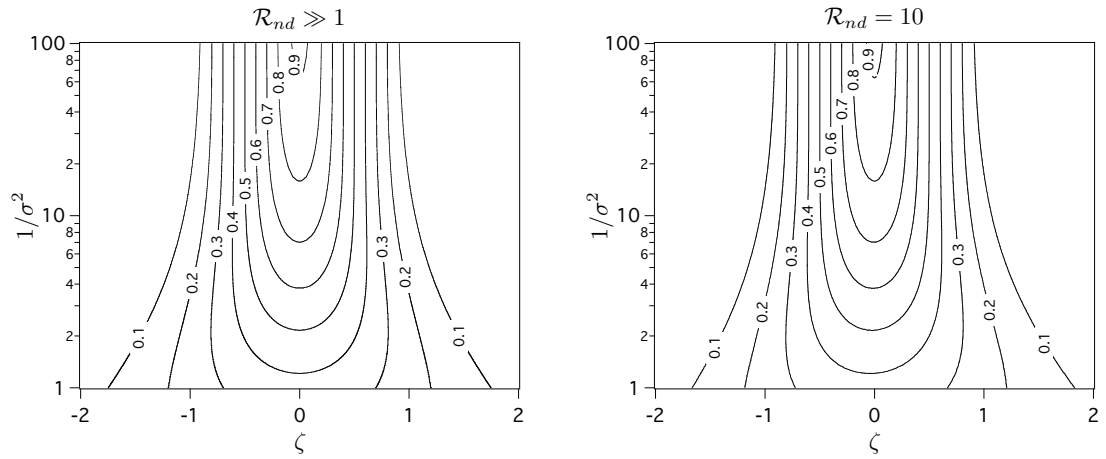

Figure 1.3. Transfer functions for differential mobility analyzers with $\mathcal{R}_{nd} \gg 1$ and $\mathcal{R}_{nd} = 10$. For large $1/\sigma^2$, the performance closely approximates the triangular kinematic limit and, significantly, the asymptotic behavior for $\mathcal{R}_{nd} \gg 1$ is recovered even for a moderate value of $\mathcal{R}_{nd} = 10$. As diffusive degradation becomes more important, the transfer function broadens. At finite $\mathcal{R}_{nd}$, differences in the diffusion coefficients of transmitted particles yield a slightly asymmetric transmission probability as a function of $\zeta = \mathcal{R}_{nd}\,(Z/Z^* - 1)$ at sufficiently small $1/\sigma^2$, as can be seen here for $\mathcal{R}_{nd} = 10$.

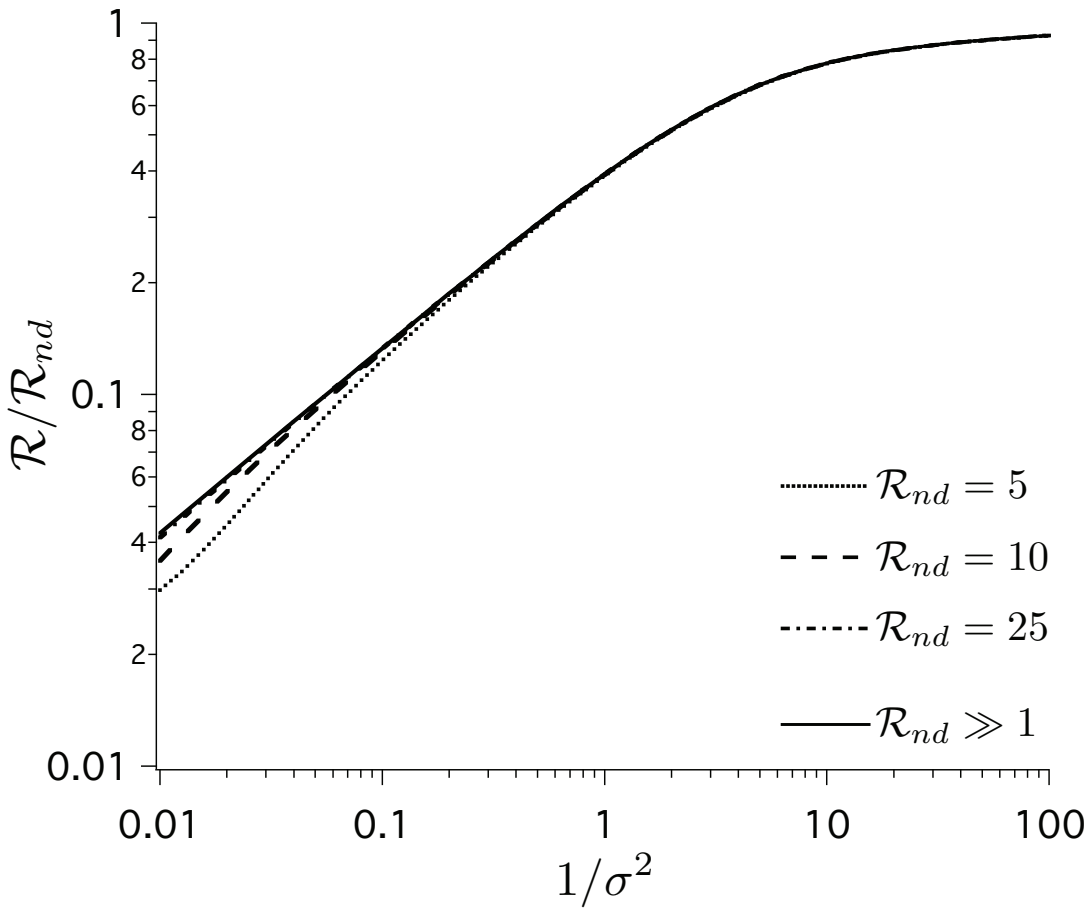

Figure 1.4. Degradation of resolving power for DMAs. Geometric and velocity profile details are wrapped up into the square of the dimensionless diffusion parameter σ^2, so performance is only a function of the kinematic resolving power $\mathcal{R}_{nd}$, the ratio of the sheath to the aerosol flow rate. Excellent agreement between finite $\mathcal{R}_{nd}$ and the asymptotic $\mathcal{R}_{nd} \gg 1$ behavior is observed for large $1/\sigma^2$, where the observed resolving power asymptotically approaches $\mathcal{R}_{nd}$. Deviations are observed at small $\mathcal{R}_{nd}$ and $1/\sigma^2$, where differences in the diffusion coefficients of the transmitted aerosols result in asymmetric transfer functions and, hence, quantitatively small differences from $\mathcal{R}_{nd} \gg 1$ performance.

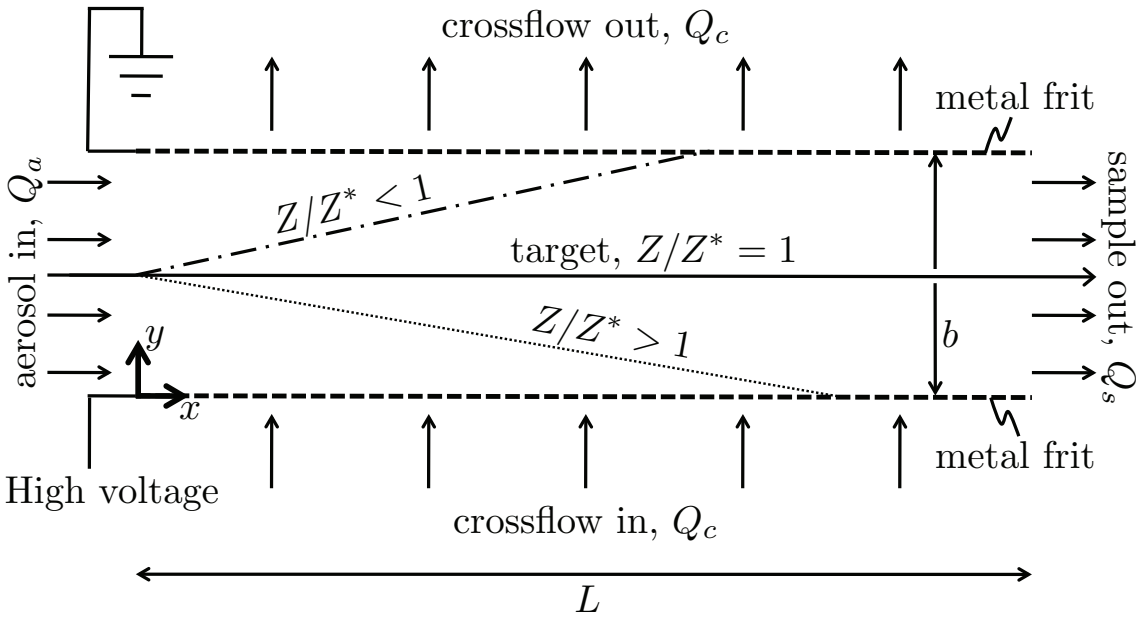

Figure 1.5. A planar OMAC with three particle streamlines originating at the center of the aerosol inlet to illustrate its behavior. Aerosol is introduced to the channel at a flow rate Q_a and sample is continuously collected at the other end at a rate of $Q_s = Q_a$. As with DMAs, an orthogonal electric field is used to deflect particles. The OMAC has a crossflow Q_c that counteracts the displacement owing to the electric field. Target particles proceed directly from the aerosol inlet to the sample outlet, with high and low mobility contaminants rejected through the sides. While three representative particle streamlines that originated at the center of the aerosol inlet are shown, it should be noted that particles are introduced uniformly over the entire cross section of the inlet.

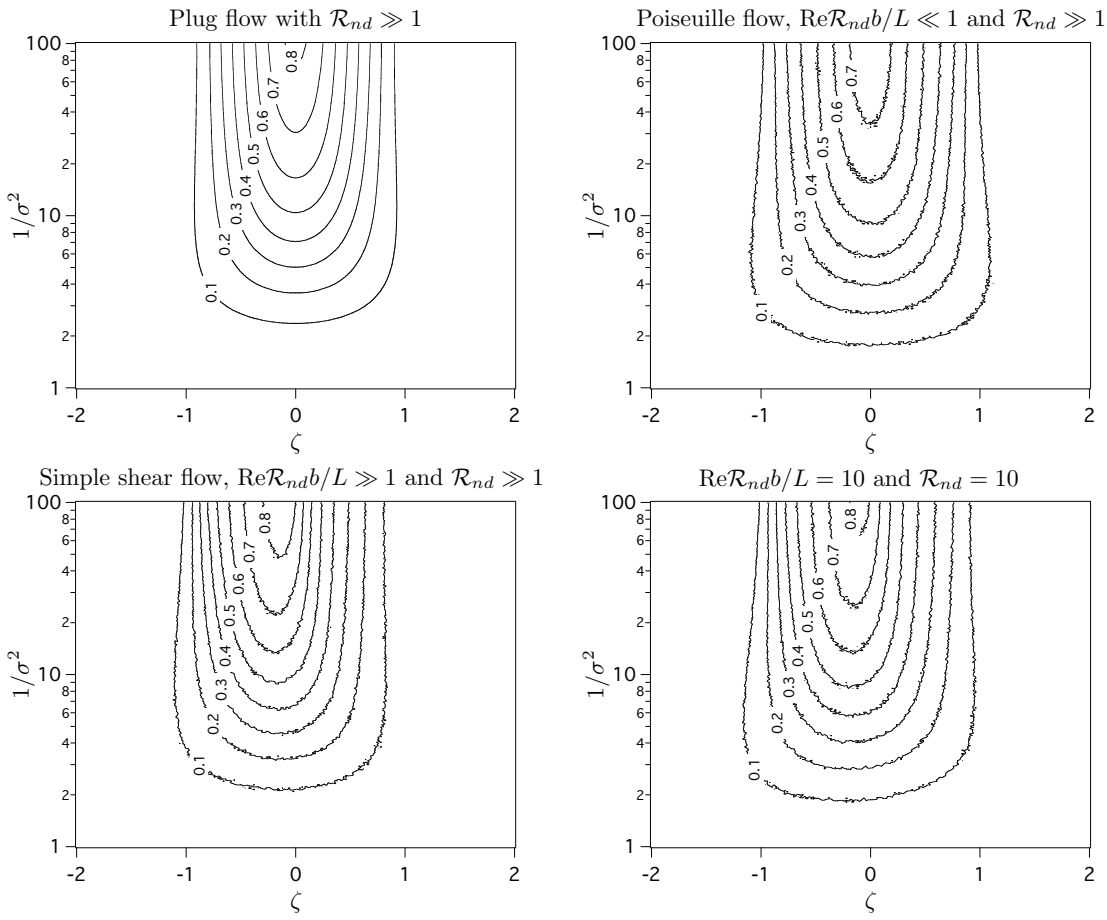

Figure 1.6. Transfer functions for opposed migration aerosol classifiers. Brownian dynamics simulation is used to compare the performance with nonuniform velocity profiles to that of plug flow, which is found by separation of variables. Distortion of the transfer functions is generally small at sufficiently large $1/\sigma^2$. Notably, for simple shear flow the mobility of maximal transmittance shifts from the target mobility, an effect that must be taken into account for accurate characterization of an aerosol size distribution.

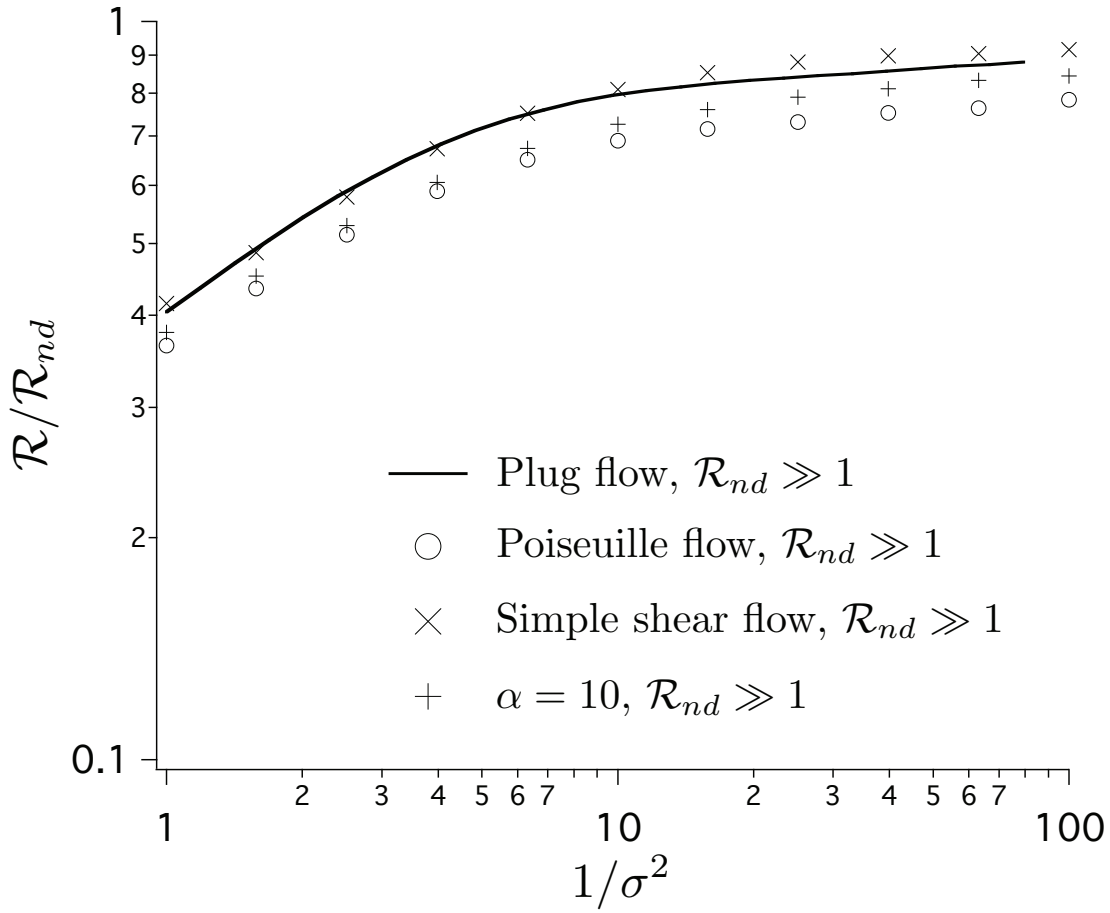

Figure 1.7. Effect of aerosol flow velocity profile on resolving power of OMAC. As the OMAC model presented here does not incorporate the effect of the velocity profile into σ^2 (as was done with DMAs via the constant G), the specific flow profiles have a finite effect on the resolving power relative to the plug-flow base-case. Qualitatively, the behaviors are similar, with the resolving power increasing monotonically with $1/\sigma^2$ to asymptotically approach $\mathcal{R}/\mathcal{R}_{nd} = 1$. While detailed quantitative deviations should be included in rigorous comparisons between theory and experiment, the plug-flow performance is representative from a perspective of a conceptual design.

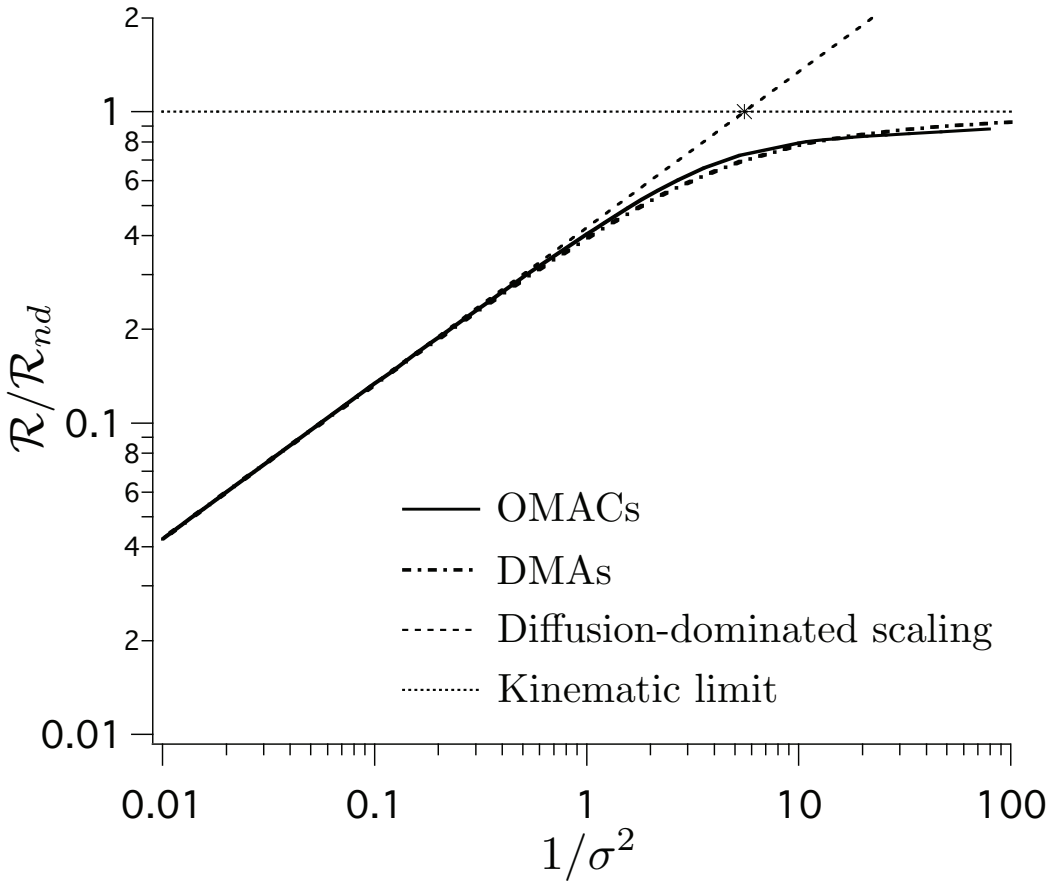

Figure 1.8. Degradation of the resolving power for DMAs and OMACs as predicted by minimal plug-flow models with $\mathcal{R}_{nd} \gg 1$. Significantly, proper scaling results in the collapse of DMA and OMAC performance onto a single curve. A quantitatively small deviation is a result of the diffusive wall deposition that OMACs suffer, an effect that is negligible for DMAs. The performance of an IGMA would be substantially similar with minor modifications depending on the degree to which the electrodes act as particle sinks. The intersection of the asymptotic scalings provides a critical value $1/\sigma_c^2 \approx 5.545$ (marked by an asterisk) that is interpreted as the boundary between the $1/\sigma^2 < 1/\sigma_c^2$ diffusion-dominated regime and the operating region $1/\sigma^2 > 1/\sigma_c^2$ where the resolving power closely approximates that of the kinematic limit.

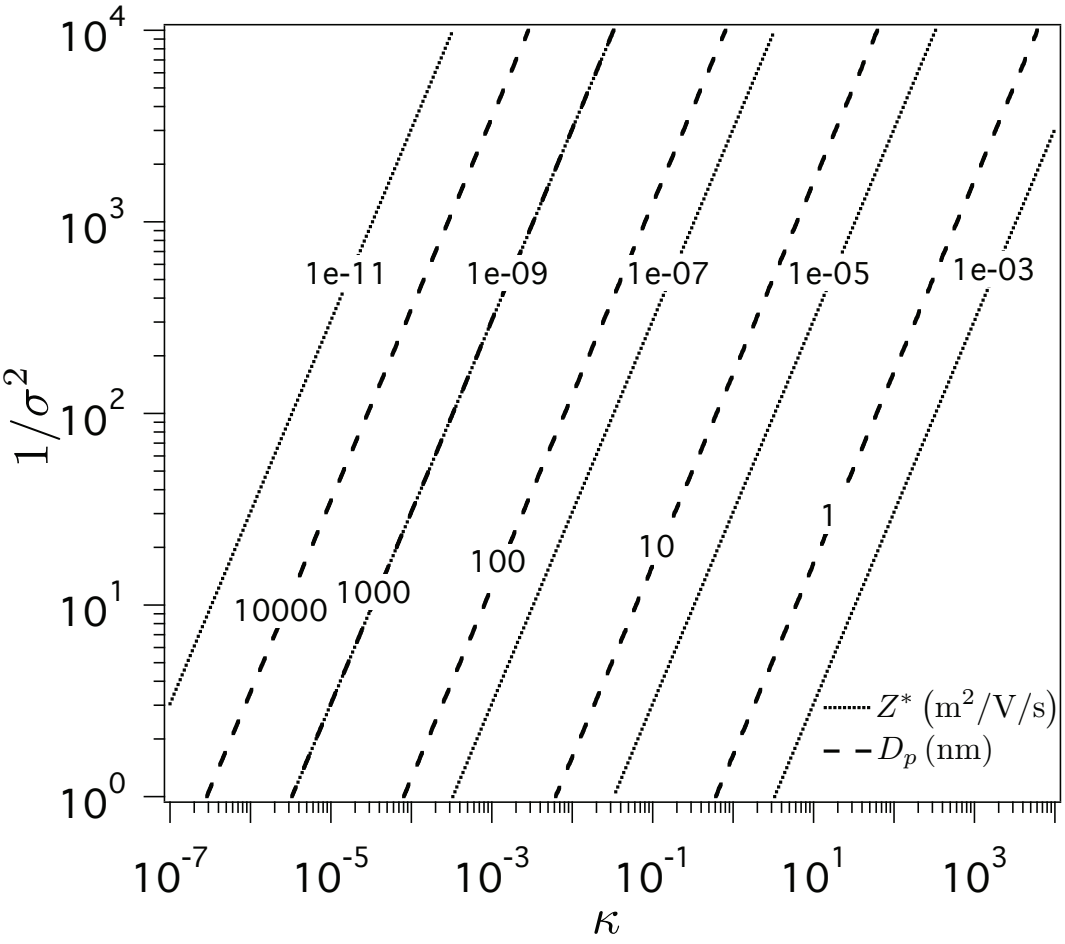

Figure 1.9. General operating diagram for mobility analyzers at room temperature and atmospheric pressure. Lines of constant mobility and diameter are plotted as a function of κ, which is proportional to the aerosol flow rate, and $1/\sigma^2$, which is proportional to the voltage. Typically, DMAs are operated at constant flow rates (fixed κ), and the accessible dynamic range is sampled by scanning or stepping in voltage (changing $1/\sigma^2$), although scanning-flow DMAs have been developed to extend the dynamic range [28].

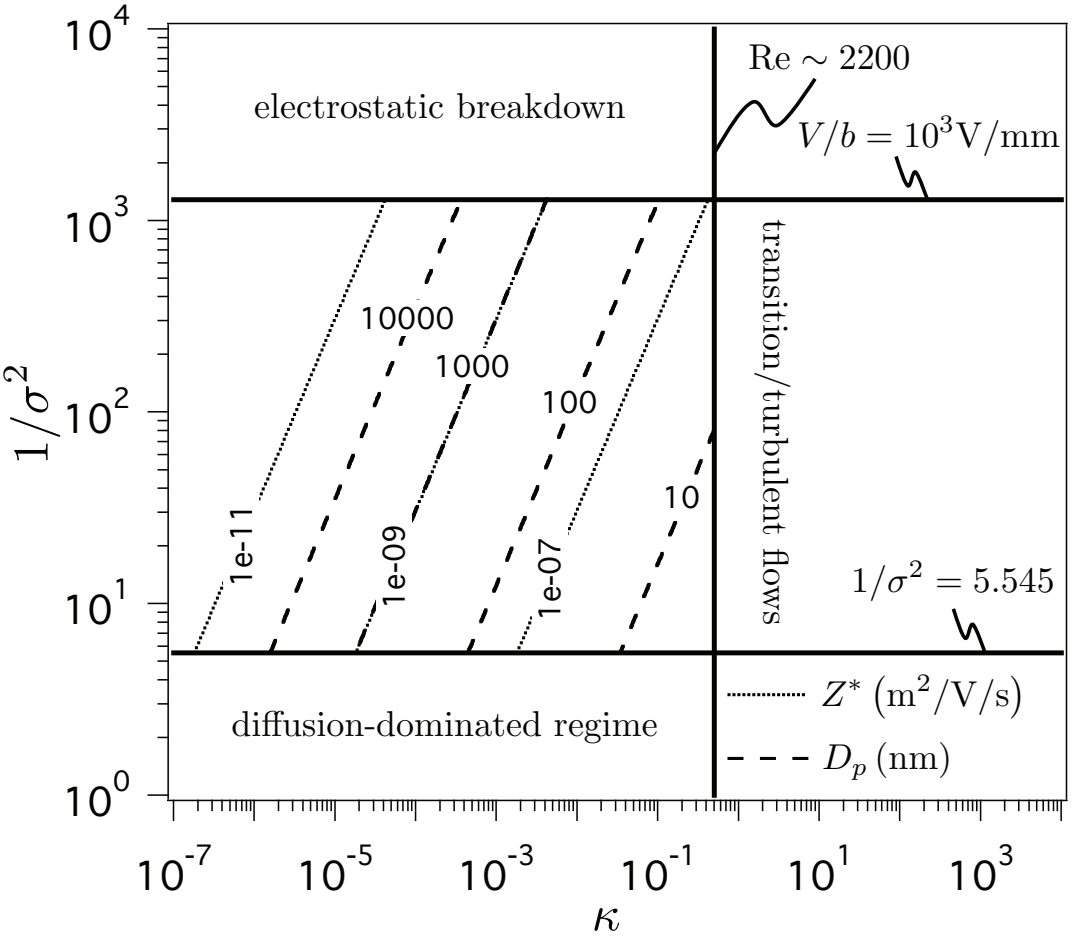

Figure 1.10. Operating diagram of a TSI Model 3081 (long) DMA for a kinematic resolving power $\mathcal{R}_{nd} = 10$ at room temperature and atmospheric pressure. The operating range of any DMA, OMAC, or IGMA may be found by demarcating the boundaries in κ and $1/\sigma^2$ on the general operating diagram. The maximum value of κ and the accessible range of $1/\sigma^2$ are completely specified by the device geometry and the setpoint for $\mathcal{R}_{nd}$. Note that increasing $\mathcal{R}_{nd}$ by an order of magnitude shifts the upper bounds of $1/\sigma^2$ and κ down two orders of magnitude as they are proportional to the inverse of the square of the kinematic resolving power. Increasing $\mathcal{R}_{nd}$ by an order of magnitude for an equivalent OMAC/IGMA shifts the upper bound of $1/\sigma^2$ down by an order of magnitude and does not affect the limit in κ, a relatively small sacrifice in dynamic range relative to the strongly unfavorable scaling of DMAs.

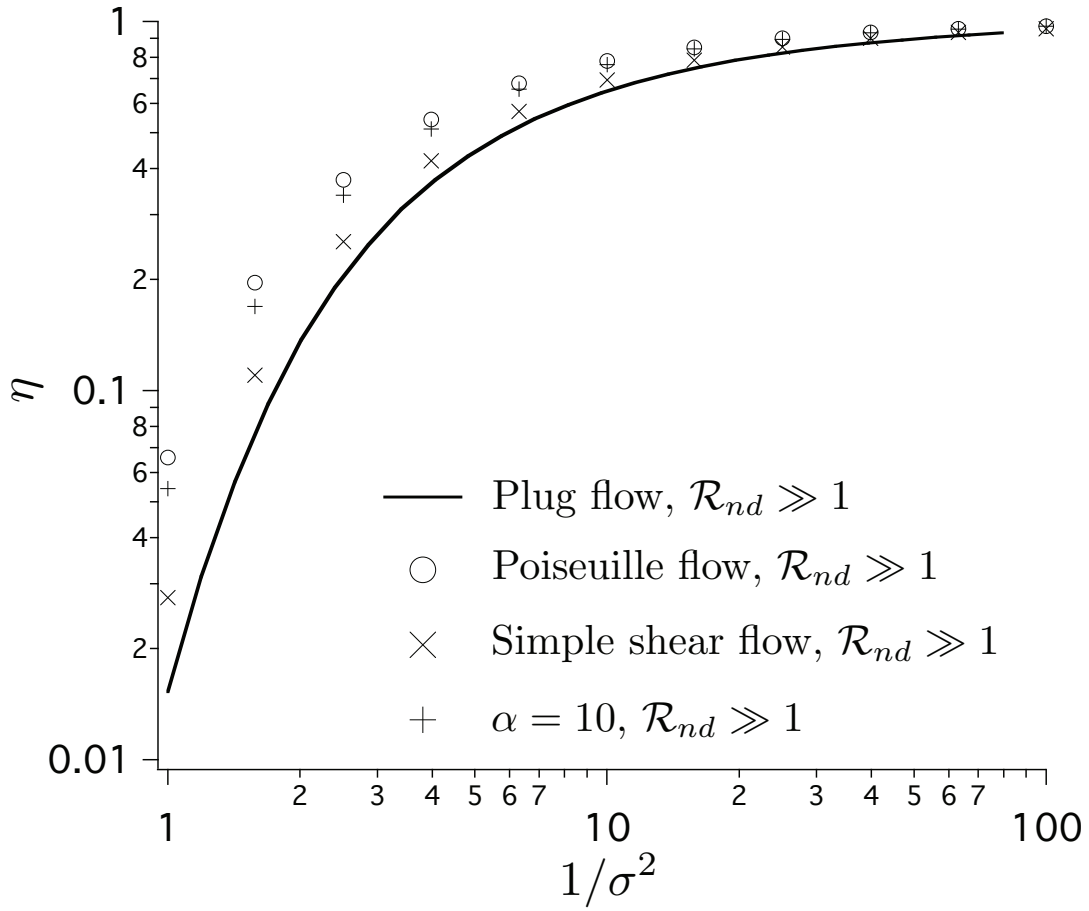

Figure 1.11. Efficiency η of OMACs in which target particle streamlines occupy the entire device. When diffusion becomes important at low $1/\sigma^2$, η drops due to wall losses. Significantly, in the kinematic operating region where $1/\sigma^2 > 1/\sigma_c^2 \approx 5.545$, $\eta \sim 1$. Hence, the reduced efficiency relative to DMAs (where η is unity everywhere) is only relevant if diffusive degradation of the resolving power is *also* acceptable for a particular application.

1.10 Table

Table 1.1. Scaling of dimensionless groups that govern the performance of mobility analyzers.

Name	**Symbol**	**DMAs**	**OMACs/IGMAs**	**Advantage**
Inverse square of the dimensionless diffusion parameter	$1/\sigma^2$	$\mathrm{Pe}/\left(2\mathcal{R}_{nd}^2\right)$	$\mathrm{Pe}/\left(2\mathcal{R}_{nd}\right)$	OMACs/IGMAs by $O(\mathcal{R}_{nd})$
Flow parameter	κ	$\mathrm{Re}\left(b/L\right)/\mathcal{R}_{nd}^2$	$\mathrm{Re}\left(b/L\right)$	OMACs/IGMAs by $O(\mathcal{R}_{nd}^2)$
Efficiency	η	1 everywhere	1 for $\frac{1}{\sigma^2} > \frac{1}{\sigma_c^2}$	DMAs for small $1/\sigma^2$

Chapter 2

A Planar Opposed Migration Aerosol Classifier

2.1 Abstract

We present data from a planar opposed migration aerosol classifier (OMAC) that demonstrate classification of aerosol over a dynamic range of mobilities that spans three orders of magnitude. Mobility standards from 1.47 nm to 92 nm were classified at a resolution of 5 or better with the handheld prototype. The lessons learned from the validation of the planar OMAC have motivated the design of a radial geometry version, which is currently under development in the Flagan Laboratory at Caltech.

2.2 Introduction

The differential mobility analyzer (DMA) of Knutson and Whitby (1975) has been widely used for ambient and chamber studies to investigate the nucleation, growth, and aging of aerosols and their effects on the environment. The success of this and similar long column cylindrical devices inspired the development of short column variants [8], as well as more radical departures such as the meticulously crafted high resolution DMAs of de la Mora and coworkers [10, 11, 12] and radial DMAs [7, 13]. Taken together, the array of custom-made and commercially available DMAs is capable of high resolving power classification of particles from 1 nm to 1 μm. When operated in scanning mode [2], these DMAs can be used to obtain the size distribution for their entire dynamic range of electrical mobilities in under a minute, or in a matter of a few seconds with fast response detectors [3, 4].

Theoretical work on inclined field DMAs [15], followed by promising simulation results [19], suggested that the application of an electric field that is inclined relative to the fluid streamlines, a configuration that does not easily lend itself to operation in scanning mode, may nonetheless be preferable to classic DMAs for applications that require small device footprints, sub-2 nm classification, large dynamic ranges of mobilities, and high resolving powers, but can tolerate time resolution on the order of minutes. The inclined grid mobility analyzer (IGMA) was the first inclined field instrument to be made. The IGMA has been shown to classify clusters, gas ions, and small nanometer particles from 0.4 to 7.5 nm, a broad dynamic range in mobilities, at a resolution of about 3 [17, 18]. The excellent performance of the IGMA arises from favorable scalings of the governing dimensionless parameters relative to classic DMAs [29].

The opposed migration aerosol classifier (OMAC) is an inclined field mobility analyzer that has the same favorable scalings as the IGMA. The differences between the OMAC and the IGMA arise from the roles that the electrodes are intended to play. With the IGMA, the electrodes are not meant to affect the fluid velocity profile, whereas with the OMAC the electrodes are used to render the crossflow uniform. The consequences of this difference in design are detailed in Fig. 2.1.

Here, a prototype planar OMAC is introduced and its performance is characterized. We first review the theoretical performance of the device. The design details of the prototype OMAC used in this study are then described. Next, results from characterization experiments with size standards that are nearly monodisperse (i.e., polystyrene (PSL) size standards) as well as measurements made in tandem with instruments with known performance characteristics are presented and discussed. Finally, we comment on the lessons learned from the development and testing of this prototype and make several recommendations for improved design features for future OMAC instruments.

2.3 Theory

Consider a planar OMAC of length L and electrode spacing b, as shown in Fig. 2.2. Variations across the width, which is of extent W, are ignored here in this minimal plug flow (uniform velocity) model. The flows are balanced, so the aerosol flow Q_a is equal to the exiting classified sample flow Q_s. The entering and exiting crossflows are both equal to Q_c. A useful metric of the performance of this and many other differential electrical mobility classifiers is the resolving power, $\mathcal{R} = Z^*/\Delta Z_{FWHM}$, where Z^* is the mobility of maximal transmittance and ΔZ_{FWHM} is that full width at half maximum of the transfer function. As was the case for DMAs, the nondiffusive resolving power is the ratio of the separation gas flow to that of the aerosol, $\mathcal{R}_{\text{nd}} = Q_c/Q_a$. The behavior of the diffusive planar plug flow OMAC is governed by the convective-diffusion equation. At steady-state, aerosol is advected through the channel in the x-direction by the primary (aerosol/sample) flow. In the y-direction, displacement by the crossflow is counteracted by that of the electric field, where the target electrical mobility is defined by $Z^* = Q_c b/\left(VWL\right)$, the value where the electrical displacement exactly counteracts the crossflow displacement, where V is the applied potential difference. For large aspect ratio devices where $\left(L/b\right)^2 \gg 1$, which is stipulated here, diffusion is negligible in the x-direction, but merits consideration in the thin y-direction that is aligned with the field. For plug flow, the convective-diffusion equation is then written

$$\frac{Q_a}{Wb}\frac{\partial C}{\partial x} + \left(\frac{Q_c}{WL} - \frac{ZV}{b}\right)\frac{\partial C}{\partial y} = D\frac{\partial^2 C}{\partial y^2}, \tag{2.1}$$

with boundary conditions

$$C\left[0,y\right] = C_0\left(H\left[y\right] - H\left[y-b\right]\right) \text{ and } C\left[x,0\right] = C\left[x,b\right] = 0. \tag{2.2}$$

Here, Z is the electrical mobility of the particle of interest, D is its diffusion coefficient, C_0 is its concentration at the aerosol inlet, V is the applied voltage, H is the Heaviside step function, and the porous walls are taken to be perfect particle sinks.

The governing equation and its boundary conditions may be rendered dimensionless by defining the variables

$$\hat{C} = C/C_{_0},\ \hat{x} = x/L,\ \text{and}\ \hat{y} = y/b, \tag{2.3}$$

substituting them in Eqs. (2.1) and (2.2), and rearranging to obtain

$$\frac{\partial \hat{C}}{\partial \hat{x}} - \zeta \frac{\partial \hat{C}}{\partial \hat{y}} = \frac{\sigma^2}{2}\left(\frac{Z}{Z^*}\right)\frac{\partial^2 \hat{C}}{\partial \hat{y}^2}, \tag{2.4}$$

with

$$\hat{C}\left[0, \hat{y}\right] = H\left[\hat{y}\right] - H\left[\hat{y} - 1\right]\ \text{and}\ \hat{C}\left[\hat{x}, 0\right] = \hat{C}\left[\hat{x}, 1\right] = 0, \tag{2.5}$$

where $\zeta = \mathcal{R}_{\text{nd}}\left(Z/Z^* - 1\right)$ and the square of the dimensionless diffusion parameter is $\sigma^2 = 2\mathcal{R}_{\text{nd}}/\text{Pe}$. The migration Péclet number Pe is the ratio of the characteristic time for diffusion to that for the field to displace a particle the distance of the gap in the absence of a crossflow. Here, $\text{Pe} = eV/kT$, where e is the elementary charge, k is the Boltzmann constant, and T is the absolute temperature, as only singly charged particles are considered.

The transmission probability may then be found by solving for the concentration by separation of variables, and then integrating the concentration over the outlet to obtain the probability that a particle of mobility Z will be transmitted when targeting particles of mobility Z^*. This probability, which is known as the instrument transfer function Ω, can be found by separation of variables to be

$$\Omega = \sum_{n=1}^{\infty} \frac{n^2\pi^2\sigma^4}{\lambda_n^4}\left(\frac{Z}{Z^*}\right)^2 \exp\left[-\lambda_n^2\right]\left(1 - (-1)^n \cosh\left[\frac{\zeta}{\sigma^2\left(Z/Z^*\right)}\right]\right), \tag{2.6}$$

where the eigenvalues are

$$\lambda_n^2 = \frac{\sigma^2}{2}\left(\frac{Z}{Z^*}\right)\left(n^2\pi^2 + \left(\frac{\zeta}{\sigma^2\left(Z/Z^*\right)}\right)^2\right). \tag{2.7}$$

As is commonly the case with transport phenomena, the most interesting part of

modeling the OMAC is in the scaling analysis. The Schmidt number, $\mathrm{Sc} = \nu/D^*$, where ν is the kinematic viscosity and D^* is the diffusion coefficient of the target particle, is a function only of σ^2 and a dimensionless flow parameter $\kappa = \mathrm{Re}b/L$, where Re is the Reynolds number, and the relationship is

$$\mathrm{Sc} = \frac{2}{\sigma^2 \kappa}. \tag{2.8}$$

Since ν is only a function of the gas composition, temperature, and pressure, and the Stokes-Einstein-Sutherland relationship relates D^* to the particle diameter D_p, a general operating diagram that has D_p as a function of σ^2 and κ may be made once the gas properties are defined [29]. Beyond enabling the construction of a general operating diagram for the OMAC, the dimensionless groups σ^2 and κ govern the performance of many differential electrical mobility classifiers. It has been shown theoretically that both scale favorably for OMACs (and IGMAs) relative to DMAs as a function of the the nondiffusive resolving power $\mathcal{R}_{\mathrm{nd}}$, with an $O(\mathcal{R}_{\mathrm{nd}})$ edge in σ^2 and an $O(\mathcal{R}_{\mathrm{nd}}^2)$ advantage in κ [29]. The testing of the present and future OMAC instruments enables the experimental validation of this theoretical result.

The theoretical value of σ^2 represents a lower bound, ideal value of the square of the dimensionless diffusion coefficient for real instruments. Nonidealities, such as imperfections in the fabricated components and field nonuniformities near edges, give rise to greater dispersion than that predicted by theory. The practice in the field has been to account for all nonidealities with an empirical multiplicative factor f_σ ([21]; see also [30]) or an additive distortion factor σ_{distor}^2, i.e., $\sigma_{obs} = f_\sigma \sigma$ or $\sigma_{obs}^2 = \sigma^2 + \sigma_{distor}^2$, where σ_{obs}^2 is the experimentally observed (fitted) square of the dimensionless diffusion parameter.

The utility of a mobility classifier is also influenced by the efficiency with which particles that enter the instrument are counted. Losses within the DMA occur primarily in the entrance and exit regions. Because particles migrate across a clean sheath flow, diffusion to the walls of the classification region is minimal except at the lowest classification voltages of the DMA.

In contrast, the porous walls of the OMAC act as a particle sink along the entire classification channel. The transmission efficiency can be defined as the ratio of the integral over the diffusive transfer function to that over the nondiffusive one, i.e.,

$$\eta_{\text{trans}} = \frac{\int_{-\infty}^{\infty} \Omega\left[Z|Z^*\right] dZ}{\int_{-\infty}^{\infty} \Omega_{\text{ND}}\left[Z|Z^*\right] dZ}. \tag{2.9}$$

The transmission efficiency is $O(1)$ for $\sigma^2 < (8 \ln 2)^{-1}$, but drops precipitously above this value.

The minimal model on which Eq. (2.6) was based neglected the effects of viscous dissipation at the porous electrode surfaces. However, it was shown by Brownian dynamics simulation that the performance, as measured by the resolving power and efficiency, does not change appreciably from the plug flow model when the full velocity profile is considered [29]. The favorable theoretical results for the OMAC and a desire for experimental validation of its performance motivated the design and fabrication of a prototype.

2.4 Experimental

The core of the prototype OMAC is composed of two porous sintered stainless steel frits (Mott Corporation, Farmington, CT) and a dielectric spacer (acrylic) between them. Together, these components define the classification region, where $b = 1.7$ mm, $W = 11.7$ mm, and $L = 37.1$ mm. In Fig. 2.3, a cross section of the device shows that the frits extend beyond the classification region. Conductive tape (copper) was affixed to the bottom of the dielectric spacer to eliminate inlet/outlet losses that would occur if there were an electric field present in this area where there is no crossflow to oppose it.

The frits and spacer are housed in a custom-made enclosure composed of a dielectric top (acrylic), that has a port for the crossflow and a miniature high voltage port that makes contact with the upper frit via a spring, and an aluminum bottom that grounds the other frit. The aluminum piece also has ports for the aerosol, sample,

and the crossflow. Swagelok® tube fittings are used to interface the device with the balance of the fluid network, and O-rings are used to make seals. There is a notable exception, however, between the frits and the dielectric spacer, where no O-rings were placed. Hence, the rough frit surface sat directly against the spacer, almost certainly making for imperfect seals. The side of the frits that faces away from the spacer was partially covered with Parafilm®, so as to improve the quality of the O-ring seals made between the frits and the enclosure.

2.5 Results and Discussion

The starting point for validation of the prototype OMAC performance was the classification of a 92 nm PSL size standard, shown in Fig. 2.4. Later, we pushed the limits of the device and successfully classified the 1.47 nm size standard tetraheptylammonium bromide at a resolution of 5, as shown in Fig. 2.5 (the peaks that follow are the dimer, trimer, etc. of this gas ion).

The observed voltage setpoint at which the maximum detector signal was observed with the prototype OMAC was consistently less than expected, even with substantially different operating conditions. This deviation from theoretical performance is likely explained by the porous media extending beyond the classification region and poor seals between the porous media and the dielectric spacer. Both of these nonidealities tend to decrease the average crossflow velocity in the classification region.

The extent to which internal leaks were problematic was found to be a function of the assembly procedure, which was difficult to control with sufficient reproducibility so that two identical instruments could be fabricated. Although tandem operation with identical instruments is an ideal method for characterization of an instrument [31, 21, 22, 30], the trial and error process of assembling two devices with substantially similar internal leaks was judged to be too cumbersome a task for the present design. Nonetheless, the performance of the prototype OMAC was successfully demonstrated with the classification of 1.47 nm and 92 nm mobility standards.

2.6 Conclusions

The development and validation of this prototype OMAC may be viewed as a starting point for the experimental development of this class of differential electrical mobility classifier. Our data to date provides some insights into which of the possible paths forward may prove to be most fruitful. Beyond the obvious improvements of providing for adequate internal seals and reducing the losses in the inlet/outlet, it may prove to be the case that all of these problems are more easily resolved with a radial geometry. The experience gained in the design, fabrication, and validation of the prototype planar OMAC have aided in planning for future incarnations of the instrument.

2.7 Figures

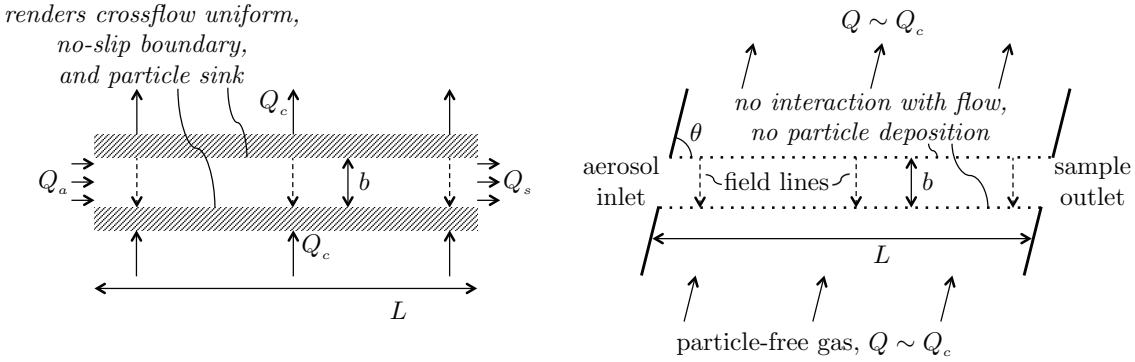

Figure 2.1. The different role of the electrodes in the OMAC and the IGMA as shown by two idealized plug flow, planar conceptual diagrams. The conductive porous media of the OMAC renders the crossflow Q_c uniform and may be approximated as a perfect particle sink that provides a no-slip boundary condition for the aerosol/sample flow. With the IMGA, the grid (or screen) electrodes are not intended to act as a sink of particles nor affect the fluid flow. With real instruments, this design difference affects the true detailed velocity profile, the maximum obtainable flow rates (as the relevant Reynolds numbers are different), the accessible values of the nondiffusive resolving power $\mathcal{R}_{\text{nd}}$, the efficiency of particle transmission, and the complexity of extending the planar concept to other geometries (i.e., radial and cylindrical).

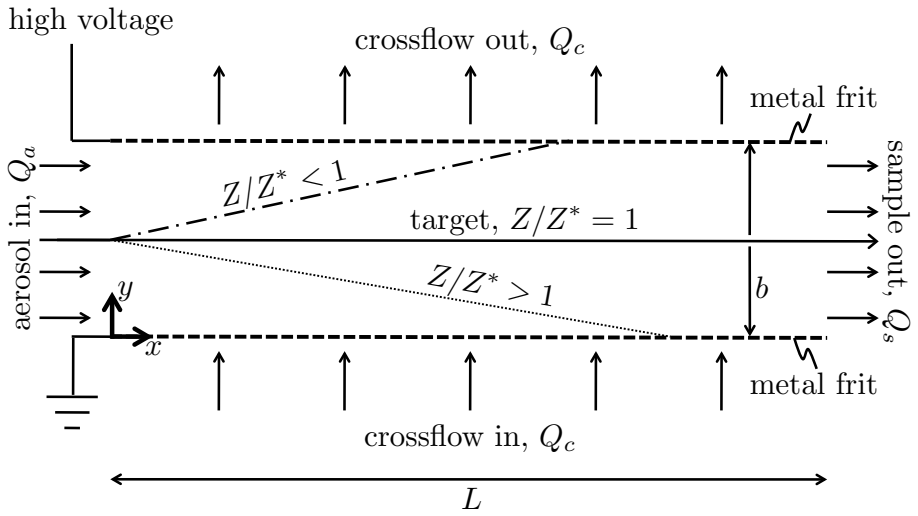

Figure 2.2. A planar OMAC with three particle streamlines originating at the center of the aerosol inlet to illustrate its behavior. Aerosol is introduced to the channel at a flow rate Q_a and sample is continuously collected at the other end at a rate of $Q_s = Q_a$. The OMAC has a crossflow Q_c that counteracts displacement owing to an electric field that is applied in the y-direction. Target particles proceed directly from the aerosol inlet to the sample outlet, with high and low mobility contaminants rejected through the sides. While three representative particle streamlines that originated at the center of the aerosol inlet are shown, it should be noted that particles are introduced uniformly over the entire cross section of the inlet.

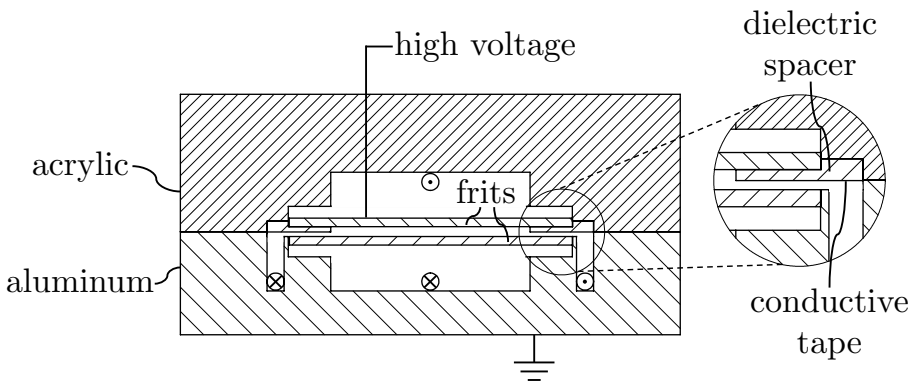

Figure 2.3. cross section of the prototype OMAC. Fluid entrances are marked as $\otimes$ and exits are labeled with $\odot$. The sample exit (which is symmetric with the aerosol entrance) is emphasized to illustrate where the frits extend beyond the classification region. Here, conductive tape is affixed to the spacer, which is in electrical contact with the lower frit, to ensure that the channel is isopotential exterior to the classification region.

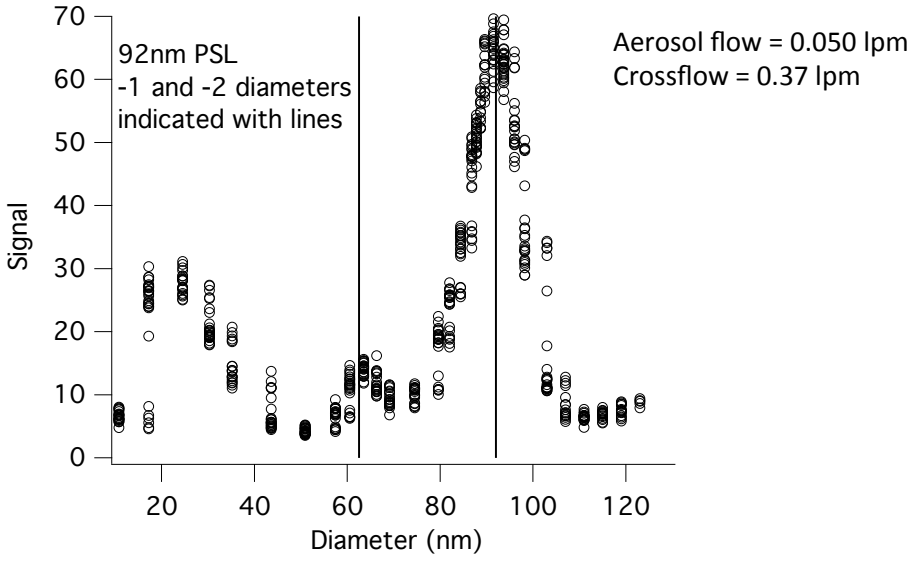

Figure 2.4. Validation of the planar OMAC with a 92 nm size standard.

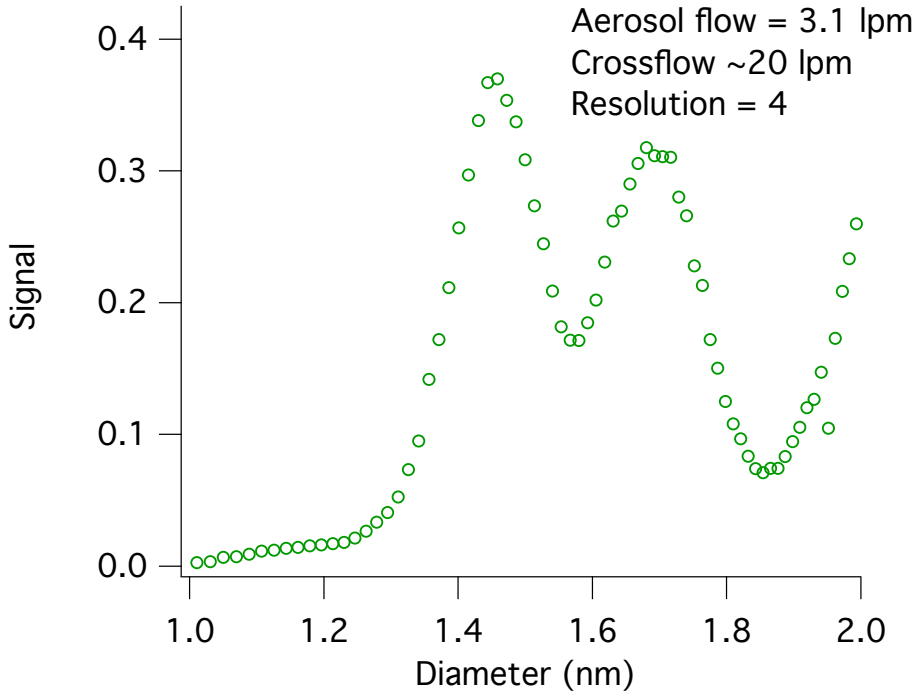

Figure 2.5. Validation of the planar OMAC with a 1.47 nm size standard.

Chapter 3

Evidence of Ion-Stabilized Nucleation Internal to Condensation Particle Counters with Sub-2 nm Size Cutoffs

3.1 Abstract

We observed a correlation between discrete ion pair production events and condensation particle counter noise at the CLOUD experiment at CERN. We hypothesize that the ion pairs generated internal to the supersaturated region activate and rapidly grow to a detectable size in detectors that push the limits of detection to below 3 nm. The CERN proton synchrotron is an unusually strong source of ion pairs; however, the present findings are relevant to balloon-borne and airplane studies, as the rate of ion pair production from galactic cosmic rays increases by an order of magnitude or more between the surface and the lower stratosphere.

3.2 Introduction

Nucleation of trace vapors produces nearly half of the global cloud condensation nuclei (CCN), yet the mechanisms of their formation and growth remain poorly understood. Atmospheric nucleation rates have been estimated from measurements at particle sizes that are far larger that the initial nuclei. Condensation particle counters (CPCs) determine the number concentration of particles larger than the so-called Kelvin equivalent size, i.e., the particle size that activates when exposed to a supersaturated vapor, often n-butanol. The minimum detectable particle size is determined

by three factors: (i) diffusion losses of small particles within the CPC; (ii) the supersaturation at which homogeneous nucleation will form new particles; and (iii) the chemical affinity of the vapor for the particulate material. The latter issue may lead to a composition dependent threshold, though n-butanol activation is relatively insensitive to composition. Diffusion losses were minimized by Stolzenburg and McMurry (1991) [32] in their ultrafine CPC (UCPC) on which commercial UCPCs have been based. Using n-butanol as a working fluid, UCPCs achieve a lower detection limit of about 2.5 nm in diameter D_p.

To understand the role of atmospheric nucleation on CCN concentration, CPC measurements must be augmented to enable measurements of growth rates. Limited size information can be obtained by making measurements at different supersaturations, thereby determining particle concentrations above different Kelvin equivalent sizes. Higher resolution size distribution measurements are made using the differential mobility analyzer (DMA) with a UCPC detector. Until recently, this measurement was also limited to $D_p > 2.5$ nm.

New DMAs can classify particles as small as 1 nm in diameter. The residence time in recently developed instruments has been reduced significantly to minimize diffusional degradation of DMA resolving power for such nano-condensation nuclei (nano-CN; [33]). This has been accomplished by using classifiers with aspect ratios that are smaller than those of the classic long-column DMAs [8], even smaller $O(1)$ aspect ratio devices that are meticulously machined so as to accommodate extremely large $O(10^3$ lpm) flow rates (HRDMA; [10, 11, 12]) and radial geometry instruments whose inward-accelerating flow further reduces the time spent in the classification region [7, 13]. Additionally, relatively large flow rate devices such as the air ion spectrometer (AIS; [34]) and the symmetric inclined grid mobility analyzer (SIGMA; [18]) have been developed with integrated electrometric detectors and have been demonstrated to be useful for classification and detection in the sub-2 nm regime. In a comparison of several of the $O(1$ lpm) classifiers with $O(5)$ resolving power, which are of moderate flow and resolving power relative to other instruments, the $O(1)$ aspect ratio nano-radial differential mobility analyzer (nano-RDMA; [13]) was shown

to compete favorably with other instruments with regard to both resolving power and transport efficiency [35]. Though there are higher flow rate alternatives with superior resolution, the nano-RDMA has the advantages of a broader dynamic range of mobilities and a smaller sample flow, which are ideal for chamber experiments.

Once classified, the charged nano-CN may be counted using an electrometer or a CPC. For sub-2 nm detection after a classifier, state of the art electrometers are only suitable for devices such as the HRDMA, AIS, and SIGMA, that are designed for large sample flow rates. A typical sensitivity of an electrometer is $O(10^{-16}$ A), and since the elementary charge is $e = 1.609 \times 10^{-19}$ C, $O(10^2 - 10^3)$, singly charged nano-CN must be captured by the Faraday cup each second to produce a measurable signal. Since diffusive transport losses to tubing walls are large and the probability of a particle being charged after a neutralizer is small for nano-CN, detector sensitivity is a key design parameter for sub-2 nm classification systems. Recently, the 2.5 nm cutoff of the widely used UCPC was extended to below 2 nm by adapting it for two-stage operation, with the first stage using a low-volatility, high surface tension working fluid and then a standard n-butanol 'booster' CPC for further growth and subsequent optical counting via light scattering. An extensive theoretical evaluation of more than 800 different candidate working fluids resulted in the selection of diethylene glycol (DEG) as suitable for use in the first stage of what will be referred to here as the UMN-CPC [36]. Although the UMN-CPC has single particle sensitivity, the incoming sample flow is divided into two or three streams: (i) an optional 1.2 lpm transport flow that reduces upstream diffusional losses; (ii) a sheath flow of ~ 0.25 lpm that is filtered, and then heated and saturated with the vapor of the working fluid; and (iii) a smaller $0.03 - 0.05$ lpm capillary flow whose nano-CN are grown and then counted. Hence, by design only $2 - 17\%$ of the aerosol that enters the CPC are counted with such an instrument design. The percentage may be lower due to diffusional losses internal to the detector and incomplete activation and growth of the incoming particles to a detectable size. At the low concentrations that typically result from sub-2 nm classification, the resulting low particle count rate leads to large measurement uncertainties or long counting times and slow measurements.

Ultrafine particle activation can be achieved with higher flow rates by turbulent mixing of a warm, vapor-laden flow with a cold aerosol flow in a device that has been variously called a mixing-type CPC or a particle size magnifier (PSM) [37, 38]. Following the lead of Iida et al. (2009), Vanhanen et al. (2011) developed a two-stage CPC that employs a high aerosol flow rate PSM first-stage that uses DEG as a working fluid and a n-butanol booster CPC [39]. While its response time, much like the UMN-CPC, is relatively long and dominated by the $O(1\text{ s})$ second-stage n-butanol booster, the PSM does have the design advantage of not immediately discarding the majority of the classified aerosol.

For the Fall 2010 Cosmics Leaving OUtdoor Droplets (CLOUD) campaign at CERN, an UMN-CPC consisting of a laminar UCPC modified to use DEG and a n-butanol second-stage booster was deployed by Frankfurt University and a PSM was deployed by the University of Helsinki. The details of the CLOUD chamber and an overview of the results from the Fall 2010 campaign are presented elsewhere [40]. The UMN-CPC and the PSM were used for much of the campaign to track the increase in the chamber particle concentration during steady-state nucleation events. Additionally, there were efforts to integrate each of these instruments with a nano-RDMA deployed by Caltech for studying the evolution of the $1 - 10$ nm size distribution in the chamber as particles nucleated and grew. The subject of the present manuscript is to present and discuss the results and lessons learned from these efforts, and to chart a path forward for improving such measurements for chamber studies, surface-level field deployments over land and the ocean, and high altitude studies.

Before proceeding, it will be of some utility to discuss the pion beam spills from the CERN Proton Synchrotron (PS) that are used as a source of ionizing radiation at the CLOUD chamber. A pion is a subatomic particle which, when it and its daughter particles decay, may result in the generation of ion pairs. The conditions in the free troposphere, where galactic cosmic rays and their daughter particles create considerably more ion pairs per unit volume per unit time than on the surface, may be simulated at the CLOUD chamber by introducing discrete bursts, or spills, of

subatomic particles from the PS, where the paths of these particles are deflected from the accelerator to being incident on the chamber using a magnetic field. The typical operating conditions are to introduce $2-3$ regularly spaced spills to the chamber per $\sim$ 45 s PS supercycle, so the characteristic timescale between spills is $\sim$ 15 s. Since the chamber is well-mixed by two fans, the ion concentration rapidly becomes homogeneous despite the discrete nature of the ion-pair source pion beam and the fact that it is focused on a relatively small ~ 1 m^2 portion of a ~ 3 m in diameter and height cylindrical chamber. The intensity of the pion beam, which is proportional to the number of ion-pairs that are generated in the chamber, is measured by a plastic scintillator hodoscope. The pion spills from the PS, which are essential for simulating the higher altitude conditions and motivated the siting of the CLOUD project at CERN, led to unexpected instrumentation challenges for the measurement of the $1-10$ nm size distribution.

3.3 Observations at CLOUD

When the nano-RDMA was integrated with the UMN-CPC, it was found that there were periodic count spikes in the CPC of duration ~ 3 s with periodicity of ~ 15 s. As shown in Fig. 3.1, these spikes correlated with the PS beam pion spills, as measured by a hodoscope. A Fourier analysis revealed that the frequencies of the two signals were nearly the same. It was found that this spill and CPC count spike correlation, which is problematic from the perspective of there being a nonzero, unsteady baseline to the CPC concentration, could be eliminated by decreasing the temperature difference between the saturator and condenser in the first, or DEG, stage of the UMN-CPC. Furthermore, a reduction of the saturator flow rate with the PSM also eliminated this correlation in that instrument. These changes had the effect of increasing the minimum detectable diameter of the instruments, so sub-2 nm nano-CN could no longer be activated and grown to a detectable size. Finally, this correlation was not observed in any of the other CPCs used during the Fall 2010 CLOUD campaign at CERN, all of which had size cutoffs of 2.5 nm or greater.

3.4 Discussion

A likely explanation for the observed correlation between CPC count spikes and PS beam pion spills is ion-stabilized nucleation internal to the detector. A conceptual diagram illustrating how detectable nano-CN may be nucleated internal to a CPC is shown in Fig. 3.2. Further evidence of nucleation internal to the detectors is that the relative intensity of these spikes was greater with the PSM than the UMN-CPC. This is to be expected as the PSM has a larger system volume at and after the first stage condenser, meaning more ion pairs are generated internal to the device. Since the PSM was also commonly operated at a lower size cutoff, a larger fraction of the nano-CN formed internal to the detector activated and grew to a detectable size. Additionally, the observation that decreasing the saturator/condenser temperature difference with the UMN-CPC or, equivalently, reducing the saturator flow rate with the PSM, resulted in the elimination of these spikes supports that they are a consequence of ion-induced nucleation internal to the detector. These changes to the CPCs acted to increase the minimum detectable nano-CN size that could be activated and grown to a detectable droplet, so, similarly to the other larger size cutoff CPCs deployed for the Fall 2010 CLOUD campaign, the ion pairs generated internal to the detector were not detectable under these conditions. Finally, the possibility that the CPC spikes reflected the detection of transient detectable nano-CN generation internal to the chamber was ruled out by connecting filters to the inlets of the CPCs with the pion beam on and noting that the spikes were still observed.

The consequences of nucleation internal to the detectors are generally negligible from the perspective of counting the entire chamber concentration. This is significant as the derivative of the total concentration as a function of time is the nucleation rate, a key measure for CLOUD studies. The pion spills nucleate $\sim 10^2 - 10^3$ detectable nano-CN in the UMN-CPC and $\sim 10^3 - 10^4$ in the PSM over a duration of ~ 3 s. The chamber aerosol signal during nucleation events typically exceeds this noise by several orders of magnitude. Frequently, the nucleation internal to the detector did not even amount to a significant digit of the total count rate during even modest

nucleation runs at CLOUD.

With classification, however, the CPC count spikes from the pion beam spills may have a hugely deleterious effect, particularly in the $1-10$ nm size range where transport losses are the largest (and, hence, signal strength is the faintest). Additionally, if neutral nano-CN are to be classified, the small probability of a $1-10$ nm nano-CN acquiring a charge in a neutralizer further reduces the signal and complicates the measurement. As shown in Fig. 3.3, using detectors such as the UMN-CPC, which by design discard $3-17\%$ of the incoming signal in the laminar first stage, is nonoptimal when the objective is to classify an unknown size distribution at even a relatively small resolving power, as the signal can easily be on the same order of magnitude or even smaller than that of the CPC count spikes.

3.5 Conclusions

Sub-2 nm classification in environments with large ion production rates, such as the CLOUD chamber and at high altitude, must be done thoughtfully so as to manage or altogether eliminate the generation and detection of nano-CN internal to the instrument. For the CLOUD experiment, the high flow rate devices that use electrometric detection may be used to an extent so long as the perturbation to the system from the instrument sampling flow is small on the characteristic timescale for the physics of interest. For example, an AIS was deployed for the Fall 2010 CLOUD campaign. From the perspective of making use of lower flow rate, larger resolving power instruments such as the nano-RDMA, however, the CPC count spikes problem identified here must be addressed. One option is to use several instruments, each fixed at a target diameter or interest. A particularly suitable application for such a configuration is the study of short nucleation bursts followed by rapid growth [41]. The ~ 3 s intervals where the CPC spikes are problematic may simply be discarded. However, in many cases the combined flow rate and the number of size channels monitored may approach that of a single instrument such as the AIS, which also makes continuous measurements and even has the advantage of not having any interruptions in data

collection owing to the electrometric detectors employed. Another alternative for the CLOUD chamber is to use sufficiently fast response detectors so that an entire scan from $1 - 10$ nm is completed in the ~ 10 s between the pion beam spills. This could be achieved with two fast mixing CPCs in series. Such a configuration, if properly designed, would have the additional advantage of counting every particle that is classified, dramatically improving the counting statistics and making the inversion from the raw data to a size distribution a more tractable endeavor. Finally, there is evidence that an optimally configured single stage, fast response detector is capable of activating nano-CN; this possibly simpler option should be considered as well [42].

For ground and sea-level studies, laboratory validation of the instrumentation would generally be sufficient for ensuring that ion-pair production internal to the detector owing to galactic cosmic ray (GCR) decay is not problematic. For airplane or balloon-borne studies, however, the GCR intensity increases with altitude. Hence, CPC detector performance should be reevaluated at altitude and, in many cases, the minimum detectible diameter would have to be increased in order to decrease the noise to the one count per five minutes standard in the literature [36]. An important lesson learned from the Fall 2010 CLOUD campaign is that such an increase to the minimum detectable diameter would likely mean sacrificing the capability for sub-2 nm classification at high altitudes. Beyond resorting to electrometric methods, it may prove to be the case that for some applications a favorable signal to detector noise ratio may be obtained through further optimization of the classifier and detector. For the classifier, this means removing any dielectric from the aerosol flow path, a culprit for much of the losses of nano-CN owing to the unfavorable field and the accumulation of parasitic surface charge that may then act to deflect the nano-CN to deposit on a wall. Typically, dielectrics are used to transition from ground to high voltage at the classifier inlet or outlet; they may be eliminated by introducing the aerosol and capturing the sample through ports that are both grounded [43] or running one of the lines at potential. Note that care should be taken to ensure that there is no risk of ignition or detonation from arcing in the presence of a flammable working fluid such as n-butanol. The operation of the detector with some internal

GCR-induced nucleation should be such that every nano-CN that enters the device is counted and, hence, the signal is maximized. This means using properly designed fast-mixing CPCs, which also have the added benefit of a short response time.

3.6 Figures

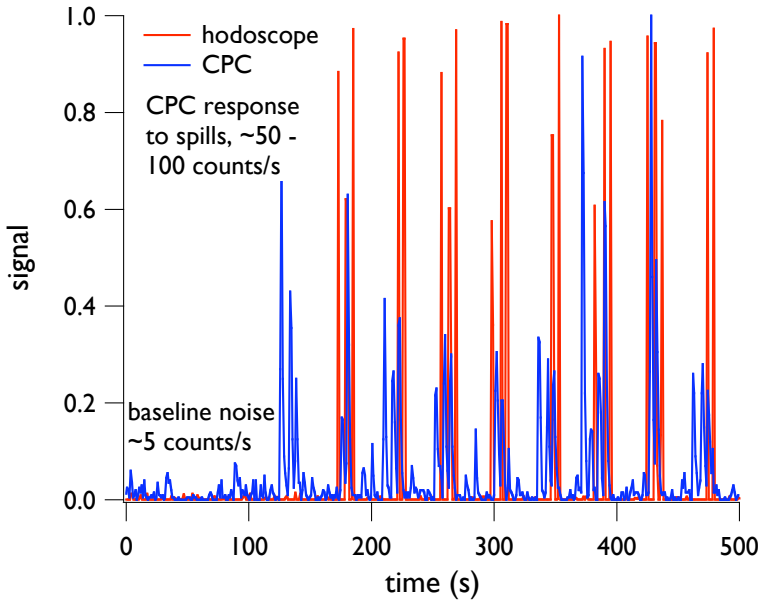

Figure 3.1. The correlation between the CERN PS beam pion spills and CPC count spikes for both the UMN-CPC. Similar behavior was observed with the PSM.

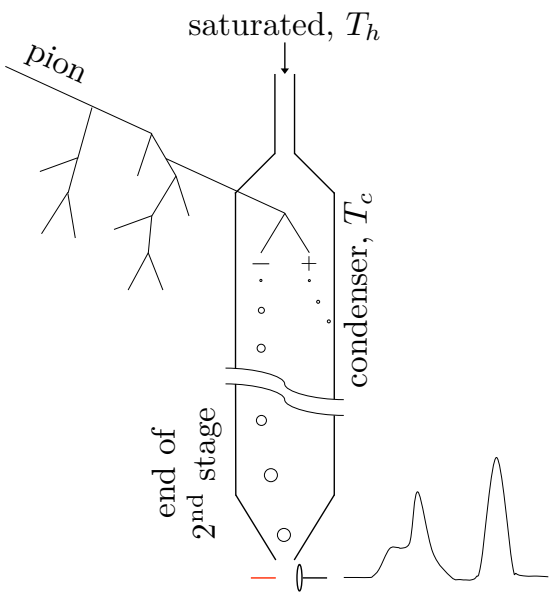

Figure 3.2. A possible pathway for nucleation and growth of detectable nano-CN internal to a CPC. An ion pair formed in the first stage condenser (or, conceivably, downstream of it) may then become a charged nano-CN and subsequently grow rapidly in the supersaturated DEG and, later, n-butanol environments. Here, the negative ion grows to become a detectable particle, while the positive ion is lost via diffusive deposition to the wall. It is likely that ion pairs generated upstream of the first stage condenser share a fate similar to that of the positive ion shown here since, as gas ions or clusters, they have large diffusion coefficients and rapidly deposit onto tubing walls.

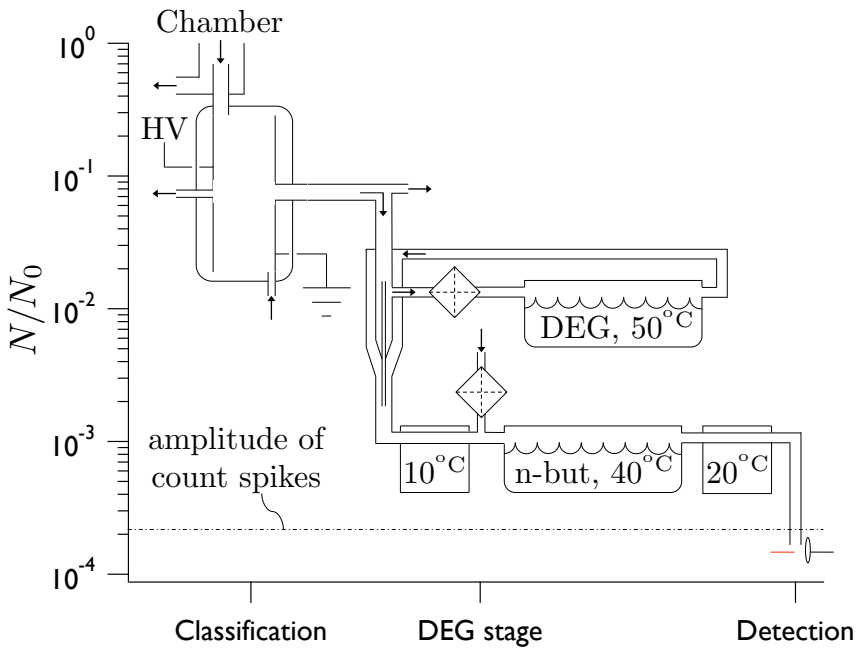

Figure 3.3. A representative characteristic magnitude of the unknown size distribution signal N relative to that which would be observed with lossless transport, classification, and detection, N_0, is shown as the nano-RDMA/UMN-CPC system integrated into CLOUD is traversed. While care should be taken to minimize transport losses from the chamber to the instrument, note that the vast majority of the losses in the system occur as the nano-CN from the first (DEG) stage laminar CPC transport and sheath flows are discarded.

Chapter 4

A Working Fluid Selection Process for Isothermal Condensation Particle Counters

4.1 Abstract

Using a substantially simplified selection process, we identified 4-methylnonane, methyltoluene, and propylcyclohexane, as promising working fluids for condensation particle counters (CPC) operation at 180 K at the Cosmics Leaving OUtdoor Droplets experiment at CERN. Transport modeling of isothermal ultrafine CPCs (UCPCs) reveals that, sensibly, their performance is governed by the Graetz number and the radial extent of the capillary relative to that of the tube through which the sheath gas is introduced. While the optimal design and operating conditions of an isothermal UCPC are identified, the broadest impact of instrumentation development efforts would be the fabrication of mixing-type CPCs designed to prevent nascent particle evaporation, which would be ideal for use with a differential electrical mobility classifier to interrogate the size distribution because of their rapid time response. Significantly, the working fluid selection process we develop here is applicable to all CPCs, as we decouple complex transport modeling from the identification of promising candidate fluids.

4.2 Introduction

The Cosmics Leaving OUtdoor Droplets (CLOUD) experiment at CERN is now capable of operating at 180 K, enabling simulations of the coldest regions of the polar stratosphere. While condensation particle counters (CPCs) have long been used for measuring particle concentrations of such systems, their present designs require that the sampled aerosol be introduced into a warm ($\sim$ 310 K) gas stream that is saturated with the working fluid vapor. For room temperature experiments, heating the aerosol by $10 - 30$ K leads to some evaporation and, thereby affects the apparent activation efficiency of the nascent particles in the CLOUD chamber, though the effect may be small enough to ignore. For operation at 180 K, however, the resultant temperature difference of more than 100 K represents a dramatic departure from the chamber conditions. This would likely result in significant challenges with the detection of freshly nucleated particles. There are many other endeavors that require measurements in environments with temperatures that are substantially different from room temperature, notable amongst which are airplane and balloon-borne campaigns, and ambient surface-level studies in cold environments such as the heavily studied boreal forest in Hyytiälä, Finland, and the long-running observatory at Jungfraujoch in Switzerland. Hence, there is a need for new approaches to detect particles, particularly small ones composed of volatile species that must be measured under extreme operating conditions.

Much can be learned from present CPC designs, such as those illustrated in Fig. 4.1, and from the methodologies that have been used to select working fluids. Perhaps the most widely used device is that of Agarwal and Sem (1980) in which the aerosol flows through a heated n-butanol saturator [44]. The particle/vapor mixture then flows through a thermoelectrically cooled condenser to produce the supersaturation that leads to particle activation and growth; this method has been used to detect particles as small as 10 nm in diameter. Stolzenburg and McMurry (1991) redesigned that instrument to reduce diffusional losses and enable better control of the supersaturation; their ultrafine CPC (UCPC) is capable of detecting particles as small as

2.5 nm in diameter [21, 32].

An entirely different approach is to turbulently mix the aerosol with a hot stream saturated with n-butanol. Variously called the mixing-type CPC or particle size magnifier (PSM) [37, 38, 39], this instrument enables efficient activation of particles with a much larger aerosol flow than that used with the UCPC . A particularly clever instrument is the water CPC. This instrument takes advantage of the fact that the diffusion coefficient of the working fluid (water) is larger than the thermal diffusivity of the gas. By heating a wet-walled tube along its length, supersaturation is produced in the neighborhood of the centerline of a heated, wet-walled tube. Expansion-type CPCs, where an adiabatic expansion supersaturates the vapor, have also been used to detect sub-10 nm particles [45]. Through all of these developments, CPC measurements have been confined to particles larger than ~ 2.5 nm in diameter.

The 2.5 nm barrier was recently surpassed by Iida et al. (2009), who separated activation from growth in a two-stage CPC. This was accomplished by using a low volatility, high surface tension working fluid to activate sub-2 nm particles without inducing homogeneous nucleation of the vapor. The activated nanoparticles were then grown and detected using a conventional n-butanol 'booster' CPC, as illustrated in Fig. 4.1. A UCPC was used as the first stage to minimize nanoparticle diffusional losses. The working fluid was identified from a set of over 800 candidate organic compounds. Particle activation and growth simulations identified conditions that would enable detection of particles as small as 1 nm in diameter. Predictions of the rate of new particle formation using the classical theory of homogeneous nucleation enabled identification of a small subset of working fluids that could activate the small particles with minimal risk of nucleation-induced artifacts. Ultimately, diethylene glycol (DEG) was selected as the most promising working fluid for the first stage. Its suitability was confirmed experimentally using a DEG UCPC first-stage and a n-butanol second stage to detect gas ions as small as 1.2 nm in diameter. This impressive achievement was quickly followed with a PSM version of the instrument [39], in which the first stage activated the particles using DEG in a PSM, while the second booster stage was a conventional n-butanol CPC. More recently, it was shown

that a single stage n-butanol UCPC can both activate sub-2 nm particles, and grow them to an optically detectible size [42], albeit under aggressive, high supersaturation conditions that were attained by operating the saturator at temperatures as high as 340 K.

Thus, using either a two-stage CPC or a high vapor pressure, high supersaturation single-stage instrument, particle detection to ~ 1 nm is now possible. However, CPC designers implicitly assume that the particles to be detected are sufficiently refractory that they will not evaporate significantly at the most extreme conditions encountered in the instrument. While this assumption is often reasonable, the conditions encountered for low temperature measurements at CLOUD, in upper atmosphere measurements, or in measurements of freshly nucleated particles near the critical size, require measurements of marginally stable particles for which evaporation is likely. To develop measurement approaches suitable for such conditions, we therefore seek to identify CPC working fluids and operating conditions that will minimize the risk of shrinkage of particles below the detection threshold by evaporation. Iida et al. (2009) provided a strategy for solving this CPC design problem, which we generalize in this paper. Here, the operating temperature is taken as a key design parameter. We search a library of candidate compounds for ones that will activate particles of interest near that operating temperature, and that will do so with minimal risk of nucleating new particles, subject to additional safety, cost, and feasibility constraints.

4.3 Evaluation of candidate working fluids for 180 K

The central objective here is to eliminate all unnecessary complexity from the working fluid selection and CPC design processes in order to distill the problem down to the essential physics. Using the model of Stolzenburg (1988) as inspiration, a more simply applied minimal model is sought. A measure of the extent to which this endeavor is successful will be how broadly the process that is set forth is used for applications

analogous to the 180 K operating condition considered here.

To begin, candidate working fluids are identified independent of transport considerations. A perfectly mixed, isothermal control volume will be considered, a significant departure from the treatment of Stolzenburg (1988). Such a treatment may nonetheless prove to be of some utility for the 180 K application considered here, as it would be ideal to prevent evaporation of incoming aerosol by maintaining the entire flow path at a constant temperature. Arguably the most challenging aspect of the analysis of Iida et al. (2009) is accurately solving the convective-diffusion equation homogeneous nucleation rate model. While this can be done with some ease with a finite element routine, such as those implemented by COMSOL, such programs can be prohibitively expensive, and suffer numerical instabilities when solving stiff rate equations.

The relevant physical data on 4899 candidate working fluids from [46] was used to screen for candidate working fluids, according to the algorithm that is sketched in Fig. 4.2. The suitability of a working fluid for use at 180K was first examined using estimates of the homogeneous nucleation rate, minimum activated diameter, and growth rate. The material safety data sheets of those candidates that remain were then used to evaluate possible hazards to their use. The application of this algorithm to the 180 K CLOUD operating condition illustrates a general methodology that could be applied across the entire temperature range.

The specific selection criteria may differ slightly depending on the application. For the present purposes, we consider a fixed control volume of 1 mL, a reasonable order of magnitude estimate for the supersaturated volume of a UCPC (the volume of the Stolzenburg and McMurry (1991) UCPC is 1.46 mL [21, 32]). Classical homogeneous nucleation theory is used to calculate the rate of formation of new particles per unit volume J as

$$J = \left(\frac{2\sigma}{\pi m_1}\right)^{1/2} \frac{v_1 N_1^2}{S} \exp\left[-\frac{16\pi}{3}\frac{\sigma^3 v_1^2}{(kT)^3 (\ln S)^2}\right], \tag{4.1}$$

where σ is the surface tension, m_1 is the mass of a molecule of the working fluid, v_1 is the volume per molecule in the liquid phase, N_1 is the number concentration of

working fluid monomers in the gas phase, S is the saturation ratio, k is the Boltzmann constant, and T is the temperature [47]. The saturator temperature is adjusted until the calculated rate of homogeneous nucleation is 1 min^{-1} in the control volume, following the guidelines set out by Iida et al (2009). This calculation provides an estimate of the maximum usable saturation ratio for each respective compound. This limiting saturation ratio, S_{lim} determines the diameter of the smallest particle that can be activated according to the Kelvin equation [47]

$$D_p = \frac{4\sigma v_1}{kT \ln S_{\text{lim}}}. \tag{4.2}$$

Since our focus is on particles much smaller than the mean free path, we use the kinetic theory growth rate expression,

$$\frac{dD_p}{dt} = \frac{v_1 \bar{c}_1 \alpha}{2} \left(N_1 - N_{1,s}\right), \tag{4.3}$$

where the mean speed of the molecules is

$$\bar{c}_1 = \left(\frac{8kT}{\pi m_1}\right)^{1/2}. \tag{4.4}$$

The surface monomer number density $N_{1,s}$ is set to zero and the accommodation coefficient α is set to unity for the purpose of making a rough estimation [47]. The growth rate must be sufficient to grow particles to a size that can be activated by a conventional CPC, > 10 nm, within the $\sim 10^{-2}$ s residence time of the activation stage, so we require $dD_p/dt > 10^3$ nm s^{-1}. Growth to supermicron sizes within this time may enable operation as a single-stage CPC, as demonstrated by Kuang et al. (2012) for n-butanol at room temperature. The final stipulation, motivated by the present focus of CLOUD on nucleation studies, is that the working fluid must be theoretically capable of activating particles with a Kelvin $D_p < 2$ nm. Many candidate working fluids were identified in this initial screen; Fig. 4.3 shows the minimum operating temperature of these working fluids and the temperature range over which they satisfy the restrictions set forth up to now.

Ideally, a working fluid will enable operation over a reasonably broad temperature range, perhaps 25 K, to enable flexibility in use in the CLOUD experiments or in airborne operation. Thus, the set of candidate working fluids can be further limited by considering only those that have a maximum operating temperature of 205 K or greater. The physical/chemical data and operating parameters at $T_{\text{op}} = 180$ K of the 24 working fluids identified using the present algorithm are shown in Table 4.1, with the safest 3 candidates from the perspective of health and reactivity emphasized with bold font. While factors such as cost and flammability are not explicitly considered here in the determination of suitable candidate working fluids, it merits mentioning that factors such as these may be primary drivers of analogous analyses for different applications. For example, for a broad deployment of instruments on airplanes, there may be cost limitations and regulations that restrict the usage of flammable working fluids.

4.4 Transport considerations in laminar-flow CPC designs

4.4.1 Plug flow analysis

Having identified a number of candidate working fluids based only on thermodynamic and kinetic factors, we now examine the role of transport processes in working fluid selection. Since our focus is on the development of a simple model for the detection of freshly nucleated particles, we consider the minimal model of the UCPC of Stolzenburg and McMurry (1991). This highly idealized model assumes that the aerosol enters the activation region through a small capillary of radius ϵ, that is inside a concentric larger tube of radius R. The outer tube carries the working fluid vapor that was initially saturated at a higher temperature than T_{op}. For present purposes, it is assumed that the vapor laden flow has been cooled to the sample temperature T_{op}, to produce the initial saturation ratio S_0 at the entrance to the activation and growth region. Thus, this minimal model represents an ideal, isothermal UCPC.

Figure illustrates this ideal model.

Activation within the UCPC occurs when $S > S_{\text{crit}}[D_p]$, as described by the Kelvin equation. The particle number concentration is assumed to be sufficiently low that neither the vapor concentration nor the temperature is altered by the activation and growth process. Thus, the aerosol and supersaturation profiles can be assumed to evolve independently. Because particle diffusion coefficients are much lower than those of the vapor, particle diffusion is neglected. The minimal model thus reduces to solving the convective-diffusion equation for the vapor concentration, $C[r,z]$, i.e.,

$$u[r]\frac{\partial C}{\partial z} = D\left(\frac{1}{r}\frac{\partial}{\partial r}\left[r\frac{\partial C}{\partial r}\right] + \frac{\partial^2 C}{\partial z^2}\right), \tag{4.5}$$

and calculating particle growth for those that surpass the Kelvin threshold, where $u[r]$ is the axial velocity profile for the gas and D is the vapor diffusion coefficient.

Initially, we assume plug flow $u[r] = U$, the mean velocity of the flow. The boundary condition at the entrance is $C[r,0] = C_{\text{ss}}(\text{H}[r-\epsilon] - \text{H}[r-R])$, where H is the Heaviside step function. Conceivably, a physical system that would provide for such a uniform initial condition would provide for the rapid cooling of the hot, saturated gas immediately upstream of the isothermal supersaturation region. A chilled particle-free gas stream could be turbulently mixed with the saturator exhaust, for example, so long as the turbulence is sufficiently damped out by the inlet considered here. The wall is assumed to have a thin layer of liquid that, while otherwise neglected, establishes a saturation boundary condition at the wall, $C[R,z] = C_{\text{sat}}\left[T_{\text{op}}\right]$. Symmetry at the centerline requires $\frac{\partial C}{\partial r}[0,z] = 0$.

The convective-diffusion equation can be made dimensionless by defining the scaled variables

$$\hat{C} = \frac{C - C_{\text{sat}}}{C_{\text{ss}} - C_{\text{sat}}},\ \hat{r} = \frac{r}{R},\ \text{and}\ \hat{z} = \frac{z}{L}. \tag{4.6}$$

Assuming that the tube aspect ratio is large, $(L/R)^2 \gg 1$, it becomes

$$\frac{\text{Gz}}{4}\frac{\partial \hat{C}}{\partial \hat{z}} = \frac{1}{\hat{r}}\frac{\partial}{\partial \hat{r}}\left[\hat{r}\frac{\partial \hat{C}}{\partial \hat{r}}\right], \tag{4.7}$$

with

$$\hat{C}\left[\hat{r},0\right]=\mathrm{H}\left[\hat{r}-\frac{\epsilon}{R}\right]-\mathrm{H}\left[\hat{r}-1\right],\ \hat{C}\left[1,\hat{z}\right]=0,\ \text{and}\ \frac{\partial C}{\partial r}\left[0,\hat{z}\right]=0, \tag{4.8}$$

where $\mathrm{Gz}=4UR^2/D/L$ is the Graetz number, a dimensionless group that describes the development of the concentration profile in laminar tube flow.

The scaling of the convective-diffusion equation and associated boundary conditions for a general plug flow UCPC has resulted in the identification of the Graetz number and the dimensionless capillary radius, ϵ/R, as the dimensionless groups that govern the performance of such an instrument. From the perspective of detector performance, it is ideal to maximize ϵ/R to achieve the highest possible sensitivity and signal to noise ratio, assuming that all incoming particles are activated and subsequently grown to a detectable size. The activation and growth of the aerosol in such an isothermal CPC would require that $\epsilon/R<1$, so that the supersaturated vapor is introduced at the inlet. Additionally, the value of Gz at which the instrument is operated must fall within the physically realizable range for the working fluid, detector geometry, and operating conditions. A useful expression for the Graetz number from the perspective of instrument design is

$$\mathrm{Gz}=\frac{4Q}{\pi^{2/3}D}\left(\frac{R}{L}\right)^{2/3}\left(\frac{1}{V}\right)^{1/3}, \tag{4.9}$$

where $Q=\pi R^2U$ is the total (sheath and aerosol) flow rate and $V=\pi R^2L$ is the isothermal supersaturated region volume. At 180 K, the present working fluids have $D\sim10^{-6}$ m^2/s. We choose design parameters that are consistent with present instruments, a flow rate of $0.03\ \mathrm{lpm}<Q<3\ \mathrm{lpm}$, an aspect ratio in the range $10<L/R<10^2$, and a supersaturated control volume of $V=1$ mL. Given these inputs, the accessible range in the Graetz number is approximately $4<\mathrm{Gz}<2000$.

It would now be useful to determine a quantitative criterion by which the performance of instruments with different ϵ/R and Gz may be compared. One such metric is the value of the centerline saturation ratio at the outlet of the control volume. Since $S_0\gg1$ for all of the candidate working fluids, the exit centerline saturation

ratio is

$$S\left[0,L\right] \equiv \frac{C\left[0,L\right]}{C_{\text{sat}}} = \hat{C}\left[0,1\right]\left(S_0 - 1\right) + 1 \approx \hat{C}\left[0,1\right] S_0, \tag{4.10}$$

so long as $\hat{C}\left[0,1\right] \gg S_0^{-1}$. Since the vapor must diffuse to reach the centerline, all of the entering particles with a diameter greater than that of the Kelvin diameter for $S = \hat{C}\left[0,1\right] S_0$ are activated. For $\hat{C}\left[0,1\right] = 0.8$ and $S_0 = 10^2$, the size cutoff predicted by the perfectly mixed, isothermal model will be consistent with that calculated with the present model to within

$$\frac{D_{p,\text{ Kelvin}}\left[0.8S_0\right]}{D_{p,\text{ Kelvin}}\left[S_0\right]} - 1 = \frac{\ln S_0}{\ln\left[0.8S_0\right]} - 1 = \frac{\ln 100}{\ln 80} - 1 = 0.0509\ldots \approx 5\%, \tag{4.11}$$

which validates the approximations of the model that wholly neglects transport for isothermal CPC working fluid selection. Another appealing reason for selecting a relatively large outlet centerline saturation ratio as the criterion for determining the optimal values of ϵ/R and Gz is that once particles are activated, many remain in a highly supersaturated region for the duration of their transit through the control volume. Insofar as vapor depletion (from activation and growth of particles) could be problematic, a design which provides for large saturation ratios in the neighborhood of the aerosol minimizes the decrease in efficiency that would follow.

The minimum tolerable outlet centerline saturation ratio is now set to $S\left[0,L\right] \approx \hat{C}\left[0,1\right] S_0 = 0.8S_0$, though it could be set to a different value depending on the application, and a solution to the convective-diffusion is sought in order to find the optimal values of ϵ/R and Gz for this plug flow isothermal CPC. The dimensionless working fluid vapor concentration is found via separation of variables to be

$$\hat{C} = \sum_{n=0}^{\infty} A_n \mathrm{J}_0\left[\lambda_n \hat{r}\right] \exp\left[-4\lambda_n^2 \hat{z}/\mathrm{Gz}\right], \tag{4.12}$$

with coefficients

$$A_n = \frac{2\left(\mathrm{J}_1\left[\lambda_n\right] - \frac{\epsilon}{R}\mathrm{J}_1\left[\frac{\epsilon}{R}\lambda_n\right]\right)}{\lambda_n\left(\mathrm{J}_1\left[\lambda_n\right]\right)^2}, \tag{4.13}$$

where J_i is the Bessel function of the first kind and λ_n is the n-th root of J_0. Figure

4.5 shows the contours of constant $\hat{C}[0,1] = S[0,L]/S_0$ as a function of ϵ/R and Gz.

The concentration profile for the aerosol can be obtained from the same convective-diffusion equation with appropriately modified boundary conditions and scaled Gz. For the optimal vapor operating conditions of $\epsilon/R = 0.21$ and Gz $= 58$, fewer than 0.5% of the aerosol would be lost to diffusion to to walls even if none of them were activated. Hence, diffusional losses of the aerosol are negligible in the supersaturated region.

It should be noted that while the saturation ratio is large in the neighborhood of the particles for the present design, it may prove to be the case that a booster stage is necessary to grow the particles to a detectable size [36]. This second stage device would have a much more forgiving design as the incoming particles will have already been activated and grown to some extent. Recent work [42] has shown, however, that an optimized single stage device is sufficient in at least one case.

4.4.2 Poiseuille flow analysis

The promising results from the plug flow model motivated a more detailed model, where the more physically relevant Poiseuille flow velocity profile $u[r] = 2U\left(1-(r/R)^2\right)$ is incorporated. The nondimensionalized convective-diffusion equation becomes

$$\frac{\mathrm{Gz}}{2}\left(1-\hat{r}^2\right)\frac{\partial \hat{c}}{\partial \hat{z}} = \frac{1}{\hat{r}}\frac{\partial}{\partial \hat{r}}\left[\hat{r}\frac{\partial \hat{C}}{\partial \hat{r}}\right], \tag{4.14}$$

with

$$\hat{C}[\hat{r},0] = \mathrm{H}\left[\hat{r}-\frac{\epsilon}{R}\right] - \mathrm{H}[\hat{r}-1],\ \hat{C}[1,\hat{z}] = 0,\ \text{and}\ \frac{\partial C}{\partial r}[0,\hat{z}] = 0, \tag{4.15}$$

where the same approximations made in the plug flow model are again applied. The solution was found using COMSOL, and the contours of constant $\hat{C}[0,1] = S[0,L]/S_0$ as a function of ϵ/R and Gz are shown in Fig. 4.6. Similarly to the plug flow model, even for the smallest of the sample aerosol the transport efficiency is large. Less than 1.5% of the aerosol is lost to the walls in the worst case scenario where none of the

freshly nucleated particles were activated, so the diffusional loss of aerosol is negligible in this supersaturated control volume.

With the optimal values of $\epsilon/R = 0.1$ and $\mathrm{Gz} = 35$ determined for Poiseuille flow, it is worthwhile to consider some typical values of the relevant dimensions and operating conditions of a isothermal UCPC to ensure that they seem reasonable. Consider a system with $V = 1$ mL and $R/L = 1/10$, so then $L = 3.17$ cm, $R = 0.317$ cm and $\epsilon = 0.0317$ cm, none of which stand out as problematic from the practical perspective of machining tolerances, providing care is taken in the fabrication and alignment. In order to obtain $\mathrm{Gz} = 35$, a total flow rate of $Q = 0.05$ lpm must flow through the control volume, a somewhat small flow rate for a detector that remains laminar in the present system as the Reynolds number $Re \approx 30$ for this flow rate and these dimensions at 180 K. Nonetheless, this is certainly a practical flow rate and size for personal monitoring or remote sampling in extreme environments, like Saturn's moon Titan.

4.5 Discussion

The present results illustrate the utility of a simplified working fluid selection process, done independently of transport considerations for isothermal CPCs. The characteristic volume of the supersaturated region may be used as an input to a perfectly mixed, uniform temperature model. Given some upper bound in the tolerable homogeneous nucleation rate, the theoretical maximum attainable saturation ratio may be calculated from homogeneous nucleation theory to make a theoretical calculation of the maximum attainable saturation ratio. As can be seen with Eq. (4.1), the classical homogeneous nucleation rate is a strong function of the saturation ratio and, hence, the total nucleation rate that is found from integration over the control volume will be dominated by the region of highest supersaturation.

The transport modeling presented here for isothermal UCPCs presents a basic set of guidelines for the design and operation of such devices. The proposed isothermal operation resolves the longstanding issue with CPCs potentially evaporating nascent

particles. While the model could stand to be refined with a more physically reasonable inlet concentration profile, for example, this type of fine-tuning may have limited impact. The real need for the next generation of detectors is fast-response devices that count all of the particles which enter them, maximizing the signal to noise ratio. Beyond maximizing the signal to noise ratio, the short response time would enable rapid classification of an aerosol size distribution when the CPC is integrated into a scanning electrical mobility spectrometer instrument. An example design of an isothermal mixing-type CPC is shown in Fig. 4.7. Fast-response devices are essential for the classification of rapidly evolving systems such as the CLOUD chamber; the development of a mixing-type CPC that prevents nascent particle evaporation would enable measurement of size distributions with excellent time resolution.

Independent of the details of detector design, experimental validation of the working fluid performance is essential. The straightforward, tractable nature of the present algorithm for working fluid selection, which relies heavily upon approximate analytical expressions and physical property correlations, comes at the expense of capturing details that may prove to be significant in making measurements. For example, interactions between the working fluid vapor and trace species in the aerosol gas may result in multicomponent nucleation rates internal to the detector that are far greater than that estimated from classical homogeneous nucleation theory here. The key role of the present work is to propose a methodology for narrowing a large field of candidate working fluids to a handful; the experimental validation that follows is essential in determining which of this smaller pool of working fluids is most suitable for the application of interest.

4.6 Conclusions

Inspired by Stolzenburg (1988) and Iida et al. (2009), we developed a simplified set of guidelines for working fluid selection and isothermal UCPC design for operation at 180 K. It was shown that working fluid selection could be decoupled from transport modeling, making for a straightforward process that was illustrated for the extreme

example of sampling from the CLOUD chamber at 180 K. For the example of an isothermal UCPC, the maximum obtainable value of the signal to noise, which is proportional to the capillary cross-sectional area relative to that of the supersaturated sheath gas flow tube, was sought subject to a minimum tolerable centerline saturation ratio at the outlet of 80% of the inlet supersaturation. The optimum operating conditions in the governing dimensionless parameters, which were found to be ϵ/R and Gz, were then identified for a minimal plug flow model ($\epsilon/R = 0.21$ and $\mathrm{Gz} = 58$) and for a more physically realistic Poiseuille flow model ($\epsilon/R = 0.1$ and $\mathrm{Gz} = 35$). These values of the dimensionless groups were shown to be consistent with a device of physical size and operating flow rate that are within reason. It is recommended that future work seek to employ these candidate working fluids in a mixing-type CPC design that prevents nascent particle evaporation.

4.7 Figures

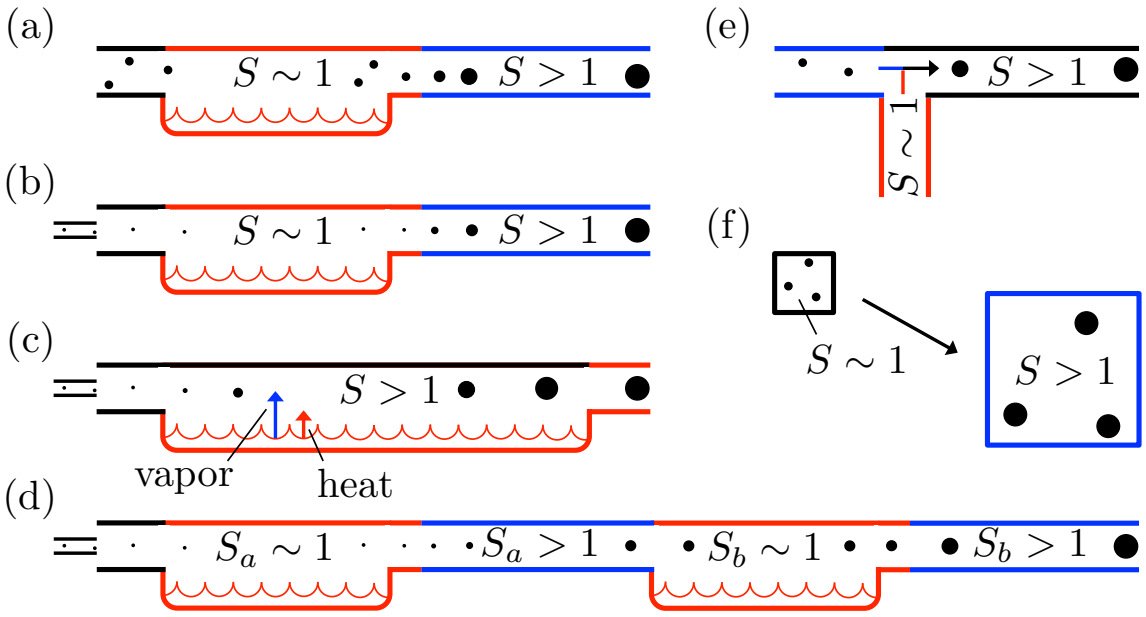

Figure 4.1. Several commonly used condensation particle counter designs. Generally, incoming aerosol is first heated whilst being exposed to the saturated vapor of the working fluid. The mixture is then cooled to supersaturate the working vapor so that it activates and grows the particles to roughly 10 μm so that they may be counted optically using a laser light scattering detector. The CPCs are: (a) broadly used continuous flow design [44]; (b) the UCPC that decreases diffusional losses [21, 32]; (c) the water CPC [48]; (d) the two-stage CPC [36]; (e) the mixing-type CPC or PSM [37]; and (f) the expansion-type CPC [45].

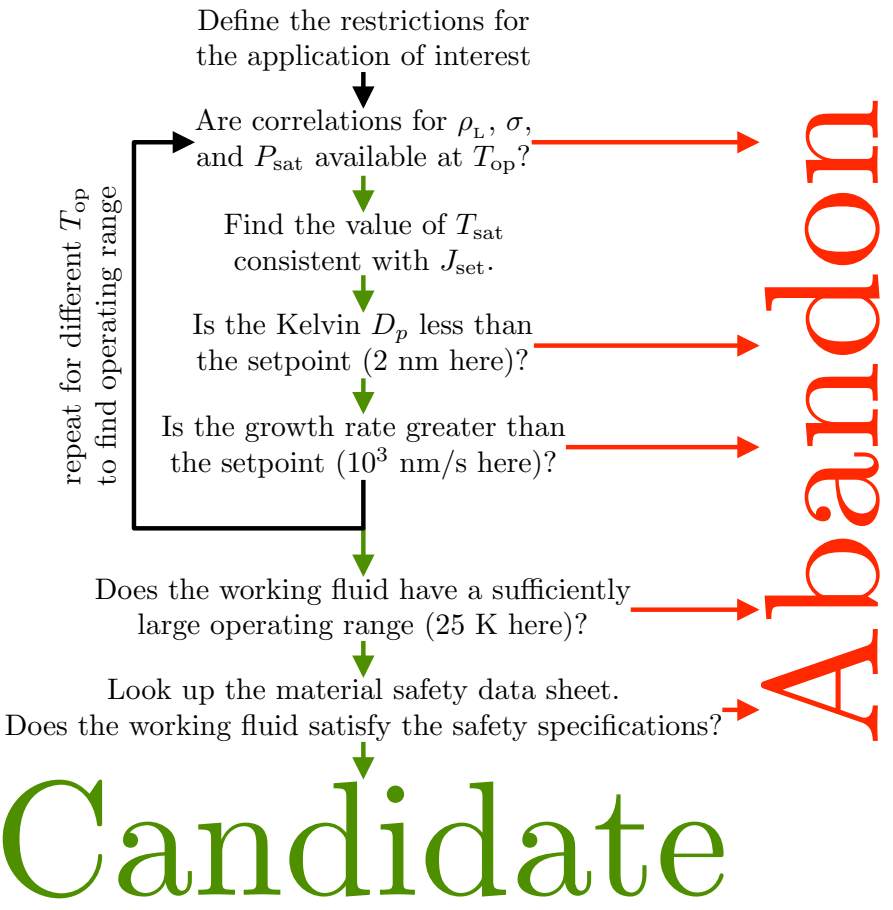

Figure 4.2. Working fluid selection process, inspired by Iida et. al. (2009).

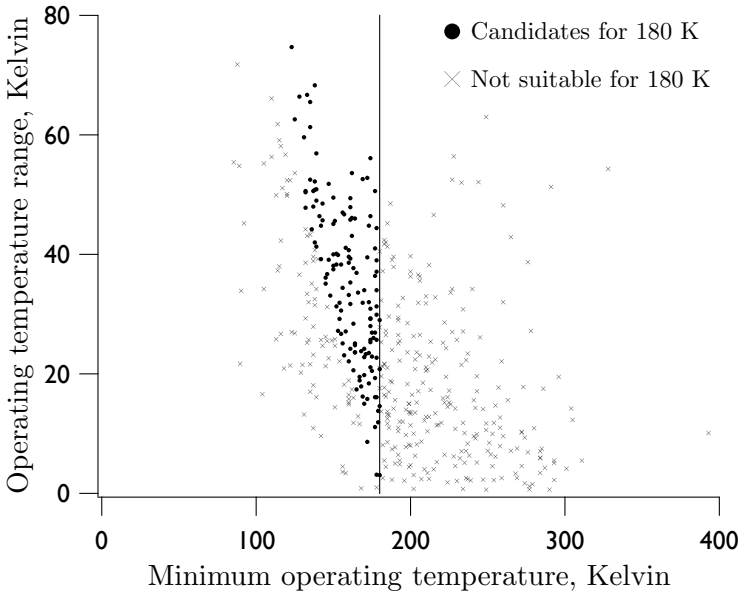

Figure 4.3. The minimum and range of the operating temperature for working fluids that are theoretically capable of activating particles with a Kelvin $D_p < 2$ nm, with an emphasis on those suitable for 180 K.

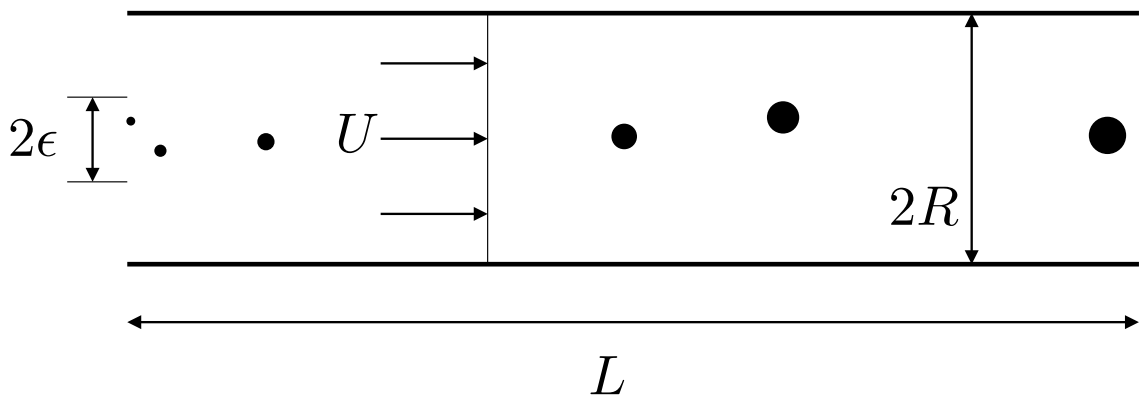

Figure 4.4. The supersaturated region of a plug flow isothermal UCPC.

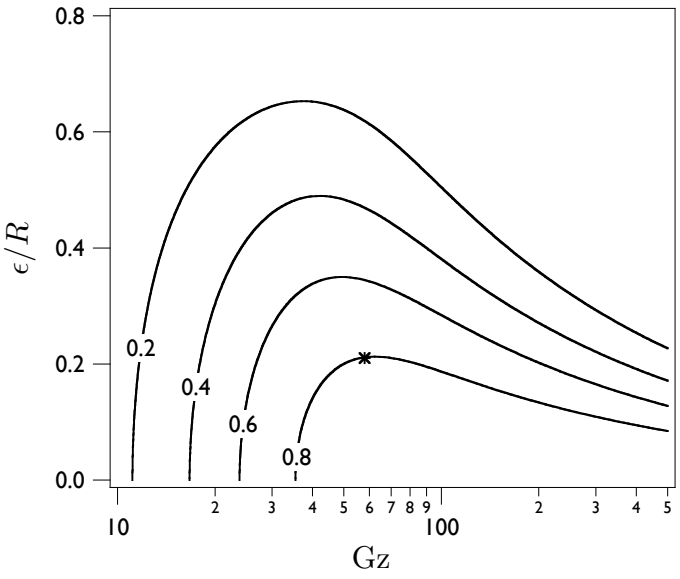

Figure 4.5. The centerline outlet saturation ratio $S[0, L]$ relative to that of the inlet for an isothermal laminar-flow CPC as a function of the Graetz number Gz and the dimensionless extent of the aerosol capillary ϵ/R for a minimal plug flow model. For $S[0, L]/S_0 = 0.8$, which is specified in the present example as the minimum tolerable value, at most $\epsilon/R = 0.21$ when $\mathrm{Gz} = 58$; this point is marked with an asterisk. This represents the most favorable configuration given the restriction in centerline saturation ratio.

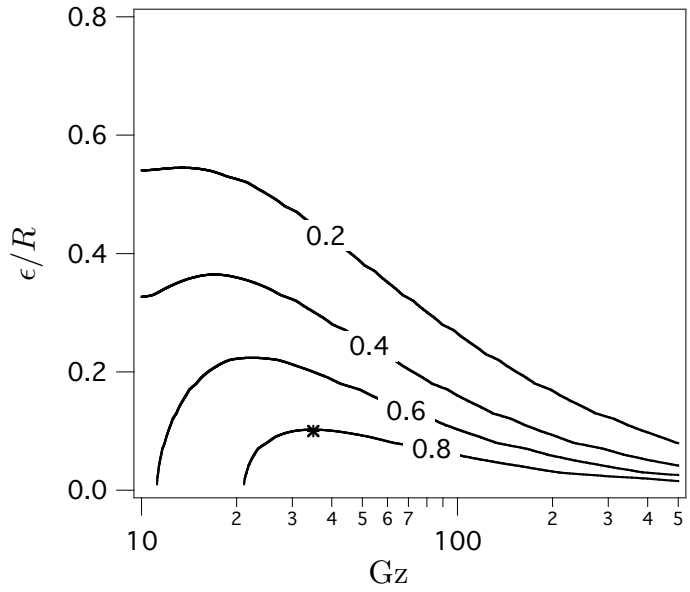

Figure 4.6. The centerline outlet saturation ratio as a function of ϵ/R and Gz for a isothermal UCPC with Poiseuille flow, as found numerically with COMSOL. For $S[0,L]/S_0 = 0.8$, which is again specified as the minimum tolerable value, at most $\epsilon/R = 0.1$ when $\mathrm{Gz} = 35$; this point is marked with an asterisk.

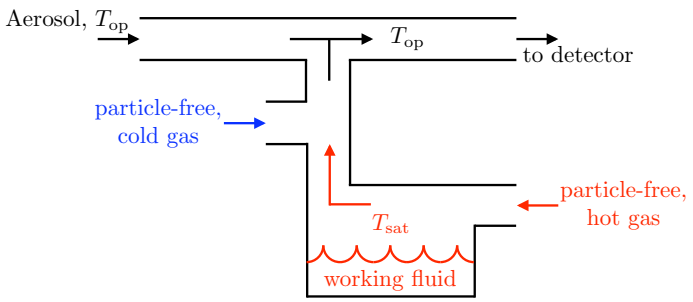

Figure 4.7. A conceptual design of an isothermal mixing-type CPC. Warm air saturated with the working fluid is rapidly cooled to the operating temperature T_{op} just before it is mixed with the aerosol.

4.8 Table

Table 4.1. Candidate working fluids for an isothermal CPC for the CLOUD chamber at $T_{op} = 180$ K. The names that appear in bold, 4-methylnonoane and m-ethyltoluene, have the most favorable National Fire Protection Association (NFPA) ratings among this candidate pool in the dimensions relevant for CLOUD, with a level of 0 for health (H), 2-3 for flammability (F), and 0 for reactivity (R), as reported on their respective Materials Safety Data Sheets.

Name	CAS Number	Formula	MW	T_f	T_b	Values at $T_{op} = 180$ K							NFPA		
						T_{sat}	Kelvin D_p	dD_p/dt	S_0	P_{sat}	σ	ρ_L	H	F	R
			kg/kmol	K	K	K	nm	nm/s		Pa	N/m	kg/m^3			
1,2-dichloropropane	78-87-5	$C_3H_6Cl_2$	113	173	370	243	1.6	1.3e6	9.2e2	2.6e-1	0.047	1300	1	3	0
1,3-cyclohexadiene	592-57-4	C_6H_8	80.1	161	353	234	1.7	1.7e6	3.8e2	7.3e-1	0.045	960	1	3	0
1,3-dichloropropane	142-28-9	$C_3H_6Cl_2$	113	174	394	238	1.5	1.6e5	2.1e3	1.5e-2	0.050	1300	2	3	0
1-bromobutane	109-65-9	C_4H_9Br	137	161	375	226	1.7	1.8e5	4.6e2	7.1e-2	0.040	1400	2	3	0
1-iodopropane	107-08-4	C_3H_7I	170	172	376	235	1.7	4.8e5	3.9e2	2.8e-1	0.043	2000	1	2	1
1-nitropropane	108-03-2	$C_3H_7NO_2$	89.1	169	404	222	1.6	1.5e4	4.1e2	6.5e-3	0.043	1100	1	3	0
4-methylnonane	17301-94-9	$C_{10}H_{22}$	142	174	439	248	1.7	5.0e4	1.5e4	3.5e-4	0.035	820	0	2	0
allyl acetate	591-87-7	$C_5H_8O_2$	100	138	377	232	1.7	3.4e5	4.5e2	1.2e-1	0.041	1000	4	3	0
butyronitrile	109-74-0	C_4H_7N	69.1	161	391	215	1.7	2.1e4	1.5e2	2.4e-2	0.040	890	4	3	0
carbon disulfide	75-15-0	CS_2	76.1	162	319	228	1.7	5.2e6	7.2e1	1.8e1	0.050	1400	2	3	0
cumene	98-82-8	C_9H_{12}	120	177	426	240	1.6	3.9e4	7.1e3	7.3e-4	0.041	950	2	3	0
dichloromethane	75-09-2	CH_2Cl_2	84.9	178	313	225	1.6	3.8e6	1.0e2	9.2e0	0.051	1500	2	0	0
diethyl disulfide	110-81-6	$C_4H_{10}S_2$	122	172	427	242	1.5	4.3e4	5.4e3	1.2e-3	0.044	1100	2	2	0
ethyl iodide	75-03-6	C_2H_5I	156	162	345	226	1.7	9.0e5	1.3e2	1.8e0	0.044	2200	2	2	0
ethylbenzene	100-41-4	C_8H_{10}	106	178	409	239	1.6	1.1e5	2.7e3	5.7e-3	0.043	960	3	3	0
m-ethyltoluene	620-14-4	C_9H_{12}	120	178	434	247	1.5	5.4e4	1.2e4	5.9e-4	0.043	950	0	2	0
propyl butanoate	105-66-8	$C_7H_{14}O_2$	130	178	416	237	1.7	4.7e4	2.9e3	2.1e-3	0.037	970	2	3	0
propylbenzene	103-65-1	C_9H_{12}	120	174	432	242	1.6	3.7e4	8.3e3	5.9e-4	0.042	950	1	2	0
propylcyclohexane	1678-92-8	C_9H_{18}	126	178	430	242	1.7	6.0e4	5.9e3	1.2e-3	0.037	880	0	3	0
tetrahydrothiophene	110-01-0	C_4H_8S	88.2	177	394	235	1.5	1.5e5	1.1e3	2.6e-2	0.049	1100	2	3	0
toluene	108-88-3	C_7H_8	92.1	178	384	233	1.7	2.6e5	7.1e2	5.6e-2	0.043	970	2	3	0
tripropylamine	102-69-2	$C_9H_{21}N$	143	180	430	232	1.6	2.7e3	1.3e4	2.3e-5	0.033	830	3	3	0
valeronitrile	110-59-8	C_5H_9N	83.1	177	414	218	1.6	5.9e3	4.0e2	2.2e-3	0.038	890	2	2	0
vinylcyclohexene	100-40-3	C_8H_{12}	108	164	401	235	1.7	1.6e5	2.1e3	1.0e-2	0.040	920	2	3	0

Chapter 5

Gradient Focusing Ion Mobility Spectrometry

5.1 Abstract

We introduce a method for high resolution ion classification in the gas phase. A longitudinal gradient in the gas velocity is counteracted by electrophoretic displacement, leading to the establishment of stable stagnation regions for ions of different mobility. Ions are successively transmitted by increasing the applied electrical field. Whereas many ion mobility spectrometers suffer from resolution degradation owing to the finite size of the sample bolus, the gradient focusing method we present here overcomes this limitation by focusing the ions as they traverse the classification region.

5.2 Introduction

Ion mobility spectrometry (IMS) is broadly used for applications that include detection of chemical warfare agents, explosives, illicit drugs, and biomolecule analysis [49, 50, 51, 52, 53]. Related electrical mobility methods are used for particle sizing. The essential elements of IMS classification regions, as shown in Fig. 5.1, are sample introduction, axial transport of charged species by an electric field, a drift gas flow that prevents the accumulation of undesired contaminants in the system, and classified ion extraction for downstream detection or analysis [54]. Radial focusing of the ions in the center of the classification region is achieved in some instruments using RF or alternating field-based ion guides [55, 56]. One particularly effective approach is to install an ion funnel on the inlet and/or outlet to force ions to the centerline [57, 58].

These enhancements have, with a considerable amount of success, minimized signal degradation due to radial dispersion. Reductions in resolution by axial dispersion, on the other hand, has proven to be a more challenging problem.

Most ion mobility spectrometers operate in the time domain wherein a small sample bolus is introduced at one end of the classification channel. Ions migrate along the length of the spectrometer at velocities of

$$v_i \cong K_i \Delta\phi / L + v_{\text{drift}}, \tag{5.1}$$

where K_i is the ion mobility, $\Delta\phi$ is the potential difference over the length, L, of the classification region, and v_{drift} is the velocity of the drift gas flow, which is generally negative. The residence time of the target separand in the classifier is, thus,

$$\tau_r = L / v_i. \tag{5.2}$$

The ability of an IMS instrument to resolve a given target separand is quantified by its resolution

$$\mathrm{R} = \tau_r / \Delta t_{_{FWHM}} \tag{5.3}$$

where $\Delta t_{_{FWHM}}$ is the full width at half maximum of the peak [59]. While values of $\mathrm{R} \sim 10^2$ have been achieved, higher resolution is needed to maximize the peak capacity of the instrument. In the idealized case of a small bolus that can be approximated by a delta function, the resolution of most IMS instruments may be approximated as

$$\mathrm{R} \approx \left(\frac{ze\Delta\phi}{kT \cdot 16 \ln 2} \right)^{1/2}, \tag{5.4}$$

where $\Delta\phi$ is the potential difference over the length of the classification region, z is the number of elementary charges on the ion, e is the elementary charge, k is the Boltzmann constant, and T is the temperature [60]. At room temperature, $e/(kT) = 38.9\ \mathrm{V}^{-1}$. The maximum field that can be supported at atmospheric pressure without electrostatic breakdown is $O(10^6\ \mathrm{V/m})$, so the resolution of a singly charged ion

transported through a 0.1 m IMS instrument is

$$\mathrm{R} \approx \left(\frac{10^6 \text{ V/m } \cdot 0.1 \text{ m } \cdot 1 \cdot 38.9 \text{ V}^{-1}}{16 \ln 2} \right)^{1/2} = 6 \times 10^2, \tag{5.5}$$

considerably larger than the observed levels of $O(10^2)$. Finite sample bolus size and other instrument nonidealities limit R in present instruments.

Nonuniform electric fields have been used to increase the resolution. One IMS instrument that makes use of a nonuniform field, called the field asymmetric IMS (FAIMS) or the differential mobility spectrometer, leverages the nonlinear dependence of ion mobilities on field strength to focus the target ion to the center of a channel, while depositing contaminants on the walls [61]. An axial flow advects the classified target to the detector. In contrast to the time domain ion mobility spectrometer, the FAIMS can classify ions continuously, acting as a band-pass filter that transmits ions within a narrow range of mobilities. While the entire ion mobility spectrum can be determined from a single sample bolus in time-domain IMS, a FAIMS instrument must step through the full range of compensation voltages to obtain an ion spectrum. That spectrum provides a signature for the composition of the sample mixture; the quantity measured is, however, not the ion mobilities, but rather a convolution of the mobility with the nonlinear mobility responses of the transmitted ions. Furthermore, because a carrier gas flow is used to convey the ions through the FAIMS, neutral molecules are also transmitted, complicating non-electrometric detection methods. Another class of instruments that make use of a nonuniform field is called traveling-wave IMS. Traveling-wave IMS mitigates the instrumental non-ideality from axial potential wells that emerge from the stacked ring radial ion focusing [62, 63]. A temporally varying field aids in the ions overcoming these potential wells that would otherwise hinder the transport of a fraction of the target and, hence, increase axial dispersion.

Commonly used aqueous separation methods, which are considerably different from gas-phase IMS, also suffer from resolution degradation as a result of axial dispersion [64]. However, aqueous gradient focusing methods [65], which are extensions

of classical aqueous techniques, produce self-sharpening peaks by displacing each separand to its respective stable stagnation region. These methods require two counteracting modes of displacement, one of which varies monotonically in strength in the classification region. Though many different modes of displacement and combinations thereof are conceivable, the most extensively explored configuration imposes a fluid flow in opposition to electrophoretic migration [66, 67, 68, 69, 70, 71]. The scaling of the resolution and peak capacity for these methods is generally favorable relative to other aqueous separation alternatives [65].

There are, however, fundamental differences in the physics of charging and surface adhesion for species in a gas relative to a buffer solution. These differences prevent direct mapping of many of the most successful aqueous gradient focusing methods to the gas-phase. One of the more common gradient focusing methods, isoelectric focusing, concentrates the separands about a stagnation region where they have a effective charge of zero [72]. This is accomplished by imposing a pH gradient on the fluid, but no analogous method is available to produce a steady spatial gradient of the effective particle charge in the gas phase. The incorporation of stationary phases, as suggested by the method of counteracting chromatographic electrophoresis [67, 68], is out of the question with IMS since the ions would bind strongly to the stationary phase and not easily be resuspended.

Nonetheless, gradient focusing of gas ions is possible with alternate approaches to establishing the gradient; this paper describes a method in which a gas velocity gradient is established to enable ion focusing.

5.3 Description

Figure 5.2 illustrates a velocity gradient ion mobility spectrometer in which electrophoretic migration is opposed by a drift gas flow whose velocity is maximum at the outlet end of the classification region. The gas velocity decreases as it approaches the classifier entrance due to suction through a porous channel wall. Ions introduced near the centerline of the device migrate against the drift gas flow under the action of

an applied electric field, only to accumulate where the gas velocity exactly balances the migration velocity, i.e., where

$$U\left[r,z\right]=K\Delta\phi\left[t\right]/L. \tag{5.6}$$

Increasing the applied electric field as a function of time enables successive elution of separands as the stagnation regions shift toward the classifier outlet.

To attain high resolution, both the electric field and the longitudinal velocity must be uniform over the cross section of the region where ions are focused. Wall suction is an established method that is used to reduce boundary layer thickness, i.e., to reduce the thickness of the region where viscous dissipation leads to transverse gradients in the streamwise (longitudinal) velocity, though it has been used mainly in aircraft applications. Here, the extraction of gas through the porous walls reduces the region where the longitudinal velocity varies with the radius to a relatively thin boundary layer near the porous wall of the tube. The uniform suction flow out of the walls may be obtained by using frits or other porous media, and the ions may be focused radially using RF or alternating fields which provide for steep potential gradients [55, 56] that prevent diffusion to the boundary layer near the walls where the radial velocity profile is nonuniform.

To illustrate the premise of this method, consider nitrogen as a representative drift gas. At 25°C and 1 atm, nitrogen has a kinematic viscosity $\nu = 1.6 \times 10^{-5}$ m^2/s. A relatively small ion mobility $K = 10^{-4}$ m^2/V/s (chosen as such to be conservative) and a potential difference $\Delta\phi = 10^5$ V applied over a distance $L = 0.1$ m result in a representative unopposed migration velocity of

$$K\Delta\phi/L = 10^{-4}\ \text{m}^2/\text{V/s}\cdot 10^5\ \text{V}/0.1\ \text{m} = 1\ \text{m/s}, \tag{5.7}$$

where it should be noted that the applied field of 10^6 V/m is a factor of 3 less than the breakdown field strength for atmospheric pressure nitrogen. Following from the calculation of the migration velocity is the characteristic drift gas velocity $U \sim 1$ m/s and, for a device of aspect ratio $L/R = 10$, where R is the radius of the classification

region, the characteristic Reynolds number Re is

$$\mathrm{Re} = \frac{2UR}{\nu} = \frac{2 \cdot 1 \text{ m/s} \cdot 0.01 \text{ m}}{1.6 \times 10^{-5} \text{ m}^2/\text{s}} = 10^3. \tag{5.8}$$

In order to minimize the radial extent of the boundary layer, the radial suction velocity at the wall is set to 0.05 m/s, which results in the drift gas flow rate being precisely equal to the suction gas flow rate. The Navier-Stokes equations for the classification region were solved for this representative set of conditions using COMSOL, and the favorable results are shown in Fig. 5.3.

The sample introduction and classified sample extraction stages must be designed thoughtfully in order to ensure that they do not contribute to signal or resolution degradation. With the peaks self-sharpening in response to any perturbations in the classification region, the performance of the instrument will be sensitive to dispersion at the inlet and outlet. At the inlet, a smaller concentric tube may be used for sample introduction, but care should be taken to ensure that the flow from the inlet has manageably small effects on the velocity profile in the classification region and that the ions do not disperse radially. Axial dispersion, while strongly undesirable at the outlet, may be tolerated to an extent with sample introduction because of the focusing downstream in the classification region. Ions should be focused radially toward the centerline at the outlet, which can be done using an ion funnel [57, 58].

The specific functional forms of the velocity field gradient and the temporally varying electric field should be such that the resolution is maximized for the separands of interest. The resolution for this intrinsically dynamic measurement may vary wildly depending on the operating conditions; theory and simulation may be used to guide the selection of the optimal values of relevant parameters. In the end, the only limitations to obtaining arbitrarily large resolutions will be space charge, outlet, and/or finite detector size effects.

5.4 Figures

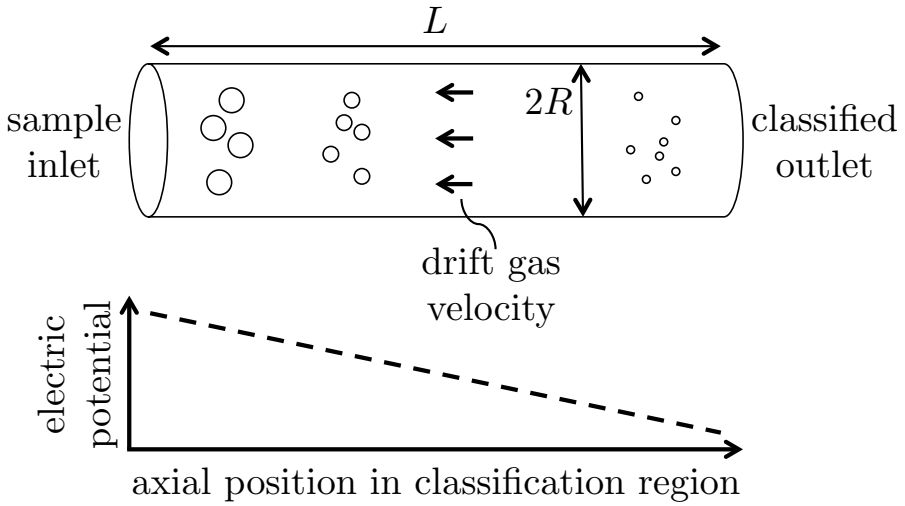

Figure 5.1. The classification region of an ion mobility spectrometer. Charged constituents of the sample migrate axially in the presence of an electric field at different rates. Smaller, more highly charged particles migrate faster than larger particles that suffer more collisions with the drift gas. The inert drift gas flow prevents the build-up of contaminants in the system and their transport to the end of the spectrometer. Once ions are transmitted, they are either sensed by an electrometric detector or transported for downstream analysis by a second instrument such as a mass spectrometer.

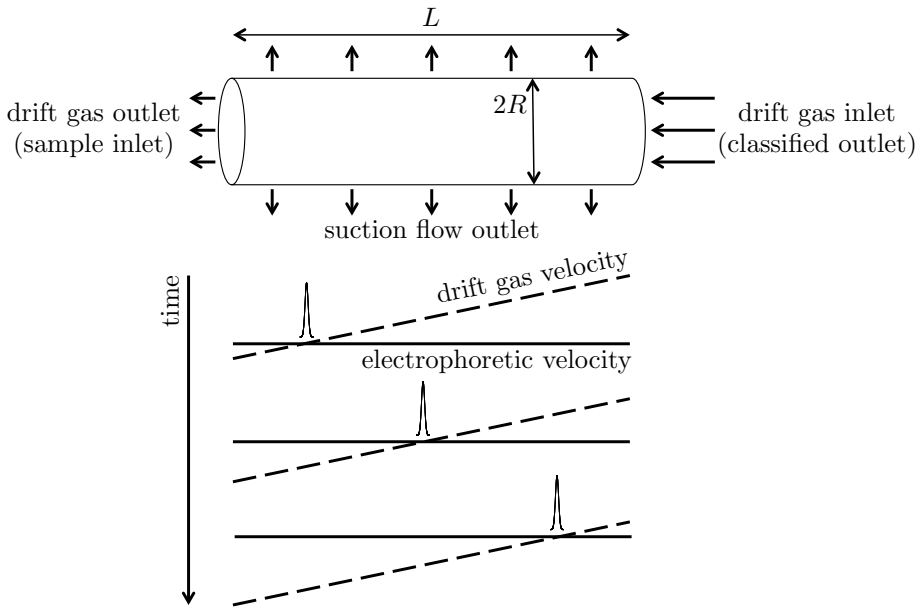

Figure 5.2. The principle of velocity gradient focusing ion mobility spectrometry. Ion migration in the axial electric field is counteracted by a spatially nonuniform opposing flow. The ions concentrate at their respective stagnation regions, which vary depending on their respective values of the ion mobility K. The magnitude of the electric field increases as a function of time, displacing the stagnation regions until they successively reach the classified outlet.

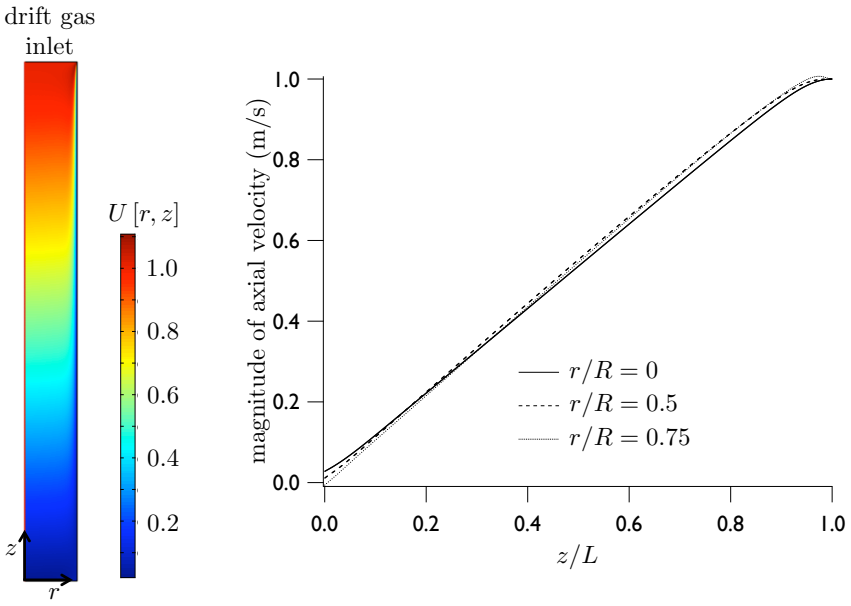

Figure 5.3. The drift gas velocity profile for a representative set of operating conditions for a velocity gradient focusing IMS instrument, found from solving the Navier-Stokes equations using a finite element scheme in COMSOL. The similarity between the axial velocity gradient at different radial positions demonstrates that, for ions that are adequately focused in the radial direction, Taylor dispersion will not play a significant role in the degradation of the resolution. The boundary conditions used here were a uniform velocity of 1 m/s at the drift gas inlet (classified outlet), a suction velocity at $r = R$ of 0.05 m/s, an isobaric boundary condition at the drift gas outlet (sample inlet), and a symmetry condition at the centerline.

Chapter 6

Continuous Opposed Drift Electrophoresis

6.1 Abstract

We introduce a new scalable method for high resolving power purification of nanoparticles and microparticles. A uniform electric field counterbalanced by an opposing flow isolates the target fraction as an orthogonal primary flow continuously introduces sample and advects product to the outlet. Inspired by an aerosol characterization technique, where making the most of dilute samples is a must, continuous opposed drift electrophoresis (CODE) is set apart from other aqueous methods that require large separand concentrations for scalable throughput. Analytical and simulation results are presented to illustrate the power of CODE to isolate a single target fraction without the drawbacks of particle/particle and separand/buffer interactions. Suitable for a broad range of applications, CODE is a particularly appealing solution for scalable therapeutic production, where a single fraction is needed at high purity, and microparticle separations, where high resolving power options are limited.

6.2 Introduction

There is a need for new, scalable, high-resolving-power separation techniques for particles ranging from 1 nm – 10 μm. Few methods exist for size-resolved separation of microparticles like bacteria and cells for classification and environmental monitoring [73]. Beyond the analytical-scale, options for preparative to industrial-scale purification for applications such as therapeutic production are extremely limited, with chromatography frequently being the only option [74, 75, 76]. In general, as target particle size or throughput increases, the options for high resolving power separations quickly decrease.

Successful analytical protein separation methods that exploit the principle of gradient focusing show promise for broader applications with big particles and large sample volumes. Gradient focusing, as shown in Fig. 6.1, fractionates a complex mixture by displacing the separands from their initial positions to stable stagnation regions [65]. The subset of gradient focusing methods that makes use of electrophoresis with an opposing flow, counteracting chromatographic electrophoresis (CACE) and field gradient focusing (FGF), are particularly notable because of their resolution and scalability [67, 69]. CACE provides for a gradient in the interaction between the separands and the stationary phase packing, typically the accessible volume coefficient. A hybrid of chromatography and electrophoresis, CACE uses an electric field with an opposing flow to focus the particles at their stagnation region. FGF is a free-solution method where a gradient in the electric field is used in tandem with an opposing flow to fractionate a sample.

To fully realize the potential of CACE and FGF as a scalable techniques, the basic batch methods must be modified to operate continuously. Many of the principles applied in the design of free-flow electrophoresis are instructive for adapting batch electrophoretic methods such as CACE and FGF to continuous operation [77]. A thin-gap planar geometry is preferable for high-throughput with tractable temperature management. The application of the field orthogonal to the primary flow, as shown in Fig. 6.2, allows for steady sample introduction and product removal. With continuous

CACE, it is easier to pack a columnar geometry than a planar one. Casting and functionalizing monoliths *in situ* using photopolymerization would both enable a shift to thin-gap planar geometries and make for substantially easier fabrication, as packing gradients is an onerous task [68, 71].

Innovations in the field-flow fractionation (FFF) community set the stage for the scale-up of FGF. FFF is a batch analytical method that adopted a thin-gap planar geometry for convenience with the application of a field force that is normal to the primary flow. Challenges arising from large particles, wall roughness, surface adhesion, and impractically long retention times motivated the use of FGF [66]. Subsequently, the outlet sample streams were split to increase the sensitivity of the signal [78]. The integration of FGF with split outlets made for a continuous 'equilibrium operation split-flow lateral transport thin' method, as shown in Fig. 6.3 [79, 80]. A scaled-up version was later independently developed [70, 81]. The method was also extended to nonlinear fields applied across the width of the device [82, 83].

Continuous FGF, as with all fractionation methods, requires large separand concentrations to achieve large-scale throughput. Particle/particle interactions, which increase in frequency at high concentrations, degrade resolution when target species bind to form a dimer, for example. With biological samples like proteins there are a plethora of possible interparticle interactions [84, 85, 86]. Resolution is further degraded by separand/buffer interactions that result in undesired pH and conductivity gradients in the vicinity of the stagnation regions [87, 88]. A fundamentally different approach is needed for scalable aqueous particle separations without the drawbacks of nonlinear concentration effects.

In the aerosol characterization community, a key objective is to obtain continuous high resolving power separations of intrinsically dilute samples. The opposed migration aerosol classifier (OMAC), a dilute electrophoretic method, suggests a scalable aqueous method where separand concentration effects could be avoided entirely [19]. As shown in Fig. 6.4, a constant electric field is opposed by a steady counterflow to continuously isolate a single fraction. Excluding FGF, counterflows have only been used with aqueous electrophoretic methods to counteract electroosmotic flow,

with the hope of increasing resolution amongst the many fractions that were sought [89, 90]. Because of their origins in analytical methods, scalable aqueous separations have been designed to collect a large number of fractions, even if the collection of many fractions comes at the expense of undesired concentration effects. The OMAC inspires a scalable method that is liberated from the mindset of maximizing fractions by purifying a single fraction at high resolving power and high-throughput in the dilute limit.

Continuous opposed drift electrophoresis (CODE), inspired by the OMAC, introduces innovations from the aerosol characterization community to aqueous electrophoretic separations. CODE is a scalable thin-gap method where a single fraction is isolated at high resolving power. By isolating only a single fraction, the entire cross-sectional area of the device may be used for sample introduction and product collection. The substantial reduction in fractions combined with continuous operation opens the door to significant scalability without the drawbacks of concentration effects.

6.3 Theory and simulation

In general, any two physical mechanisms that steadily displace particles could be used as the basis of a continuous aqueous single fraction method inspired by the OMAC. Electrophoresis with a steady opposing flow was chosen because of the speed and selectivity of this combination. CODE, as shown in Fig. 6.5, may be operated with the field applied across the width or the thin-gap. In both cases, several approximations are generally reasonable. As CODE is designed for optimal operation in the dilute limit, concentration effects are ignored. Furthermore, as a single buffer is used, the pH and conductivity are taken to be constant everywhere in the channel. A notable aside is that undesired pH and conductivity gradients arise with continuous FGF other concentrated methods, decreasing resolution and significantly complicating the modeling [87, 88]. Temperature gradients are ignored as external cooling may be used to remove Joule heat. The velocity profiles are presumed to be uniform; the effect of

the parabolic flow in the thin dimension on performance will be discussed later. To obtain high-throughput with tractable heat removal, there is a separation of length scales $h/W \ll 1$ and $h/L \ll 1$, where h is the thin-gap height, W is the width, and L is the length. It is also frequently true that $W/L \ll 1$ – this is stipulated here for simplicity. Finally, for convenience with comparing the width and thin-gap modes, the electroosmotic flow that would typically develop when the field is applied across the width is ignored. Note that the electroosmotic flow may be suppressed with a wall coating of nil zeta potential or by using moving boundaries [91, 92]. Given the above assumptions, the governing equation for CODE at steady state is (in dimensionless form):

$$\frac{\mathrm{Pe}}{\mathcal{R}_{\mathrm{nd}}}\frac{\partial C}{\partial x} + \mathrm{Pe}\left(1 - \frac{\mu}{\mu^*}\right)\frac{\partial C}{\partial \xi} = \frac{\partial^2 C}{\partial \xi^2}, \tag{6.1}$$

with boundary conditions

$$C\left(x,\ 0\right) = 0,\ C\left(x,\ 1\right) = 0,\ \text{and}\ C\left(0,\ \xi\right) = 1, \tag{6.2}$$

where Pe is the Péclet number, $\mathcal{R}_{\mathrm{nd}}$ is the nondispersive resolving power, C is the separand concentration, μ^* is the target mobility, and ξ is the direction that is aligned with the potential drop (i.e., $\xi = z$, the smallest dimension, for the thin-gap mode). The migration Péclet number $\mathrm{Pe} = \mu^* \Delta\phi / D$ is the ratio of advective to diffusive transport, where $\Delta\phi$ is the potential drop across the channel, and D is the separand diffusion coefficient. The nondispersive resolving power is $\mathcal{R}_{\mathrm{nd}} = \mu^* \Delta\phi L / U\ell^2$, where ℓ is the length scale of the direction that is aligned with the potential drop and U is the average sample flow velocity along the length of the classification region. In the kinematic limit, particles with mobilities in the range $-\mathcal{R}_{\mathrm{nd}}^{-1} < 1 - \mu/\mu^* < \mathcal{R}_{\mathrm{nd}}^{-1}$ are transmitted, which can be adjusted to an arbitrarily small window for $\mathcal{R}_{\mathrm{nd}} \gg 1$.

The theoretical yield was found by solving Eq. (6.1) with boundary conditions Eq. (6.2) using separation of variables and integrating to find the average outlet concentration. The results are shown in Fig. 6.6, which shows that arbitrarily tight fractions may be transmitted even when diffusion is included by operating at large Pe and $\mathcal{R}_{\mathrm{nd}}$. This first-order analysis, however, ignores the effect of the parabolic flow

in the thin dimension on performance.

The effect of Poiseuille flow in the thin dimension can be quite dramatic, especially when the potential drop is across the width. The dimensionless number that governs the importance of the parabolic shape of the flow profile is the Graetz number

$$\mathrm{Gz} = \frac{h^2/D}{\ell^2/\mu^*\Delta\phi} = \mathrm{Pe}\left(\frac{h}{\ell}\right)^2, \tag{6.3}$$

the ratio of the characteristic time for sampling the streamlines in the thin dimension to the characteristic time for advection. The increase in dispersion arising from diffusion normal to a nonuniform velocity profile is called Taylor dispersion, which increases the effective diffusion coefficient by a factor of $(1 + \mathrm{GzPe}/210)$ [93]. The performance of CODE for finite Gz was found theoretically by incorporating this increase in effective diffusion coefficient into Eq. (6.1) and separately by Brownian dynamics simulation ([26, 27, 94]; see also Appendix A). Figure 6.7 illustrates that for a representative separation the yield drops dramatically when the condition $\mathrm{Gz} \ll 1$ is not satisfied. In the ballistic limit $\mathrm{Gz} \to \infty$, where diffusion is negligible, Fig. 6.8 shows that the highest resolution fraction that can be isolated is near $\mu/\mu^* = 3/2$, not $\mu/\mu^* = 1$.

While large Gz diminishes yield when the potential drop is across the width, $\mathrm{Gz} \gg 1$ is actually necessary for high resolving power separations in the thin-gap mode where Gz reduces to Pe. When the potential drop is across the thin dimension, the opposing flow may be made effectively uniform by using rigid porous media for walls. Since it may be well-approximated as uniform, the opposing flow does not contribute to dispersion. Sampling the primary flow streamlines then comes at the expense of diffusive losses. Brownian dynamics simulation results for the thin-gap mode are shown in Fig. 6.9.

6.4 Discussion

As with other planar electrophoretic methods, the throughput of the target fraction in CODE is proportional to

$$\dot{m} \sim C_o UWh/N, \tag{6.4}$$

where C_o is the separand concentration at the inlet and N is the number of fractions collected. Whereas $N \sim 10 - 10^2$ for continuous FGF and free-flow electrophoresis, CODE's optimization for continuous single fraction collection allows for a factor of N reduction in operating concentration at constant throughput. Operation in the dilute limit minimizes the effects of particle/particle and separand/buffer interactions on the resolution of the separations. CODE's scalability in the dilute limit sets it apart from other separation methods.

While both the width and thin-gap modes are optimized for dilute separand concentrations, there are advantages to each that make them particularly well-suited for different applications. When selecting between the width and thin-gap modes, temperature control is an important consideration. The rate of energy generation per unit volume by Joule heating is

$$\frac{\dot{S}}{LWh} = \sigma \left(\frac{\Delta\phi}{\ell} \right)^2, \tag{6.5}$$

where σ is the electrical conductivity. Consider, for example, a separation that is done at identical resolution (fixed Pe and $\mathcal{R}_{\text{nd}}$) on geometrically identical devices with a consistent buffer and target species. Application of the field across the width results in a considerably smaller rate of heat generation. Since $\dot{S} \sim \ell^{-2}$, the rate of heat generation is smaller by a factor of $(h/W)^2$, which is several orders of magnitude for $h/W \ll 1$. In general, therefore, the width mode is preferable for high resolving power separations of small particles as they require large potential drops to obtain large Pe. From a throughput perspective, the thin-gap mode has a similarly impressive edge. As $\mathcal{R}_{\text{nd}} \sim U^{-1}\ell^{-2}$, the primary velocity (and, hence, the throughput) is larger by a factor of $(W/h)^2$. Hence, providing the required heat removal is tractable, the

thin-gap mode offers considerably more throughput when all else is held constant.

Fabrication considerations are also relevant when selecting the mode. For high resolving power continuous microanalysis, it is considerably easier to make a width mode device. There is no need for smooth porous boundaries separated by a relatively small distance. Rather, standard polymer casting or etching techniques may be used to make channels with $h/W \ll 1$ so that the conditions $\mathrm{Pe} \gg 1$ and $\mathrm{Gz} \ll 1$ are simultaneously satisfied. Construction of a device that satisfies both $\mathrm{Pe} \gg 1$ and $\mathrm{Gz} \ll 1$ becomes considerably more challenging for larger separands and larger instruments. As was seen in Fig. 6.7, satisfying the condition $\mathrm{Gz} \ll 1$ is critical for high-yield recovery of the target fraction. In fact, it was shown in Fig. 6.8 that the mobility for which the highest resolution is attained in the limit of $\mathrm{Gz} \to \infty$ shifts. In the ballistic limit, the fraction with the highest resolution has an electrophoretic velocity that very closely counterbalances the opposing flow velocity over the largest fraction of the channel height. With Poiseuille flow, the region where the velocity varies the least, that with the lowest shear rate, is in the center of the channel where the velocity is near its maximum, $3\mu^*\Delta\phi/W//2$. The results in Fig. 6.8 show that the highest resolution fraction is then, sensibly, near a mobility of $3\mu^*/2$. Operating in this limit of $\mathrm{Gz} \to \infty$, however, is undesirable because of the low yields under high selectivity conditions relative to those obtained when $\mathrm{Gz} \ll 1$. One approach that could facilitate scale-up of the width mode is to introduce a gel which would shorten the distance that particle must diffuse to sample all of the streamlines. In order to minimize dispersion from interactions with the stationary phase and to maximize throughput, low density gels with regular characteristic feature sizes are desirable. Ideally, the performance would approach that of a large number of smaller systems bundled together.

The optimal mode also depends on the physicochemical properties of the separand. While the target mobility (typically $O(10^{-8}\mathrm{m}^2/\mathrm{V/s})$) may be adjusted by changing the pH, the diffusion coefficient is a strict function of size. From the Stokes-Einstein-Sutherland relation, $D \sim a^{-1}$, where a is the hydrodynamic radius of the separand. As shown by Fig. 6.10, small-molecules, proteins and viruses with large values of D

sample streamlines in the thin-direction quickly, facilitating excellent separations in the width mode, but causing large diffusive losses (or, alternatively, impractically large heat removal requirements) in the thin-gap mode. Larger separands like bacteria and cells stay put on their streamlines and are best isolated with the thin-gap mode, where, as shown by Fig. 6.9, advective dispersion is not problematic. Indeed, the promise of thin-gap mode CODE for scalable microparticle (bacteria, cells, etc) separation at high resolving power is among the most exciting prospects for CODE.

Once the proper mode is selected for a particular application, preparative-scale throughput can be achieved by building a bench-top device of similar size to those made in the free-flow electrophoresis community, with $L \sim 1$ m, $W \sim 0.1$ m, and $h \sim 0.001$ m. The resolving power is proportional to the square root of the plate number, a metric commonly used in chromatography. Plate numbers of $O(10^4)$ or greater are typical; hence, a resolving power of at least 10^2 is desirable. Preparative scale throughput is $O(1$ g/hr); and typical titer concentrations are 1 g/liter. Thus, the sample flow must be ~ 1 liter/hr, and the crossflow is $\sim 10^2$ liters/hr. For a target separand of mobility $O(10^{-8}$ m^2/V/s), the field strength required is 2.8×10^4 V/m, which is near the upper bound of what is practical for free electrophoretic techniques given the need for heat dissipation. Further scale-up may be accomplished by stacking cells with alternating cooling layers in width mode, and by operating several instruments in parallel in thin-gap mode.

6.5 Conclusions

Continuous opposed drift electrophoresis, a scalable method for isolating nanoparticles and microparticles at high resolution in the dilute limit, was introduced. It takes a fundamentally different approach from other aqueous separation methods. Rather than scaling up a successful analytical fractionation method, CODE is inspired by the OMAC, an aerosol characterization technique. By continuously isolating a single fraction rather than many and using the entire cross-sectional area of the primary flow for sample introduction and product collection, CODE enables scalable separations

in the dilute limit so that deleterious concentration effects may be avoided.

The potential of the CODE width and thin-gap modes for scalable high resolving power separations was shown analytically and with Brownian dynamics simulation. The optimal mode depends on the particle diffusion coefficient, which is inversely proportional to the characteristic length scale of the separand. Small particles with large diffusion constants were shown to be best isolated in width mode, where the particles rapidly sample the streamlines in the thin dimension. The separation of small particles with the thin-gap mode leads to challenges arising from heat removal, which is several orders of magnitude larger than that for width mode. The thin-gap mode was shown to be optimal for larger particles like bacteria that stay near their initial streamlines, where the throughput for the width mode would be many orders of magnitude smaller.

The utility of CODE would be best demonstrated to the proteomics community by unmasking previously unseen proteins that readily bind to other particles. CODE is the ideal scalable method for isolating such proteins because it is by design a dilute method, so protein/protein interactions are minimal. CODE is very well-suited for therapeutic production because the objective is typically the isolation of a single fraction, that which contains the therapeutic agent. As for the microparticles separation community, where options are very limited at present, CODE is able to run at high resolving power without being overwhelmed by the advective dispersion that other methods suffer. In fact, it was shown that the thin-gap mode performance is best when the particles have the vanishingly small diffusion coefficients that are so problematic for most other methods.

In moving forward with demonstrating the promise of CODE for biological and inorganic applications, mindfulness of the norms in these fields with respect to separations will be critical. For example, in the proteomics community, high concentrations of separands are viewed as a positive outcome, even though they may come at the expense of resolution. Hence, for this application CODE product streams should have a downstream step for concentration by filtration or chromatography. In this way, the CODE purification is operated in its optimally dilute mode while the fraction

ultimately provided is at the desired concentration.

6.6 Figures

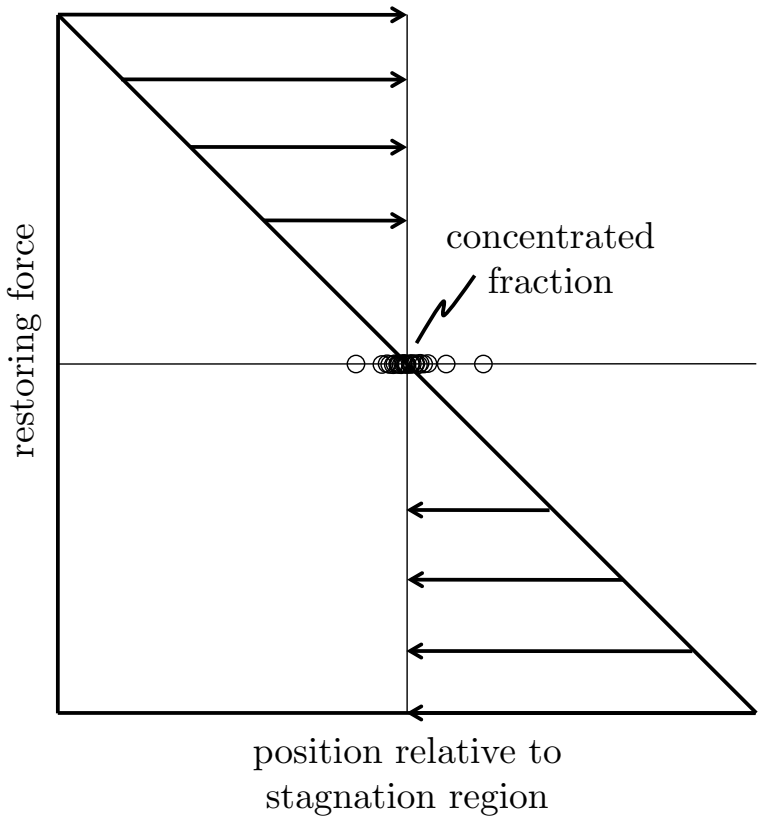

Figure 6.1. Principle of gradient focusing. Two or more modes of particle displacement are used in concert to concentrate the particles at their respective stagnation regions. For example, an electric field is applied across a gradient in pH to bring proteins to their point of zero net charge. Isoelectric focusing, as this method is called, is just a representative approach from the class of gradient focusing methods that can make use of electrophoresis, dielectrophoresis, sedimentation, and numerous other physical mechanisms for particle displacement [95].

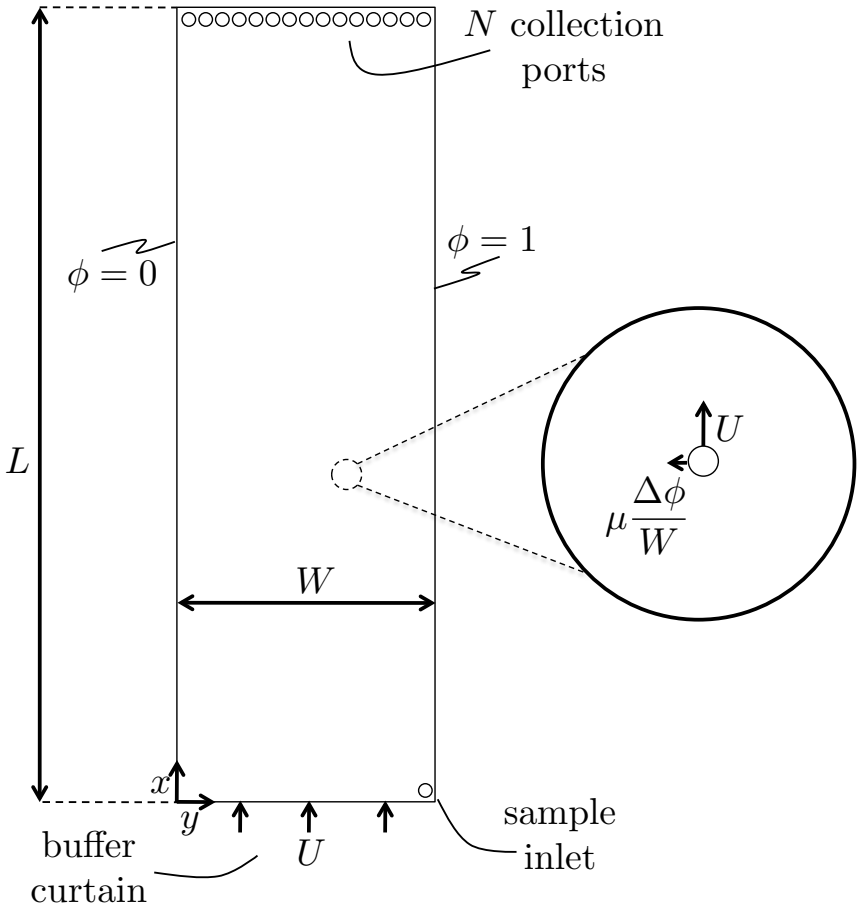

Figure 6.2. free-flow electrophoresis. The concentrated sample is continuously introduced to a planar thin-gap device through the inlet port. The buffer curtain flow advects the species to the outlet with an average velocity U. A uniform orthogonal electric field across the width $\Delta\phi/W$, where ϕ is the electric potential, deflects charged particles with mobilities μ. A large number of collection ports are used to continuously collect the numerous fractions at the outlet.

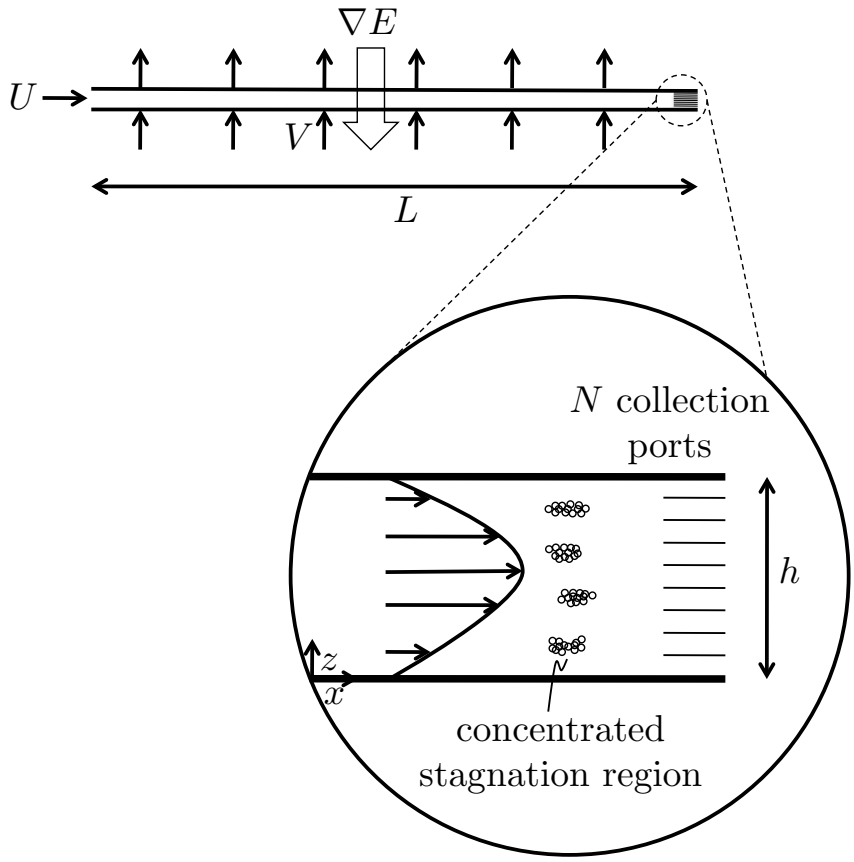

Figure 6.3. Equilibrium operation split-flow lateral transport thin continuous separation method. An electric-field gradient ∇E across the thin-gap h is opposed by a steady flow V that is normal to the primary flow U. Numerous concentrated fractions are then continuously captured at the outlet.

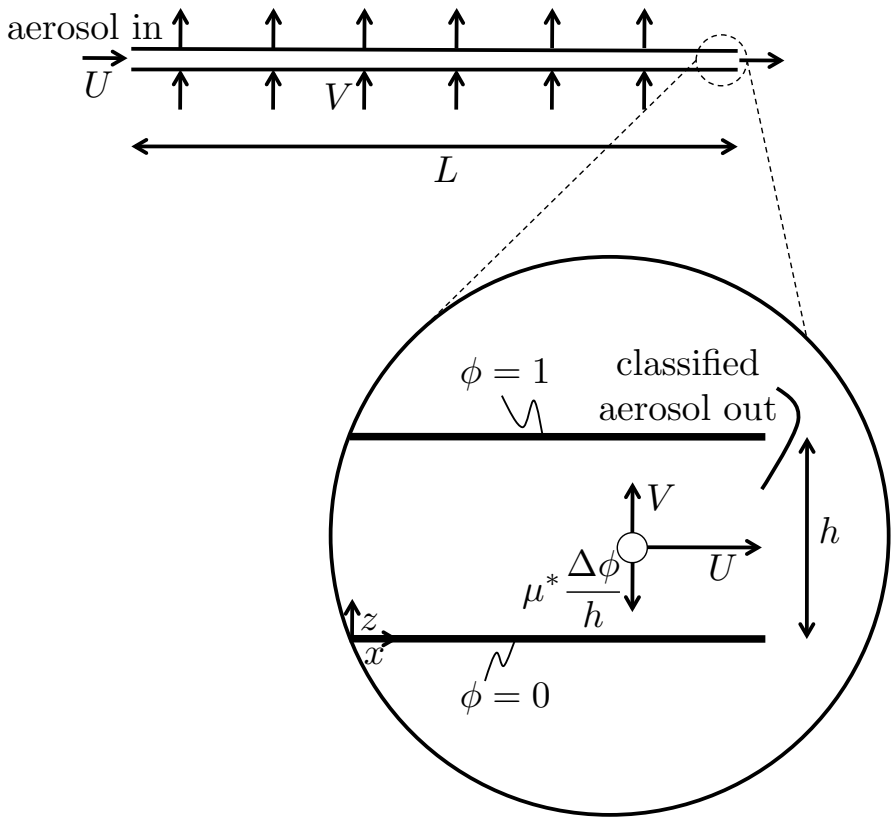

Figure 6.4. Opposed migration aerosol classifier. A dilute sample is continuously introduced to the active channel with average velocity U, where a uniform electric field $\Delta\phi/h$ applied across the thin-gap is opposed by a crossflow of average velocity V. The entire cross-sectional area of the outlet is used to continuously capture a single fraction near the target mobility μ^* at high resolving power.

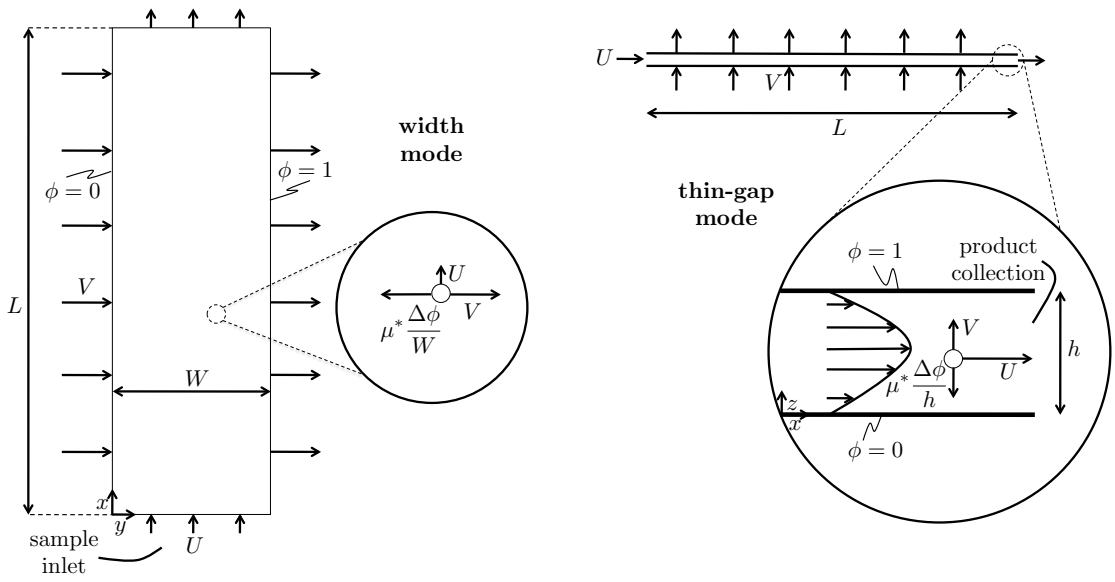

Figure 6.5. Continuous opposed drift electrophoresis. A uniform electric field is counteracted by a crossflow so that the target separand proceeds from the inlet to outlet without deflection. Waste is continuously removed out the sides. As opposed to other continuous methods, the entire cross-sectional area is used for sample introduction and product capture, so the separation may be performed in the dilute limit. In the 'width mode', the electric field $E = \Delta\phi/\ell$ is directed across the width, so $\ell = W$. With the 'thin-gap mode', $\ell = h$.

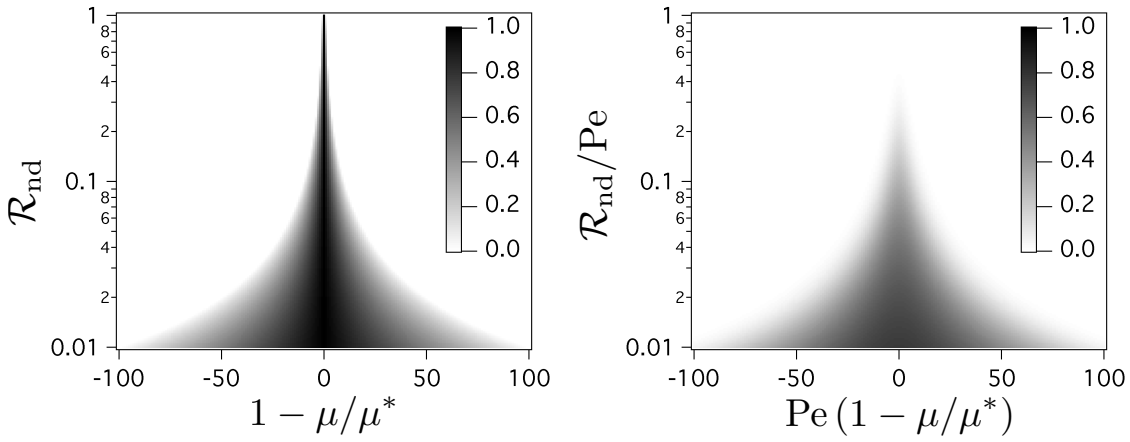

Figure 6.6. Theoretical yield in the kinematic limit and with diffusion. The target species has the highest yield (dark), reaching unity in the kinematic limit, and higher and lower mobility species are rejected out the sides. In the absence of diffusive losses, the yield was found using the method of characteristics to solve $C_x + \mathcal{R}_{\mathrm{nd}}\,(1-\mu/\mu^*)\,C_\xi = 0$ with boundary condition $C\,(0,\ \xi) = 1$, where the subscripts denote differentiation. It varies linearly with the product of the nondispersive resolving power with the reduced mobility, vanishing when the magnitude of $\mathcal{R}_{\mathrm{nd}}\,(1-\mu/\mu^*)$ exceeds unity. The Péclet number, the relative importance of advection to diffusion, plays an important role in determining the resolution when diffusion is included. Although dispersion allows a wider range of mobilities to be transmitted and reduces the yield of the target separand, at high Pe and $\mathcal{R}_{\mathrm{nd}}$ a tight fraction may be captured.

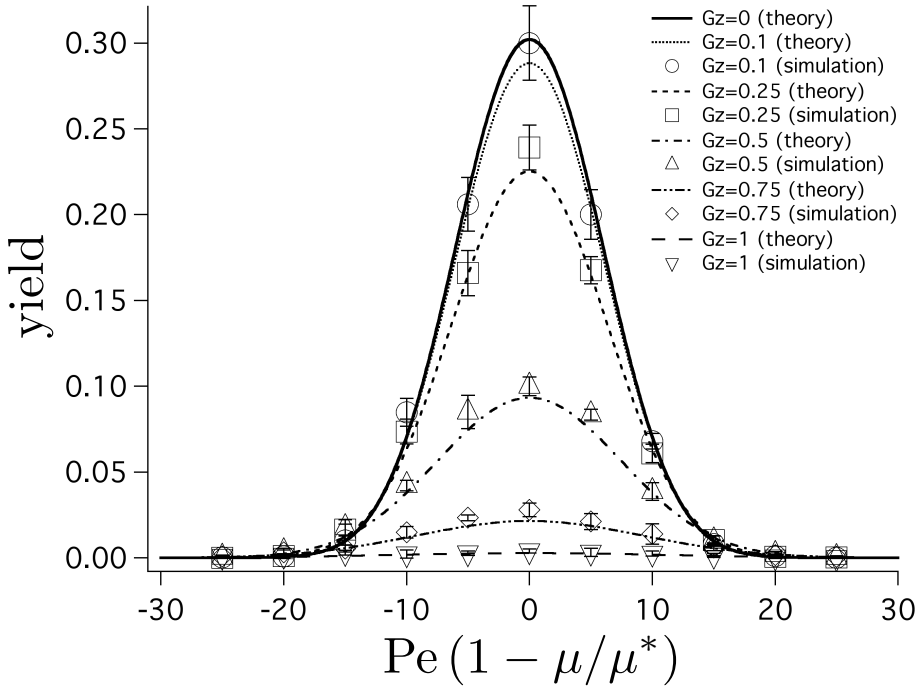

Figure 6.7. Degradation of yield as the Graetz number increases in width mode. Separation of variables and Brownian dynamics simulation results show that for $\mathcal{R}_{\mathrm{nd}}/\mathrm{Pe} = 10^{-1}$ and $\mathrm{Gz}/\mathrm{Pe} = (h/W)^2 = 10^{-3}$, Taylor dispersion across the width reduces the yield substantially as Gz increases.

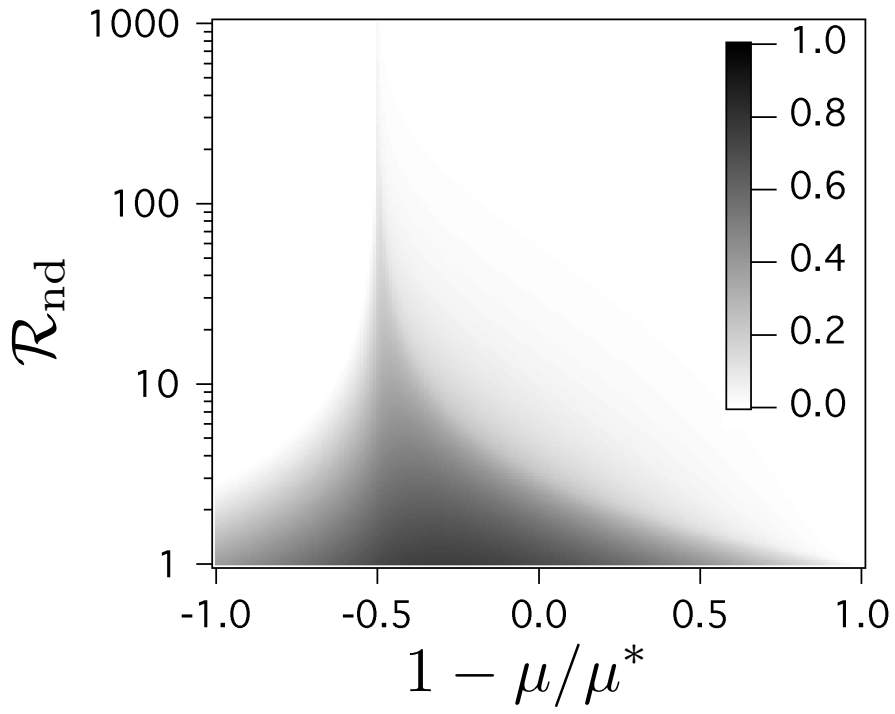

Figure 6.8. Yield in width mode in the absence of cross-streamline diffusion, $\mathrm{Gz} \rightarrow \infty$, found using the method of characteristics to solve $6z\,(1-z)\,C_x + \mathcal{R}_{\mathrm{nd}}\,(6z\,(1-z) - \mu/\mu^*)\,C_y = 0$ with boundary condition $C\,(0,\ y,\ z) = 1$, where the subscripts denote differentiation. Advective dispersion from the parabolic velocity profile results in the maximum transmission probability shifting from $\mu/\mu^* = 1$ as seen in Fig. 6.6, to near $\mu/\mu^* = 3/2$ here.

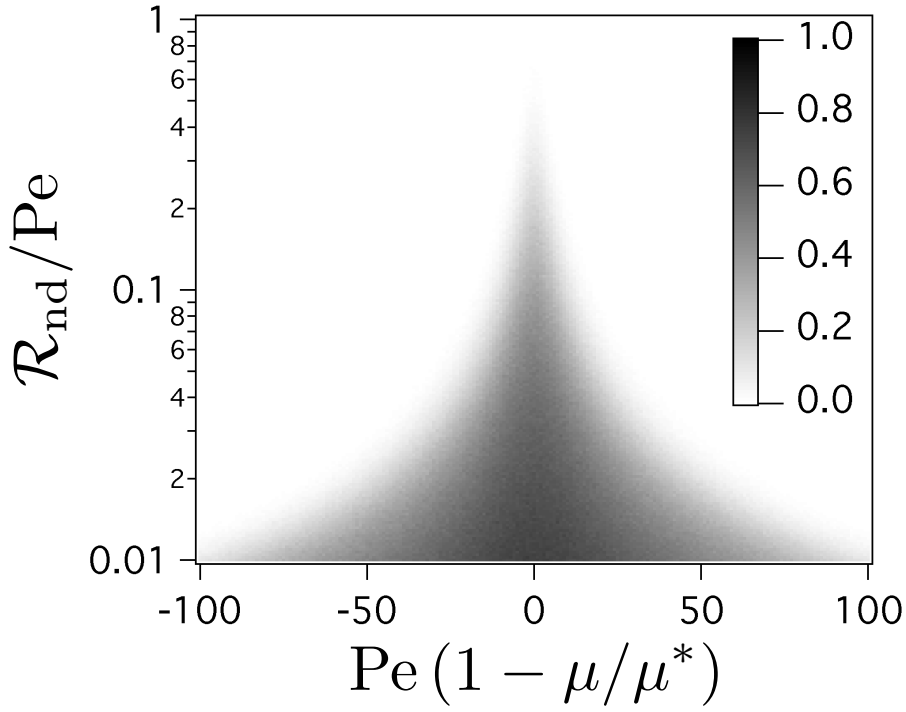

Figure 6.9. Yield for thin-gap mode found via Brownian dynamics simulation. The qualitative similarity to the diffusive result shown in Fig. 6.6 illustrates that advective dispersion from the parabolic shape of the primary flow has a small effect on the performance. Note that as with Fig. 6.6 this is only a small region of the transmission probability map; high resolving power separations can be performed for large Pe and $\mathcal{R}_{\mathrm{nd}}$ with considerably smaller $\mathcal{R}_{\mathrm{nd}}/\mathrm{Pe}$.

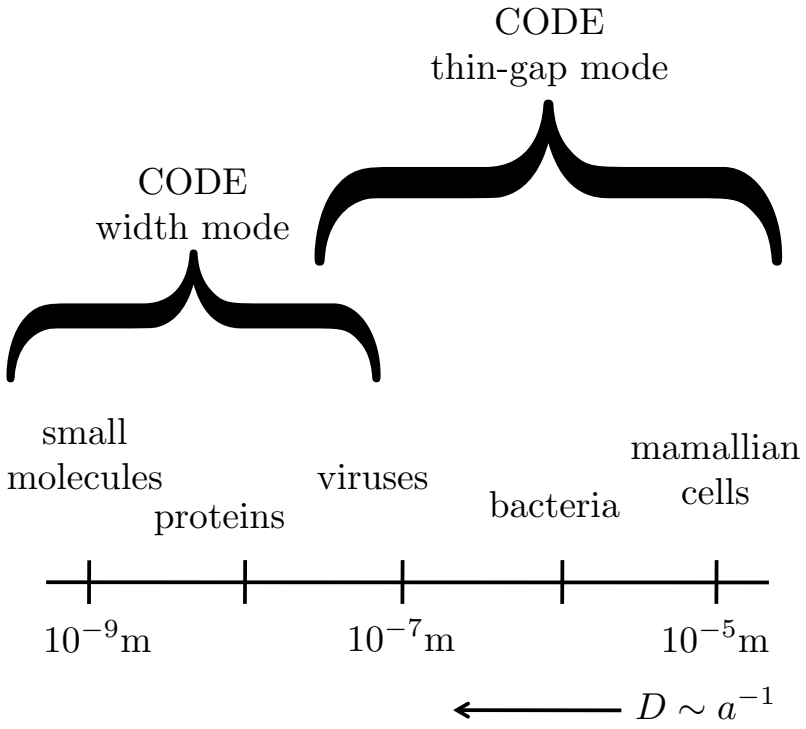

Figure 6.10. Optimal separand size-range for CODE width and thin-gap modes. As diffusion coefficient D is inversely proportional to the characteristic length scale of the separand a, smaller separands rapidly sample the streamlines and are best isolated using the width mode. The thin-gap mode is preferable for larger particles that, because of their small values of D, do not require large $\Delta\phi$ to obtain high values of Pe.

Appendix A

Brownian Dynamics Simulation of Electrophoretic Separation Instruments

We begin with the Langevin equation in the limit where the Stokes number and the Reynolds number are both small,

$$0 = \boldsymbol{F}^H + \boldsymbol{F}^E + \boldsymbol{F}^B, \tag{A.1}$$

where $\boldsymbol{F}^H$ is the hydrodynamic force, $\boldsymbol{F}^E$ is the electrophoretic force, and $\boldsymbol{F}^B$ is the random Brownian force. In the dilute limit, we can treat the particles as an ideal gas and neglect thermodynamic and hydrodynamic interparticle interactions. Furthermore, we assume that hydrodynamic interactions with the walls of the channel may be ignored. We can then write the hydrodynamic force as

$$\boldsymbol{F}^H = -6\pi\eta a \left(\boldsymbol{U} - \boldsymbol{U}^{adv}\right), \tag{A.2}$$

where η is the viscosity of the fluid, a is the particle radius, $\boldsymbol{U}$ is the instantaneous particle velocity, and $\boldsymbol{U}_{adv}$ is the rate at which the particle is advected by the imposed flow. The electrophoretic force is

$$\boldsymbol{F}^E = 6\pi\eta a\mu\boldsymbol{E}, \tag{A.3}$$

where μ is the electrophoretic mobility of the particle and $\boldsymbol{E}$ is the applied electric field. From the Fluctuation-Dissipation theorem, we know the random Brownian

force has the properties

$$\langle \boldsymbol{F}^B \rangle = \mathbf{0}, \tag{A.4}$$

and

$$\langle \boldsymbol{F}^B(t)\boldsymbol{F}^B(t+\tau)\rangle = 2kT6\pi\eta a\boldsymbol{I}\delta(\tau), \tag{A.5}$$

where <> denotes averaging, kT is the thermal energy, τ is a constant, t is time, $\boldsymbol{I}$ is the identity tensor, and δ is the Dirac delta function. For the purpose of a simulation that is discrete in time, we write

$$\boldsymbol{F}^B = \sqrt{2kT6\pi\eta a}\boldsymbol{\Psi}\Phi(t,\Delta t), \tag{A.6}$$

where $\boldsymbol{\Psi}$ is a vector of random numbers with a zero mean and a second moment of unity, Δt is the size of the time step used in the simulation, and Φ approximates the Dirac delta function. The elements of the random vector $\boldsymbol{\Psi}$ may be selected from a continuous distribution of random numbers Ψ. The choice of the distribution is arbitrary, subject to the restrictions from (A.4) and (A.5) which require that

$$\int_{-\infty}^{\infty} P(\Psi)\Psi \, d\Psi = 0 \text{ and} \tag{A.7}$$

$$\int_{-\infty}^{\infty} P(\Psi)\Psi^2 \, d\Psi = 1, \tag{A.8}$$

where $P(\Psi)$ is the probability that Ψ is randomly chosen from the distribution. We use the canned MATLAB function 'randn', which generates a normal distribution with mean zero and variance unity, which satisfies the above requirements, to populate the vector $\boldsymbol{\Psi}$.

The proper form of $\Phi(t,\Delta t)$ can be deduced from consideration of the behavior of the Dirac delta function that it is to approximate. Integration of (A.5) yields

$$\int_{-\infty}^{\infty} \left\langle \mathbf{F}^B(t)\mathbf{F}^B(t+\tau)\right\rangle \, d\tau = 2kT \, 6\pi\eta a\boldsymbol{I}. \tag{A.9}$$

Note that the bounds of integration could have been arbitrarily small, as the Brownian

force is has no memory of previous Brownian forces nor effect on future Brownian forces. The only time correlation between the Brownian force is at the very instant it occurs. In a simulation with discrete time intervals, the time scale over which the Brownian force occurs is no longer infinitesimally small; it has a finite duration of Δt. Hence, a given Brownian force is correlated with itself *only* over the time period from t to $t + \Delta t$. Therefore, the function $\Phi(t, \Delta t)$ must satisfy the relationship

$$\int_{t}^{t+\Delta t} \Phi(t, \Delta t)\Phi(t + \tau, \Delta t)\, d\tau = 1. \tag{A.10}$$

In order to satisfy this relationship, $\Phi(t, \Delta t)$ cannot be an explicit function of t with these limits of integration that were chosen based upon physical arguments. For arbitrary bounds of integration, however, Heaviside step functions that would be explicit functions of time must be used in order to obtain the proper value of the integral and the correct Brownian statistics. For the sake of simplicity and since they are not of any practical value in a simulation, the relevant step functions are omitted so $\Phi(\Delta t)$ is found to be:

$$\Phi(\Delta t) = \frac{1}{\sqrt{\Delta t}} \tag{A.11}$$

We now consider the example of continuous opposed drift electrophoresis operated in its width mode (see 5. Plugging in our relationships for the respective forces into the Langevin equation, we find

$$\boldsymbol{U} = \boldsymbol{U}^{adv} + \mu \boldsymbol{E} + \sqrt{\frac{2D}{\Delta t}}\boldsymbol{\Psi}, \tag{A.12}$$

where we have made use of the Stokes-Einstein-Sutherland relationship $D = kT/6\pi\eta a$, and we note that the diffusion coefficient is taken to be constant for present purposes, where we consider large resolving power separations. We now discretize our velocity as

$$\boldsymbol{U} = \frac{\Delta \boldsymbol{x}}{\Delta t} \tag{A.13}$$

and scale $\boldsymbol{x} \sim W$, $U_x^{adv} \sim \langle U \rangle$, $U_y^{adv} \sim \langle V \rangle$, $\mu E_y \sim \langle V \rangle$, and $\Delta t \sim W/\langle V \rangle$, where W is the width of the channel (measured in the x-direction), $\langle U \rangle$ is the average fluid

velocity in the x-direction, and $\langle V \rangle$ is the average fluid velocity in the y-direction. Note that we scale μE_y with the average velocity in the y-direction – this is motivated by the expectation that the only species of interest will be those with electrophoretic mobilities that are *very* close to the target analyte. Also note that we stipulate that we are in an advection-dominated regime with our scaling for time. Significantly, we stipulate that the characteristic time for diffusion in the z-direction is much faster than that for advection in the x and y directions, so we assume that Taylor dispersion is negligible and construct a 2-D simulation where we make use of average flow-rates rather than the true Poiseuille profiles. Furthermore, we ignore any boundary effects that could give rise to nonuniform velocity profiles in the x and y directions.

We now numerically integrate the Langevin equation with accuracy of $O(\Delta t)$ by multiplying both sides by Δt to obtain the position evolution equations

$$\Delta x = \langle U \rangle \Delta t / \langle V \rangle + \sqrt{2 \Delta t / \mathrm{Pe}} \Psi_x \tag{A.14}$$

and

$$\Delta y = \mu^* \Delta t + \sqrt{2 \Delta t / \mathrm{Pe}} \Psi_y, \tag{A.15}$$

where we have defined the Péclet number $\mathrm{Pe} = W \langle V \rangle / D$ and $\mu* = 1 - \mu / \mu_{target}$.

Bibliography

[1] E. O. Knutson and K. T. Whitby, "Aerosol classification by electric mobility: apparatus, theory, and applications," *J Aerosol Sci*, vol. 6, no. 6, pp. 443 – 451, 1975. 5

[2] S. C. Wang and R. C. Flagan, "Scanning electrical mobility spectrometer," *Aerosol Science and Technology*, vol. 13, no. 2, pp. 230–240, Jan 1990. 5, 37

[3] D. R. Collins, R. C. Flagan, and J. H. Seinfeld, "Improved inversion of scanning dma data," *Aerosol Science and Technology*, vol. 36, no. 1, pp. 1–9, Jan 2002. 5, 37

[4] S. D. Shah and D. R. Cocker, "A fast scanning mobility particle spectrometer for monitoring transient particle size distributions," *Aerosol Science and Technology*, vol. 39, no. 6, pp. 519–526, Jan 2005. 5, 37

[5] P. H. McMurry, "A review of atmospheric aerosol measurements," *Atmos Environ*, vol. 34, no. 12-14, pp. 1959–1999, Jan 2000. 5

[6] W. Winklmayr, G. P. Reischl, A. O. Lindner, and A. Berner, "A new electromobility spectrometer for the measurement of aerosol size distributions in the size range from 1 to 1000nm," *J Aerosol Sci*, vol. 22, no. 3, pp. 289–296, Jan 1991. 7

[7] S. H. Zhang, Y. Akutsu, L. M. Russell, R. C. Flagan, and J. H. Seinfeld, "Radial differential mobility analyzer," *Aerosol Science and Technology*, vol. 23, no. 3, pp. 357–372, Jan 1995. 7, 37, 52

[8] D. R. Chen, D. Y. H. Pui, D. Hummes, H. Fissan, F. R. Quant, and G. J. Sem, "Design and evaluation of a nanometer aerosol differential mobility analyzer (nano-dma)," *J Aerosol Sci*, vol. 29, no. 5-6, pp. 497–509, Jan 1998. 7, 37, 52

[9] J. Rosell-Llompart, I. G. Loscertales, D. Bingham, and J. F. de la Mora, "Sizing nanoparticles and ions with a short differential mobility analyzer," *J Aerosol Sci*, vol. 27, no. 5, pp. 695–719, Jan 1996. 7

[10] L. de Juan and J. F. de la Mora, "High resolution size analysis of nanoparticles and ions: Running a vienna dma of near optimal length at reynolds numbers up to 5000," *J Aerosol Sci*, vol. 29, no. 5-6, pp. 617–626, Jan 1998. 7, 37, 52

[11] S. Rosser and J. F. de la Mora, "Vienna-type dma of high resolution and high flow rate," *Aerosol Science and Technology*, vol. 39, no. 12, pp. 1191–1200, Jan 2005. 7, 37, 52

[12] P. Martinez-Lozano and J. F. de la Mora, "Resolution improvements of a nano-dma operating transonically," *J Aerosol Sci*, vol. 37, no. 4, pp. 500–512, Jan 2006. 7, 37, 52

[13] N. A. Brunelli, R. C. Flagan, and K. P. Giapis, "Radial differential mobility analyzer for one nanometer particle classification," *Aerosol Science and Technology*, vol. 43, no. 1, pp. 53–59, Jan 2009. 7, 37, 52

[14] M. Alonso, "Reducing the diffusional spreading rate of a brownian particle by an appropriate non-uniform external force field," *J Aerosol Sci*, vol. 33, no. 3, pp. 439–450, Jan 2002. 7

[15] I. G. Loscertales, "Drift differential mobility analyzer," *J Aerosol Sci*, vol. 29, no. 9, pp. 1117–1139, Jan 1998. 7, 38

[16] H. Tammet, "The limits of air ion mobility resolution," in *Proceedings of the 11th International Conference on Atmospheric Electricity*, Guntersville, Apr 1999, pp. 7–11. 7

[17] ——, "Method of inclined velocities in the air ion mobility analysis," in *Proceedings of the 12th International Conference on Atmospheric Electricity, Vol. 1*, Versailles, 2003, pp. 399–402. 7, 38

[18] ——, "Symmetric inclined grid mobility analyzer for the measurement of charged clusters and fine nanoparticles in atmospheric air," *Aerosol Science and Technology*, vol. 45, no. 4, pp. 468–479, Apr 2011. 8, 38, 52

[19] R. C. Flagan, "Opposed migration aerosol classifier (omac)," *Aerosol Science and Technology*, vol. 38, no. 9, pp. 890–899, Jan 2004. 8, 15, 38, 99

[20] Y. Kousaka, K. Okuyama, M. Adachi, and T. Mimura, "Effect of brownian diffusion on electrical classification of ultrafine aerosol-particles in differential mobility analyzer," *J Chem Eng Jpn*, vol. 19, no. 5, pp. 401–407, Jan 1986. 9

[21] M. R. Stolzenburg, "*An ultrafine aerosol size distribution measuring system*," Ph.D. dissertation, University of Minnesota, 1988. xix, 9, 41, 43, 65, 67, 77

[22] S. H. Zhang and R. C. Flagan, "Resolution of the radial differential mobility analyzer for ultrafine particles," *J Aerosol Sci*, vol. 27, no. 8, pp. 1179–1200, Jan 1996. 9, 43

[23] R. C. Flagan, "On differential mobility analyzer resolution," *Aerosol Science and Technology*, vol. 30, no. 6, pp. 556–570, Jan 1999. 9, 11, 18

[24] C. Hagwood, Y. Sivathanu, and G. Mulholland, "The dma transfer function with brownian motion a trajectory/monte-carlo approach," *Aerosol Science and Technology*, vol. 30, no. 1, pp. 40–61, Jan 1999. 9

[25] R. Haberman, *Applied partial differential equations*, 4th ed. New Jersey: Pearson Prentice Hall, 2004. 12

[26] D. L. Ermak and J. A. McCammon, "Brownian dynamics with hydrodynamic interactions," *J Chem Phys*, vol. 69, no. 4, pp. 1352–1360, 1978. 15, 102

[27] M. Fixman, "Simulation of polymer dynamics .1. general theory," *J Chem Phys*, vol. 69, no. 4, pp. 1527–1537, Jan 1978. 15, 102

[28] D. R. Collins, A. Nenes, R. C. Flagan, and J. H. Seinfeld, "The scanning flow dma," *J Aerosol Sci*, vol. 31, no. 10, pp. 1129–1144, Jan 2000. xvi, 32

[29] A. J. Downard, J. F. Dama, and R. C. Flagan, "An asymptotic analysis of differential electrical mobility classifiers," *Aerosol Science and Technology*, vol. 45, no. 6, pp. 717–729, Jun 2011. 38, 41, 42

[30] M. R. Stolzenburg and P. H. McMurry, "Equations governing single and tandem dma configurations and a new lognormal approximation to the transfer function," *Aerosol Science and Technology*, vol. 42, no. 6, pp. 421–432, 2008. 41, 43

[31] D. J. Rader and P. H. McMurry, "Application of the tandem differential mobility analyzer to studies of droplet growth or evaporation," *J Aerosol Sci*, vol. 17, no. 5, pp. 771–787, 1986. 43

[32] M. R. Stolzenburg and P. H. McMurry, "An ultrafine aerosol condensation nucleus counter," *Aerosol Science and Technology*, vol. 14, no. 1, pp. 48–65, 1991. xix, 52, 65, 67, 77

[33] J. Zhao, F. L. Eisele, M. Titcombe, C. Kuang, and P. H. McMurry, "Chemical ionization mass spectrometric measurements of atmospheric neutral clusters using the cluster-cims," *J Geophys Res-Atmos*, vol. 115, p. D08205, 2010. 52

[34] A. Mirme, E. Tamm, G. Mordas, M. Vana, J. Uin, S. Mirme, T. Bernotas, L. Laakso, A. Hirsikko, and M. Kulmala, "A wide-range multi-channel air ion spectrometer," *Boreal Environ Res*, vol. 12, no. 3, pp. 247–264, 2007. 52

[35] J. Jiang, M. Attoui, M. Heim, N. Brunelli, P. H. McMurry, G. Kasper, R. C. Flagan, K. Giapis, and G. Mouret, "Transfer functions and penetrations of five differential mobility analyzers for sub-2 nm particle classification," *Aerosol Science and Technology*, vol. 45, no. 4, pp. 480–492, 2011. 53

[36] K. Iida, M. R. Stolzenburg, and P. H. McMurry, "Effect of working fluid on sub-2 nm particle detection with a laminar flow ultrafine condensation particle counter," *Aerosol Science and Technology*, vol. 43, no. 1, pp. 81–96, 2009. xix, 53, 58, 73, 77

[37] K. Okuyama, Y. Kousaka, and T. Motouchi, "Condensational growth of ultrafine aerosol particles in a new particle size magnifier," *Aerosol Science and Technology*, vol. 3, no. 4, pp. 353–366, 1984. xix, 54, 65, 77

[38] L. Sgro and J. de la Mora, "A simple turbulent mixing cnc for charged particle detection down to 1.2 nm," *Aerosol Science and Technology*, vol. 38, no. 1, pp. 1–11, 2004. 54, 65

[39] J. Vanhanen, J. Mikkila, K. Lehtipalo, M. Sipila, H. E. Manninen, E. Siivola, T. Petaja, and M. Kulmala, "Particle size magnifier for nano-CN detection," *Aerosol Science and Technology*, vol. 45, no. 4, pp. 533–542, 2011. 54, 65

[40] J. Kirkby, J. Curtius, J. Almeida, E. Dunne, J. Duplissy, S. Ehrhart, A. Franchin, S. Gagné, L. Ickes, A. Kürten, A. Kupc, A. Metzger, F. Riccobono, L. Rondo, S. Schobesberger, G. Tsagkogeorgas, D. Wimmer, A. Amorim, F. Bianchi, M. Breitenlechner, A. David, J. Dommen, A. Downard, M. Ehn, R. C. Flagan, S. Haider, A. Hansel, D. Hauser, W. Jud, H. Junninen, F. Kreissl, A. Kvashin, A. Laaksonen, K. Lehtipalo, J. Lima, E. R. Lovejoy, V. Makhmutov, S. Mathot, J. Mikkilä, P. Minginette, S. Mogo, T. Nieminen, A. Onnela, P. Pereira, T. Petäjä, R. Schnitzhofer, J. H. Seinfeld, M. Sipilä, Y. Stozhkov, F. Stratmann, A. Tomé, J. Vanhanen, Y. Viisanen, A. Vrtala, P. E. Wagner, H. Walther, E. Weingartner, H. Wex, P. M. Winkler, K. S. Carslaw, D. R. Worsnop, U. Baltensperger, and M. Kulmala, "Role of sulphuric acid, ammonia and galactic cosmic rays in atmospheric aerosol nucleation," *Nature*, vol. 476, no. 7361, pp. 429–433, 2011. 54

[41] R. C. Flagan, S. C. Wang, F. D. Yin, J. H. Seinfeld, G. Reischl, W. Winklmayr, and R. Karch, "Electrical mobility measurements of fine-particle forma-

tion during chamber studies of atmospheric photochemical-reactions," *Environ Sci Technol*, vol. 25, no. 5, pp. 883–890, 1991. 57

[42] C. Kuang, M. Chen, P. H. McMurry, and J. Wang, "Modification of laminar flow ultrafine condensation particle counters for the enhanced detection of 1 nm condensation nuclei," *Aerosol Science and Technology*, vol. 46, no. 3, pp. 309–315, 2012. 58, 66, 73

[43] P. Martinez-Lozano, M. Labowsky, and J. F. de la Mora, "Experimental tests of a nano-dma with no voltage change between aerosol inlet and outlet slits," *J Aerosol Sci*, vol. 37, no. 11, pp. 1629–1642, 2006. 58

[44] J. K. Agarwal and G. J. Sem, "Continuous-flow, single-particle-counting condensation nucleus counter," *J Aerosol Sci*, vol. 11, no. 4, pp. 343–357, 1980. xix, 64, 77

[45] P. H. McMurry, "The history of condensation nucleus counters," *Aerosol Science and Technology*, vol. 33, no. 4, pp. 297–322, 2000. xix, 65, 77

[46] C. L. Yaws, *Yaws' Handbook of Thermodynamic and Physical Properties of Chemical Compounds*. Norwich, New York: Knovel, 2003. 67

[47] J. H. Seinfeld and S. N. Pandis, *Atmospheric chemistry and physics: from air pollution to climate change*. New Jersey: Wiley, 2006. 68

[48] S. V. Hering, M. R. Stolzenburg, F. R. Quant, D. R. Oberreit, and P. B. Keady, "A laminar-flow, water-based condensation particle counter (wcpc)," *Aerosol Science and Technology*, vol. 39, no. 7, pp. 659–672, 2005. xix, 77

[49] F. W. Karasek and D. W. Denney, "Detection of 2,4,6-trinitrotoluene vapors in air by plasma chromatography," *J Chromatogr*, vol. 93, no. 1, pp. 141–147, 1974. 87

[50] T. M. Sanders and S. R. Forrest, "Small particle-size distributions from mobility measurements," *J Appl Phys*, vol. 66, no. 7, pp. 3317–3323, 1989. 87

[51] H. H. Hill and S. J. Martin, "Conventional analytical methods for chemical warfare agents," *Pure Appl Chem*, vol. 74, no. 12, pp. 2281–2291, 2002. 87

[52] G. A. Eiceman and Z. Karpas, *Ion Mobility Spectrometry*. Boca Raton: Taylor & Francis, 2005. 87

[53] B. C. Bohrer, S. I. Mererbloom, S. L. Koeniger, A. E. Hilderbrand, and D. E. Clemmer, "Biomolecule analysis by ion mobility spectrometry," *Annu Rev Anal Chem*, vol. 1, pp. 293–327, 2008. 87

[54] H. H. Hill, W. F. Siems, R. H. St. Louis, and D. G. McMinn, "Ion mobility spectrometry," *Anal. Chem*, vol. 62, no. 23, pp. A1201–A1209, 1990. 87

[55] D. Gerlich, "Inhomogeneous rf-fields - a versatile tool for the study of processes with slow ions," *Adv Chem Phys*, vol. 82, pp. 1–176, 1992. 87, 91

[56] S. H. Guan and A. G. Marshall, "Stacked-ring electrostatic ion guide," *J Am Soc Mass Spectr*, vol. 7, no. 1, pp. 101–106, 1996. 87, 91

[57] K. Tang, A. A. Shvartsburg, H. N. Lee, D. C. Prior, M. A. Buschbach, F. M. Li, A. V. Tolmachev, G. A. Anderson, and R. D. Smith, "High-sensitivity ion mobility spectrometry/mass spectrometry using electrodynamic ion funnel interfaces," *Anal. Chem*, vol. 77, no. 10, pp. 3330–3339, 2005. 87, 92

[58] R. T. Kelly, A. V. Tolmachev, J. S. Page, K. Tang, and R. D. Smith, "The ion funnel: Theory, implementations, and applications," *Mass Spectrom. Rev.*, vol. 29, no. 2, pp. 294–312, 2010. 87, 92

[59] D. E. Clemmer and M. F. Jarrold, "Ion mobility measurements and their applications to clusters and biomolecules," *J Mass Spectrom*, vol. 32, no. 6, pp. 577–592, 1997. 88

[60] H. E. Revercomb and E. A. Mason, "Theory of plasma chromatography/gaseous electrophoresis–a review," *Anal. Chem*, vol. 47, no. 7, pp. 970–983, 1975. 88

[61] E. V. Krylov, E. G. Nazarov, and R. A. Miller, "Differential mobility spectrometer: Model of operation," *Int J Mass Spectrom*, vol. 266, no. 1-3, pp. 76–85, 2007. 89

[62] K. Giles, S. D. Pringle, K. R. Worthington, D. Little, J. L. Wildgoose, and R. H. Bateman, "Applications of a travelling wave-based radio-frequency-only stacked ring ion guide," *Rapid Commun Mass Sp*, vol. 18, no. 20, pp. 2401–2414, 2004. 89

[63] S. D. Pringle, K. Giles, J. L. Wildgoose, J. P. Williams, S. E. Slade, K. Thalassinos, R. H. Bateman, M. T. Bowers, and J. H. Scrivens, "An investigation of the mobility separation of some peptide and protein ions using a new hybrid quadrupole/travelling wave ims/oa-tof instrument," *Int J Mass Spectrom*, vol. 261, no. 1, pp. 1–12, 2007. 89

[64] L. Lapidus and N. R. Amundson, "Mathematics of adsorption in beds. vi. the effect of longitudinal diffusion in ion exchange and chromatographic columns," *J Phys Chem*, vol. 56, no. 8, pp. 984–988, 1952. 89

[65] J. C. Giddings and K. Dahlgren, "Resolution and peak capacity in equilibrium-gradient methods of separation," *Separ Sci*, vol. 6, no. 3, pp. 345–356, 1971. 89, 90, 98

[66] J. C. Giddings, "Hyperlayer field-flow fractionation," *Separ Sci Technol*, vol. 18, no. 8, pp. 765–773, 1983. 90, 99

[67] P. H. O'Farrell, "Separation techniques based on the opposition of two counteracting forces to produce a dynamic equilibrium," *Science*, vol. 227, no. 4694, pp. 1586–1589, 1985. 90, 98

[68] C. F. Ivory and W. A. Gobie, "Continuous counteracting chromatographic electrophoresis," *Biotechnology Progress*, vol. 6, no. 1, pp. 21–32, 1990. 90, 99

[69] W. S. Koegler and C. F. Ivory, "Field gradient focusing: A novel method for

protein separation," *Biotechnology Progress*, vol. 12, no. 6, pp. 822–836, 1996. 90, 98

[70] P. H. Rhodes and R. S. Snyder, "Method and apparatus for electrophoretic focusing," *US Patent 6,171,466*, 2001. 90, 99

[71] C. F. Ivory, "Several new electrofocusing techniques," *Electrophoresis*, vol. 28, pp. 15–25, 2007. 90, 99

[72] M. Bier, "Rotating apparatus for isoelectric focusing," *US Patent 4,588,492*, 1986. 90

[73] O. N. Katasonova and P. S. Fedotov, "Methods for continuous flow fractionation of microparticles: Outlooks and fields of application," *J Anal Chem*, vol. 64, no. 3, pp. 212–225, 2009. 98

[74] T. M. Przybycien, N. S. Pujar, and L. M. Steele, "Alternative bioseparation operations: Life beyond packed-bed chromatography," *Current Opinion Biotech.*, vol. 15, no. 5, pp. 469–478, 2004. 98

[75] T. Chapman, "Protein purification: pure but not simple," *Nature*, vol. 434, no. 7034, pp. 795–798, 2005. 98

[76] U. Gottschalk, "Bioseparation in antibody manufacturing: the good, the bad and the ugly," *Biotechnology Progress*, vol. 24, no. 3, 2008. 98

[77] A. Strickler, "Continuous particle electrophoresis: A new analytical and preparative capability," *Separ Sci*, vol. 2, no. 3, pp. 335–355, 1967. 98

[78] J. C. Giddings, H. C. Lin, K. D. Caldwell, and M. N. Myers, "Outlet stream splitting for sample concentration in field-flow fractionation," *Separ Sci Technol*, vol. 18, no. 3, pp. 293–306, 1983. 99

[79] J. C. Giddings, "A system based on split-flow lateral transport thin (splitt) separation cells for rapid and continuous particle fractionation," *Separ Sci Technol*, vol. 20, no. 9-10, pp. 749–768, 1985. 99

[80] S. Levin, M. N. Myers, and J. C. Giddings, "Continuous separation of proteins in electrical split-flow thin (splitt) cell with equilibrium operation," *Separ Sci Technol*, vol. 24, no. 14, pp. 1245–1259, 1989. 99

[81] R. S. Snyder and P. H. Rhodes, "Electrophoresis experiments for space," *AIP Conf. Proc.*, no. 504, pp. 568–573, 2000. 99

[82] H. D. Tolley, Q. G. Wang, D. A. Le Febre, and M. L. Lee, "Equilibrium gradient methods with nonlinear field intensity gradient: A theoretical approach," *Anal. Chem*, vol. 74, no. 17, pp. 4456–4463, 2002. 99

[83] D. A. Le Febre, "Analyte species separation system," *US Patent 7,141,152*, 2006. 99

[84] S. Jones and J. M. Thornton, "Principles of protein-protein interactions," *PNAS*, vol. 93, no. 1, pp. 13–20, 1996. 99

[85] W. E. Stites, "Protein–protein interactions: Interface structure, binding thermodynamics, and mutational analysis," *Chem. Rev*, vol. 97, no. 5, pp. 1233–1250, 1997. 99

[86] B. Schwikowski, P. Uetz, and S. Fields, "A network of protein–protein interactions in yeast," *Nature Biotechnology*, vol. 18, no. 12, pp. 1257–1261, 2000. 99

[87] M. Bier, O. A. Palusinski, R. A. Mosher, and D. A. Saville, "Electrophoresis - mathematical modeling and computer simulation," *Science*, vol. 219, no. 4590, pp. 1281–1287, 1983. 99, 100

[88] N. I. Tracy and C. F. Ivory, "Nonlinear modeling of protein separation in a preparative-scale dynamic field gradient focusing instrument," *AIChE J*, vol. 55, no. 1, pp. 63–74, 2009. 99, 100

[89] D. W. Richman, "System for hydrodynamic compensation for electrophoresis crescent distortion," *US Patent 4,309,268*, 1982. 100

[90] C. T. Culbertson and J. W. Jorgenson, "Flow counterbalanced capillary electrophoresis," *Anal. Chem*, vol. 66, no. 7, pp. 955–962, 1994. 100

[91] A. Strickler, "Continuous free-film electrophoresis – crescent phenomenon," *Prep Biochem*, vol. 3, no. 3, pp. 269–277, 1973. 101

[92] P. H. Rhodes and R. S. Snyder, "Moving wall, continuous flow electrophoresis apparatus," *US Patent 4,752,372*, 1988. 101

[93] R. Aris, "On the dispersion of a solute in a fluid flowing through a tube," *Proc R Soc Lon Ser-A*, vol. 235, no. 1200, pp. 67–77, 1956. 102

[94] E. Peters and T. Barenbrug, "Efficient brownian dynamics simulation of particles near walls. i. reflecting and absorbing walls," *Physical Review E*, vol. 66, no. 5, p. 56701, 2002. 102

[95] J. C. Giddings, "Two-dimensional separations – concept and promise," *Anal. Chem*, vol. 56, no. 12, pp. 1258–1270, 1984. xxi, 108